

AD-A035 880

GENERAL RESEARCH CORP MCLEAN VA WASHINGTON OPERATIONS  
SENSOR MODULATION EFFECTS UPON LASER SIGNATURES.(U)

F/G 17/8

DEC 76 J L GILBERT, P J KRAMER, W N PETERS

F30602-75-C-0292

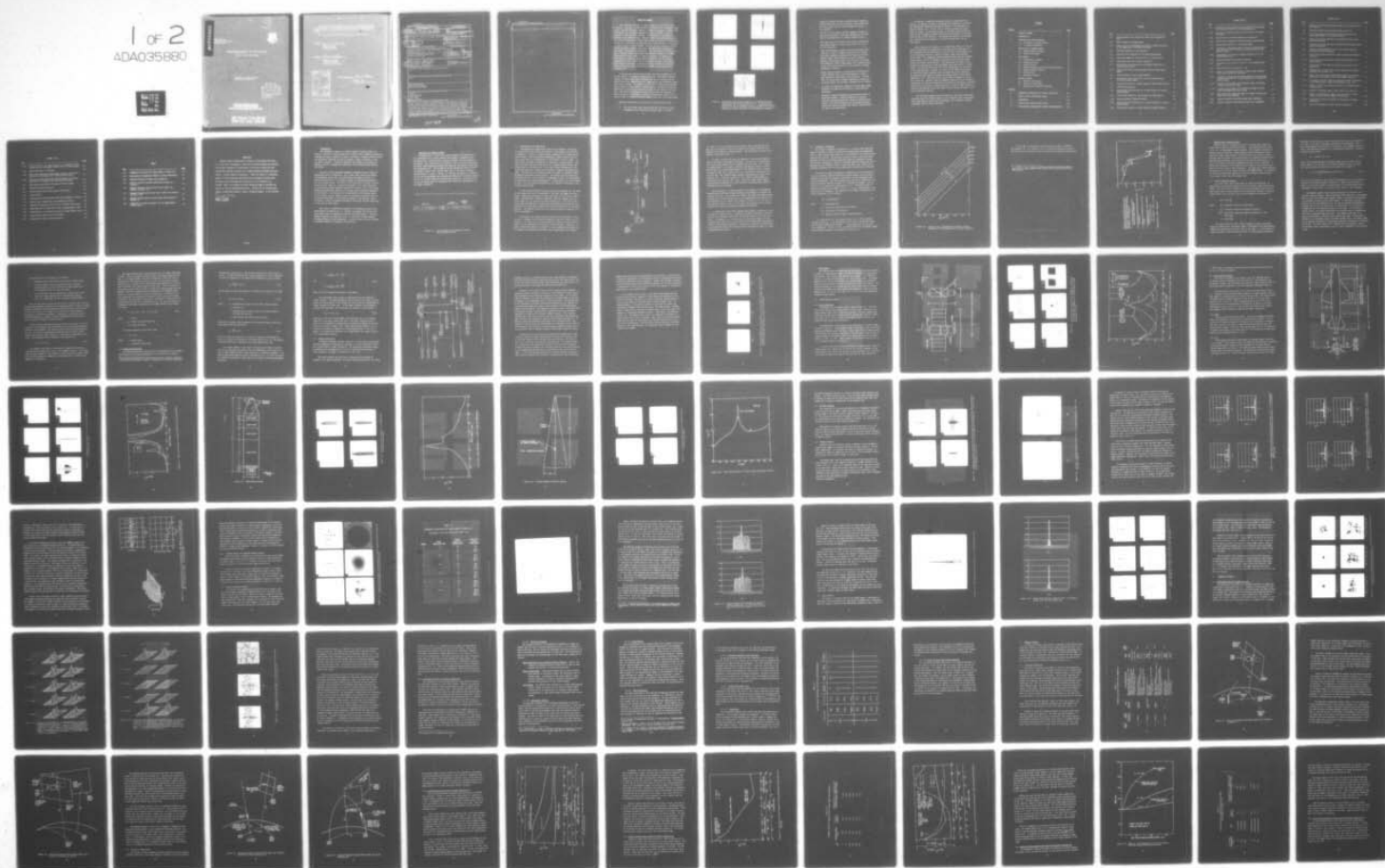
UNCLASSIFIED

905-01-CR

RADC-TR-76-391

NL

1 of 2  
ADA035880



Approved for public release;  
classification unclassified.

D-E  
D  
E  
E

UNCLASSIFIED

SECURITY CLASSIFICATION OF THIS PAGE (When Data Entered)

REPORT DOCUMENTATION PAGE		READ INSTRUCTIONS BEFORE COMPLETING FORM	
1. REPORT NUMBER <b>18</b> RADC-76-391 <b>19</b> 7R-76-391	2. GOVT ACCESSION NO.	3. RECIPIENT'S CATALOG NUMBER <b>9</b>	
4. TITLE (and Subtitle) <b>6</b> <u>SENSOR MODULATION EFFECTS UPON LASER SIGNATURES.</u>	5. TYPE OF REPORT & DATES COVERED Final Technical Report,		
6. AUTHOR(s) <b>10</b> J. L. Gilbert, P. J. Kramer, W. N. Peters	7. PERFORMING ORG. REPORT NUMBER <b>14</b> 905-01-CR	8. CONTRACT OR GRANT NUMBER(s) <b>15</b> F30602-75-C-0292 New	
9. PERFORMING ORGANIZATION NAME AND ADDRESS General Research Corporation/Washington Operations Westgate Research Park, 7655 Old Springhouse Road McLean VA 22101	10. PROGRAM ELEMENT, PROJECT, TASK AREA & WORK UNIT NUMBERS 62702F 65270131 <b>12</b>	11. CONTROLLING OFFICE NAME AND ADDRESS Rome Air Development Center (OCTM) Griffiss AFB NY 13441 <b>11</b>	12. REPORT DATE December 1976 <b>177 p.</b>
13. MONITORING AGENCY NAME & ADDRESS (if different from Controlling Office) Same <b>16</b> 6527 <b>17</b> 01	14. NUMBER OF PAGES 161	15. SECURITY CLASS. (of this report) UNCLASSIFIED	15a. DECLASSIFICATION/DOWNGRADING SCHEDULE N/A
16. DISTRIBUTION STATEMENT (of this Report) Approved for public release; distribution unlimited.			
17. DISTRIBUTION STATEMENT (of the abstract entered in Block 20, if different from Report) Same			
18. SUPPLEMENTARY NOTES RADC Project Engineer: Donald F. McKee (OCTM)			
19. KEY WORDS (Continue on reverse side if necessary and identify by block number) Sensors Target Signature Laser Radiation Laser Radar Optics, Coherent			
20. ABSTRACT (Continue on reverse side if necessary and identify by block number) This study is an analysis of coherent sensor system observable effects which tend to obscure target properties of interest. The main effects studied are finite system resolution, speckle, shot noise, and atmospheric propagation. In addition to these effects, several scenarios were considered to provide realistic assessments of their effects on the performance of laser radar systems. Also included is an investigation of the feasibility of performing range-Doppler imaging using different lasers in the measurement of range and Doppler. The analysis was made to determine the existence and extent of any fundamental			

DD FORM 1 JAN 73 1473 EDITION OF 1 NOV 65 IS OBSOLETE

UNCLASSIFIED

SECURITY CLASSIFICATION OF THIS PAGE (When Data Entered)

390 967

y/B

UNCLASSIFIED

SECURITY CLASSIFICATION OF THIS PAGE(When Data Entered)

problem areas which would prohibit or seriously limit the use of this technique.

UNCLASSIFIED

SECURITY CLASSIFICATION OF THIS PAGE(When Data Entered)

## EXECUTIVE SUMMARY

The fundamental concept of a target signature usually stems from a desire to associate a target property of interest with a measurable parameter. Although the target property or feature represents a constant physical entity, the observable parameter by which an attempt is made to evaluate it need not remain constant. By definition an observable is a function of the sensing system. However, rather than dealing with specific sensor configurations, effects which reduce the quality or information content of an observable are identified and illustrated only as they apply to general types of sensor systems. The main effects studied are finite system resolution, speckle, shot noise, and atmospheric propagation as they apply to coherent laser radiation. For the purpose of illustration, Fig. 1 includes several distributed cross-section "images" of a METEOR satellite which show examples of these key effects. In addition to these effects, several scenarios were considered to provide realistic assessments of their effects on the performance of laser radar systems. These scenarios included: ground-to-satellite; satellite-to-satellite; satellite-to-cruise missile; satellite-to-SLEM; and satellite-to-exo-atmospheric RV.

To perform the study and also provide illustrative examples of the various effects, two computer programs were used. The TARGSIM computer program, developed under other contracts, was used to calculate the expected value total, Doppler-resolved, range-Doppler, and distributed laser radar cross sections. In addition, it was used to include system effects such as finite receiver aperture, diffuse speckle, and detection noise by modifying the expected value signature knowing the statistics of the process. The Sensor System Model was used to synthesize the operation of actual systems and to calculate a series of instantaneous samples of the electric field or detected electrical signal rather than the average value.

Important conclusions of the study are outlined briefly below.

- The total laser radar cross section may vary several orders of magnitude with variations in aspect angle. In actual

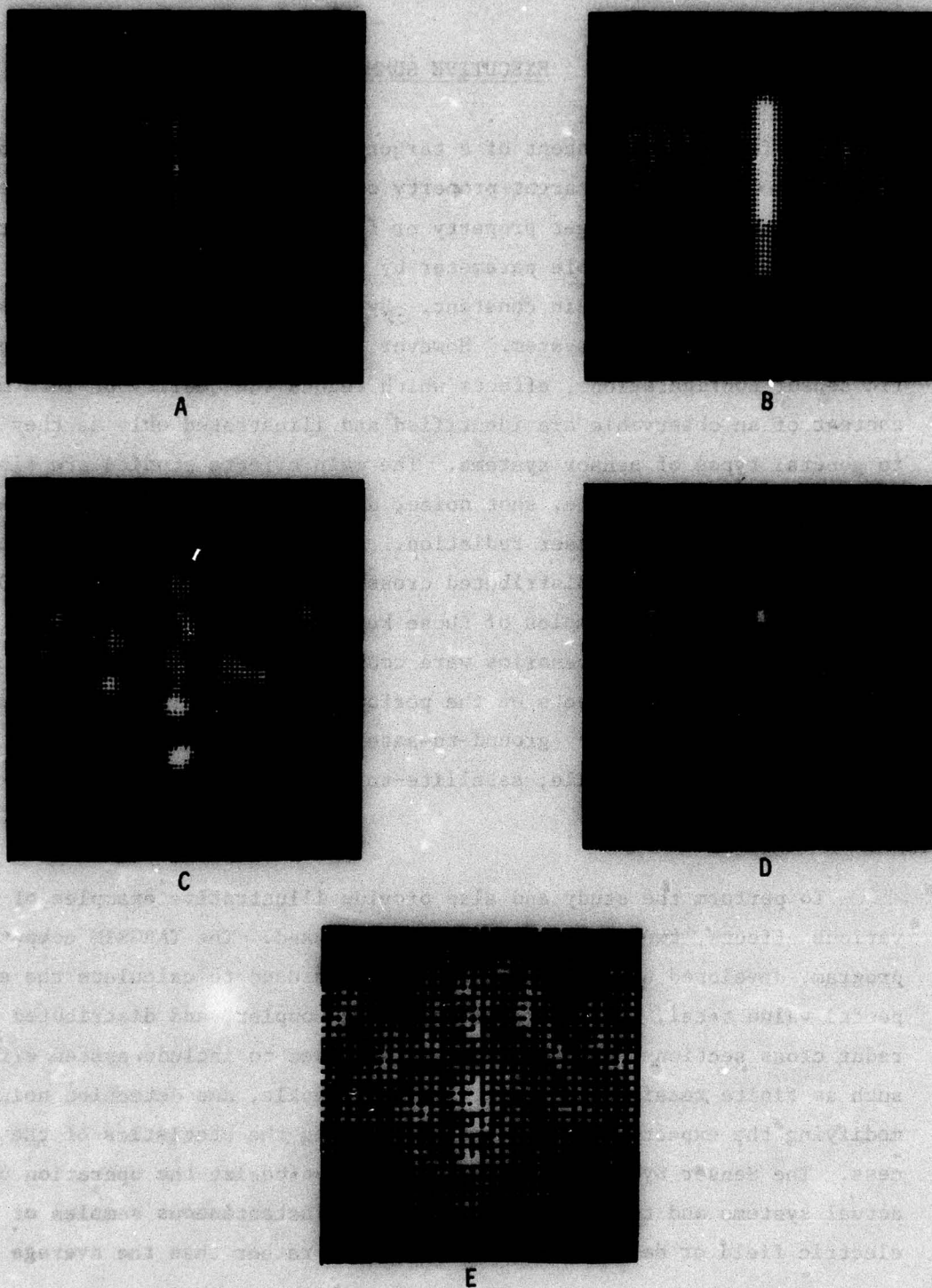


**Figure 1. Distributed Cross Section "Images" of the METEOR Satellite Illustrating Several Observable Effects: (A) Ideal System Performance; (B) 0.5 m Resolution; (C) 0.5 m Resolution with Speckle; (D) 0.5 m Resolution, Speckle, and SNR = 10; (E) 0.5 m Resolution, Speckle, and Effects of Atmospheric Propagation**

scenarios, however, the set of possible aspect angles is usually restricted such that the total cross section does not vary by more than one order of magnitude during an encounter.

- For most of the scenarios studied, changes in target aspect are slow enough to allow data averaging for the purposes of reducing noise and coherent speckle effects.
- The ranges involved ( $>250$  km) preclude using conventional angle-angle imagery to obtain target detail with realistic size apertures.
- Ideal one-dimensional synthetic resolution systems (i.e., resolving in range or Doppler frequency shift) provide sufficient resolution independent of object-to-receiver range to allow identification or feature extraction. However, such systems exhibit lower contrast ratios than two-dimensional systems (angle-angle) with comparable resolution, thus their potential for such purposes as damage assessment is reduced.
- Speckle effects caused by a moving target illuminated by a high coherence source can be averaged out to yield a good estimate of the expected value signature. If, however, the target aspect changes significantly during the averaging process, the resultant signature will be invalid.
- The effect of atmospheric turbulence on angle-angle images illustrate the need for pre-detection or post-detection processing.
- Synthetic resolution systems are generally more immune to atmospheric effects. Notable exceptions are effects caused by possible fluctuations induced by amplitude variations of the illuminating field at the target, and large effects may appear in systems with Doppler resolutions better than a few hundred hertz.

In addition to assessing observable effects on laser radar performance, an analysis was made to investigate the feasibility of performing range-Doppler imaging using different lasers in the measurement of range and Doppler (e.g., CW gas laser for Doppler, pulsed solid-state laser for range). The analysis was made to determine the existence and extent of any fundamental problem areas which would prohibit or seriously limit the use of this technique. The theoretical aspects of the problem were considered and then applied to a pulsed YAG laser and a CW CO<sub>2</sub> laser system.

After examining the analysis of the theoretical aspects of the problem and considering the capabilities of available laser technology, it was determined that the performance of the two laser (bi-wavelength) system was basically inferior to that of a single, large time-bandwidth laser system. The fundamental problem encountered with the bi-wavelength system concept is that the ambiguity functions of the individual laser sources add (rather than multiply). This means that the flaws of both sources are retained with little enhancement where they overlap. Specifically, a typical YAG laser meets all of the requirements for resolution in the range dimension. However, the effect of the phase uncertainties in typical YAG lasers indicates that the capability of the coherently processed YAG laser system to measure the target profile in the Doppler dimension is lost. The insertion of the CW laser is intended to retain this resolution. However, since the ambiguity functions of the individual sources add, any benefit obtained from an increase in the Doppler resolution provided by the CW laser is counterbalanced by a loss in range resolution caused by the addition of the side lobes of the CW laser's response to the overall ambiguity function.

The conclusion reached from this analysis is that the bi-wavelength technique using two different lasers is not competitive with other single-laser range-Doppler systems under development; and, therefore, hardware development does not appear warranted.

## CONTENTS

<u>SECTION</u>		<u>PAGE</u>
	EXECUTIVE SUMMARY	1
1	INTRODUCTION	1
2	INTERFACES AND EFFECTS STUDIED	2
	2.1 Description of System Effects	3
	2.2 Atmospheric Turbulence	6
3	DESCRIPTION OF COMPUTER MODELS	10
	3.1 TARGSIM Computer Program	10
	3.2 Sensor System Model	15
4	CASE STUDIES	20
	4.1 Description of Targets	20
	4.2 Aperture Blurring	34
	4.3 Speckle Effects	34
	4.4 Combined Speckle and Aperture-Blurring Effects	42
	4.5 Damage Assessment Effects	42
	4.6 Noise Effects	48
	4.7 Atmospheric Effects	52
5	SCENARIO STUDIES	64
	5.1 Simulator Description	64
	5.2 Results of Simulations	69
	5.3 Range-Doppler Imaging Simulations	90
<u>APPENDIX</u>		
A	MATHEMATICAL FORMULATION OF SPECKLE SIMULATION	111
B	EFFECT OF NOISE ON RECEIVED SIGNAL	114
C	ATMOSPHERICS	122
D	RANGE-DOPPLER IMAGING RADAR SYSTEM	123
E	BI-WAVELENGTH RANGE-DOPPLER IMAGING SYSTEM ANALYSIS	132

## FIGURES

<u>NO.</u>		<u>PAGE</u>
2-1	System Elements and Information Planes Along Propagation Path	2
2-2	Basic Elements of Speckle Model	4
2-3	Curves of $\sigma_N$ vs. $C_N^2$ Showing the Effects of Model Parameters on the Magnitude of the Phase Variations	7
2-4	Empirical Modeling of the Atmosphere	9
3-1	Functional Flow Diagram for the Sensor System Model	16
3-2	Gray-Scale Images of a Point Source at 3 dB per Level	19
4-1	Approximate Geometry of Meteor Satellite	21
4-2	Distributed Cross Sections for the Meteor Spacecraft at Various Aspect Angles	22
4-3	Total Cross Section of Meteor Satellite at Various Aspect Angles	23
4-4	Outline Drawing of Styx Cruise Missile	25
4-5	Distributed Cross Sections for the Styx Cruise Missile at Various Aspect Angles	26
4-6	Total Cross Section vs. Aspect Angle for Styx Cruise Missile	27
4-7	SLBM Outline Drawing	28
4-8	Distributed Cross Sections for an SLBM Booster at Various Aspect Angles	29
4-9	Total Cross Section vs. Aspect Angle for SLBM Booster	30
4-10	Outline Drawing of Reentry Vehicle	31
4-11	Distributed Cross Sections for a Reentry Vehicle at Various Aspect Angles	32
4-12	Total Cross Section vs. Aspect Angle for Reentry Vehicle	33

# FIGURES (Cont.)

<u>NO.</u>		<u>PAGE</u>
4-13	A Sequence of Meteor Spacecraft Distributed Cross Sections Which Include the Effects of Finite Resolution	35
4-14	The Effect of Diffuse Speckle for Two Views of the Meteor Spacecraft	36
4-15	Speckle Effects on Doppler-Resolved Cross Section	38
4-16	Non-Coherent Averaging of Doppler-Resolved Cross Sections	39
4-17	Signal Characteristics of a Rotating Sphere	41
4-18	A Sequence of Distributed Cross Sections of a Meteor Spacecraft Which Include the Effects of Finite Resolution and Diffuse Speckle	43
4-19	Distributed Cross Section of Meteor Satellite at $\theta = 65^\circ$ Showing Burned Area	45
4-20	Doppler-Resolved Cross Section of Meteor	47
4-21	Distributed Cross Section of RV at $\theta = 90^\circ$ Showing Burned Area	49
4-22	Doppler-Resolved Cross Section of RV	50
4-23	Sequence Illustrating the Effect of Finite SNR on Distributed Cross Sections of the Meteor	51
4-24	A Sequence of 3 dB/Level Gray-Scale Images of the Far-Field Diffraction Pattern of a Circular Aperture for Various Turbulence Levels	53
4-25	Intensity Contour Maps of the Resolved Image of Uniformly Illuminated Two-Point Target	54
4-26	Intensity Contour Maps of the Unresolved Image of a Uniformly Illuminated Two-Point Target	55
4-27	Gray-Scale Direct Detected Images of a Meteor Satellite for Three Levels of Turbulence	56
5-1	Encounter Between Ground-Based Radar and a Satellite	66
5-2	Encounter Between Satellite-Borne Radar and a Satellite	68

# FIGURES (Cont.)

<u>NO.</u>		<u>PAGE</u>
5-3	Encounter Between Satellite-Borne Radar and a Booster Rocket Near Launch	70
5-4	Encounter Between Satellite-Borne Radar and an RV	71
5-5	Total Cross Section After Minimum Approach Observed by Ground-Based Radar for Satellite Encounter	73
5-6	Total Cross Section Observed by Ground-Based Radar During Satellite Encounter	75
5-7	Total Cross Section Observed by Satellite-Borne Radar During Satellite Encounter	77
5-8	Range vs. Time Comparisons for Co- and Counter-Rotating Satellite-Satellite Encounter	79
5-9	Total Cross Section Observed by Radar During Cruise Missile Encounter	82
5-10	Total Cross Section Observed During Radar Encounter with Booster Rocket	84
5-11	Total Cross Section Observed During Radar Encounter with Spinning RV	87
5-12	Minimum Value of Total Cross Section Observed During Radar Encounter with Tumbling RV	89
5-13	Noise- and Speckle-Free Range-Doppler Images of the Meteor Satellite at Four Ranges from a Ground-Based Observer	93
5-14	The Effect of Finite Signal-to-Noise Ratio (SNR) and Speckle on the Range-Doppler Image Corresponding to Fig. 5-13	95
5-15	Effect of System and Transmission Losses on Maximum Signal-to-Noise Ratio	97
5-16	Behavior of Maximum Signal-to-Noise Ratio for Scenario 1	98
5-17	Number of Range-Doppler Images to be Averaged vs. Probability of Detection and Signal-to-Noise Ratio	100
5-18	"Separation of Means" Criterion for Detection of Signal Above Noise	101
5-19	Limits on Averaging by Target Feature Translation	102

# FIGURES (Cont.)

<u>NO.</u>		<u>PAGE</u>
5-20	Contrast Ratio of Two Image Elements vs. Probability of Discerning Contrast and Signal-to-Noise Ratio of Dimmer Element	104
5-21	Image Enhancement by Averaging	105
5-22	Noise- and Speckle-Free Range-Doppler Images of the Meteor Satellite at Two Ranges from a Satellite-Borne Radar	107
5-23	Noise- and Speckle-Free Range-Doppler Images of the Meteor Satellite at Six Ranges from a Satellite-Borne Radar	108
B-1	Heterodyne Laser Receiver (Through IF Detector Stage)	115
D-1	Coordinate System Definition	125
D-2	Transformation-Induced Range-Doppler Ambiguities	125
E-1	System Concept	134
E-2	Superposition of CW and Mode-Locked Laser Ambiguity Functions	152
E-3	Central Peak of Mode-Locked Laser Ambiguity Function	153
E-4	Hypothetical Ambiguity Function Used in Computer Simulations	154
E-5	Representation of a Four Point Target in Range-Doppler Space	155
E-6	Representation of the Meteor Satellite in Range-Doppler Space	156
E-7	Range-Doppler Image of Four Point Target	157
E-8	Range-Doppler Image of Meteor Satellite	158

## TABLES

<u>NO.</u>		<u>PAGE</u>
4-1	Parameters Associated with Images Shown in Figure 4-18	44
4-2	Description of Atmospheric Effects on System Observables	62
5-1	Encounter Simulator Program Input Parameters	65
5-2	Apparent Satellite Rotation Rates Seen by Radar for Scenario 1	76
5-3	Apparent Satellite Rotation Rate Seen by Radar for Scenario 2a with $\beta = 0^\circ$	80
5-4	Apparent Missile Rotation Rate Seen by Radar for Scenario 2b with $\beta = 20^\circ$	83
5-5	Apparent Booster Rocket Rotation Rates Seen by Radar for Scenario 2c	86
5-6	Comparison of Assumed Parameters for Two Range-Doppler Imaging Radars	92

## EVALUATION

Military sensor systems must be capable of functioning effectively in a "real world" environment. Many active infrared systems are potential and current candidates for application in the area of future military surveillance systems as spelled out in RADC Technology Program Objectives (TPO-5). General Research Corporation, (GRC) has looked at a reasonable number of likely scenarios and delved into the potential problem areas. The results are encouraging and illustrative of the pitfalls to be avoided. RADC is continuing the Sensor Modelling Study to increase the pay-off to would be systems applications. Details will be released upon request to RADC/OCTM (Donald F. McKee), Telephone Number: AC 315 330-3445.

*Donald F. McKee*

DONALD F. McKEE  
Project Engineer

## 1 INTRODUCTION

The fundamental concept of a target signature usually stems from a desire to associate a target property of interest with a measurable parameter. Although the target property or feature represents a constant physical entity, the observable parameter by which an attempt is made to evaluate it need not remain constant. Indeed the parameter may change as the target, engagement scenario, propagation conditions, and observing system elements are varied.

The state of any observable parameter undergoes various changes or degradations prior to detection. For a laser radar system, the complex electromagnetic field that is returned from the target is subject to spurious modulation as it propagates through any intervening atmosphere and the receiver optics. The state of the field that is incident upon the detector plane, while not a physical observable, is of prime importance for evaluating possible signature concepts or effects. All of the system elements preceding this plane are to a large extent beyond the influence of the observer. The existence of an observable at the detector plane of the receiver optics, however, does not necessarily guarantee that the information will exist in the electrical signal of the detector output. The extent to which the desired information does exist and how it may vary is the topic of this report.

This report is organized according to the enumerated system interfaces/effects outlined in Sec. 2. Section 3 describes the two main computer models used to simulate and evaluate the system effects. The main targets evaluated are described in Sec. 4, along with several examples of system effects on ideal signatures. Section 5 deals with the influence of scenario factors on signature characteristics.

## 2 INTERFACES AND EFFECTS STUDIED

The operation of a laser radar system involves the interaction of the transmitted field, target geometry and dynamics, propagation path characteristics, receiver optics, detection element, and post-detection processing. This interaction is indicated in Fig. 2-1, which illustrates the major signal-modifying elements and important information planes along the propagation path. The information planes defined are those at which the computer models either require input data or calculate the signal characteristics as output. Section 2.1 outlines the methods of formulating the system performance and including the effects of the target propagation to the receiver aperture and heterodyne detection. Section 2.2 describes the method used for introducing the effects of the atmosphere on the signal propagation.

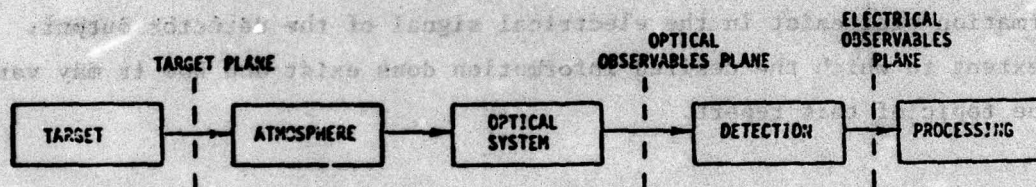


Figure 2-1. System Elements and Information Planes Along Propagation Path

## 2.1 DESCRIPTION OF SYSTEM EFFECTS

The mathematical formulations underlying the computer simulations of system effects are briefly reviewed here. More details are presented in Appendix A. Figure 2-2 shows the basic elements of the target and receiver system. The actual (three-dimensional) target is projected onto the xy plane which is perpendicular to the observer's line of sight. In this plane, the target is modeled as a collection of point sources. The field scattered from each point source is a complex quantity with a magnitude equal to the square root of the cross section represented by the scattering center and a phase that is usually a randomly distributed variable. For the case of a diffuse surface, the phase is a random variable uniformly distributed between 0 and  $2\pi$ . For surface structure with peak deviations that are on the order of a wavelength or less, the distribution of the phase would require modifications. In addition to the initial phase at time  $t = 0$ , the instantaneous phase  $\phi_1$  is frequency shifted due to the rotation of the target.

By the standard methods of Fourier optics (see Appendix A), the field in the target plane can be transformed to the pupil and image (detector) planes. Neglecting atmospheric effects and losses in the optics of the receiver, the additional parameters range (R), aperture diameter (D), and focal length (f) are introduced by the transformation. The field in the image plane then displays the statistical properties associated with scattering from a rough target (speckle) and the blurring effects of the finite aperture. The spatial resolution of the receiver system is taken as  $1.22 R\lambda/D$  at wavelength  $\lambda$ .

For Doppler- and range-resolved cross-section calculations, a point detector is assumed so that blurring (spatial resolution) effects are not relevant. The output of a square-law detector viewing a diffuse object is known to be an exponentially distributed random variable. Therefore, the proper statistical behavior of Doppler- or range-resolved measurements can be obtained by treating the observable signal appearing in each Doppler

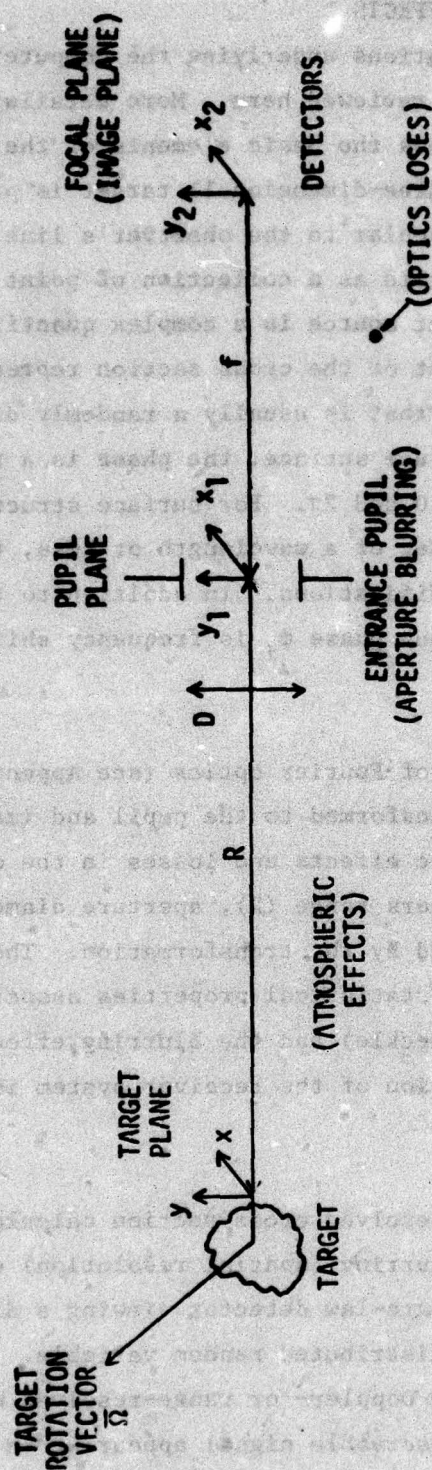


Figure 2-2. Basic Elements of Speckle Model

(or range) bin as an exponentially distributed random variable with both mean value and variance given by the Doppler- (or range-) resolved cross section in the absence of speckle effects. The calculation of these latter values is discussed in Sec. 3.

In order to reduce the effect of speckle on cross-section measurements, some form of averaging is desirable. In the case of a point detector, the receiver samples only one speckle lobe at a time. For a target of maximum extent  $L$ , at range  $R$ , rotating with angular velocity  $\omega$  (both  $L$  and the spin axis assumed perpendicular to the observer's line of sight), the speckle lobes are of extent  $\lambda R/L$  at the receiver and sweep past with velocity  $2\omega R$ . The received signal becomes uncorrelated in a time on the order of  $\lambda/2\omega L$ . Even for a small ( $L \sim 1$  m), slowly rotating target ( $\omega \sim 1$  mrad/sec), this time is only 5 msec. Since the target aspect angles are essentially unchanged in a short interval, successive point detector measurements can be averaged.

The statistics of a quantity which is the average of  $N$  independent exponentially distributed random variables are governed by the gamma distribution function. From probability theory, the gamma distributed random variable has the same average value as the exponentially distributed random variables, but its variance is reduced by a factor of  $N$ . For most of the scenarios studies in Sec. 5, the total cross section does not change rapidly with time and non-coherent averaging is possible.

An additional effect which combines with speckle to obscure the target signal is receiver noise. Assuming an optimized heterodyne detection process, the principal noise source is the shot noise of the local oscillator. In Appendix B, it is shown that the shot noise simply increases the mean value (and, hence, the variance) of the exponentially distributed output of the square-law detector. The amount of increase is proportional to the signal-to-noise ratio and may also be expressed in terms of a noise equivalent cross section.

## 2.2 ATMOSPHERIC TURBULENCE

The effect of atmospheric turbulence on a received laser beam wavefront is included in system calculations by generating a two-dimensional array of phase fluctuations induced by the atmosphere at the entrance pupil plane of the receiver. The inclusion of such an array at the pupil plane accounts for most of the phase variations caused by propagation through the turbulent atmosphere. While not including amplitude variations due to propagation from turbulent layers at high altitudes, such effects are of secondary importance for the laser radar system and scenarios of interest.

The array of phase fluctuations is computed from the convolution of a set of zero-mean, normally distributed random numbers with the autocorrelation of the spatial frequency distribution for the propagation path under consideration. This autocorrelation is the Fourier transform of the spatial frequency spectrum (assumed to be modified von Kármán). For the simulation, the spectrum was approximated by a  $\kappa^{-4}$  dependence (where  $\kappa$  = spatial frequency) with a sharp cut-off at  $\kappa = 2\pi/L_0$ , corresponding to the outer scale of turbulence. The variance for the phase fluctuations is derived in Appendix C and is given by

$$\sigma_n^2 = 0.0087k^2 C_n^2 d L_0^{5/3} \quad (2-1)$$

where  $k$  = wave number  $2\pi/\lambda$

$C_n^2$  = refractive index structure parameter

$L_0$  = outer scale of turbulence

$d$  = effective width of phase perturbing region

$\sigma_n$ , based on Eq. 2-1, is plotted in Fig. 2-3 vs.  $C_n^2$  for several values of  $d$  and  $L_0$ . As is illustrated by the curves, a particular value for the phase variance can be obtained from numerous sets of the other three parameters. In Sec. 4.8 the turbulence levels for the example images and diffraction patterns are described by values of  $\sigma_n$ .

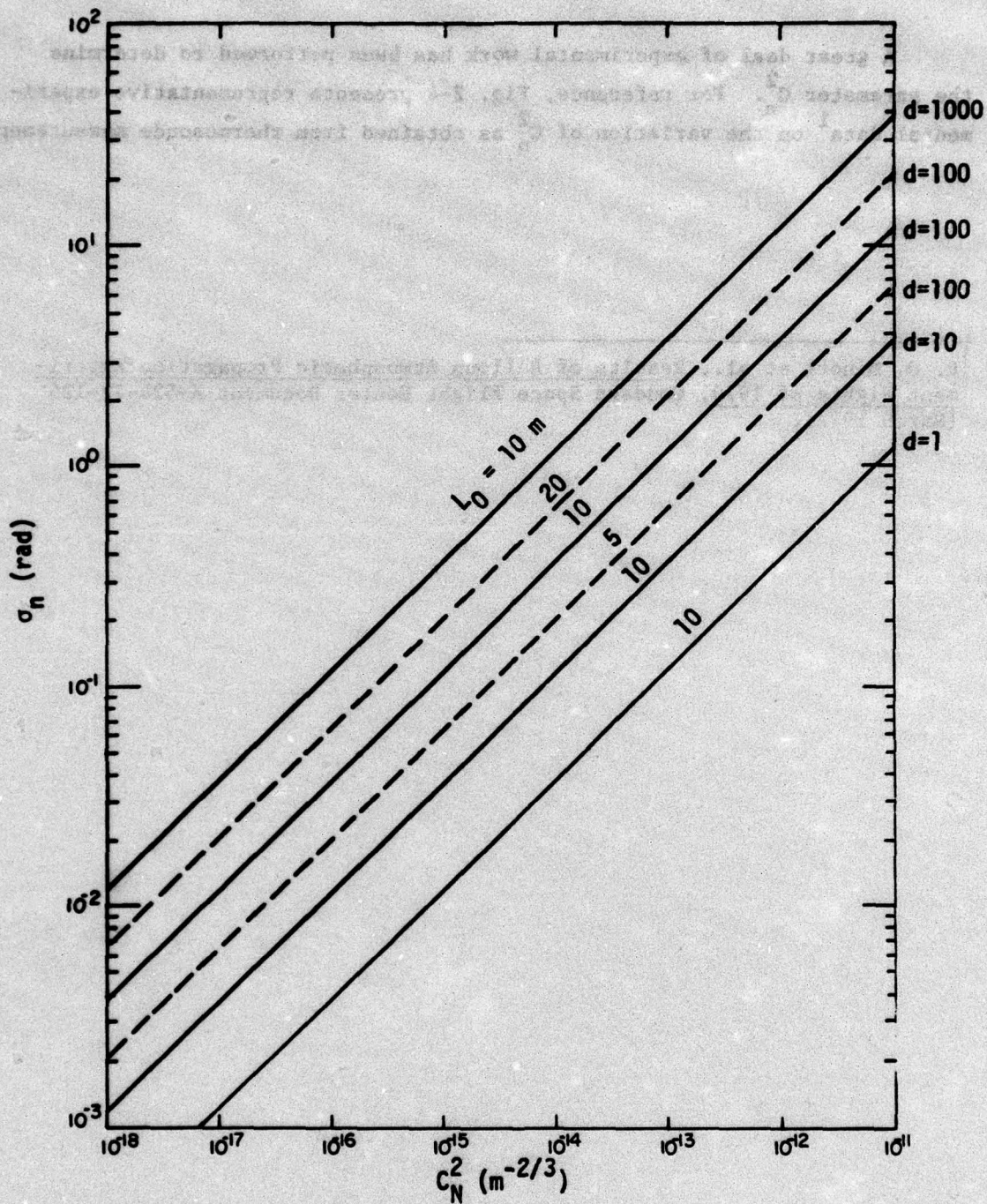


Figure 2-3. Curves of  $\sigma_n$  vs.  $C_N^2$  Showing the Effects of Model Parameters on the Magnitude of the Phase Variations

A great deal of experimental work has been performed to determine the parameter  $C_n^2$ . For reference, Fig. 2-4 presents representative experimental data<sup>1</sup> on the variation of  $C_n^2$  as obtained from thermosonde measurements.

<sup>1</sup>P. O. Minott et al., Results of Balloon Atmospheric Propagation Experiment Fights of 1970, Goddard Space Flight Center Document X-524-72-125 (March 1972).

Figure 2-4. Curves of  $C_n^2$  vs.  $h$  showing the effect of height on the magnitude of the refractive index variations.

REFRACTIVE-INDEX-STRUCTURE CONSTANT AS A  
FUNCTION OF HEIGHT ABOVE GROUND LEVEL.  
1:00 AM MST 21 OCTOBER 1970 AT HOLLOMANAFB  
NEW MEXICO. BAPE 1 EXPERIMENT

- + DATA POINTS OBTAINED BY TATARSKI'S  
METHOD OF MEAN TEMPERATURES
  - DATA POINTS OBTAINED FROM THERMOSONDES  
MEASUREMENT
  - EXPERIMENTAL DEPENDENCE OF  $C_n^2$  UPON  
ALTITUDE
  - MATHEMATICAL MODEL USED TO REPRESENT  
EXPERIMENTAL DATA  
 $C_n^2 = C_{no}^2 h^{-1/3} e^{-h/h_0}$   
 $C_{no}^2 = 4.0 \times 10^{-14} \text{ m}^{-2/3} \quad h_0 = 1000 \text{ m.}$
- GROUND LEVEL 1.2X10<sup>3</sup> m. ABOVE MSL

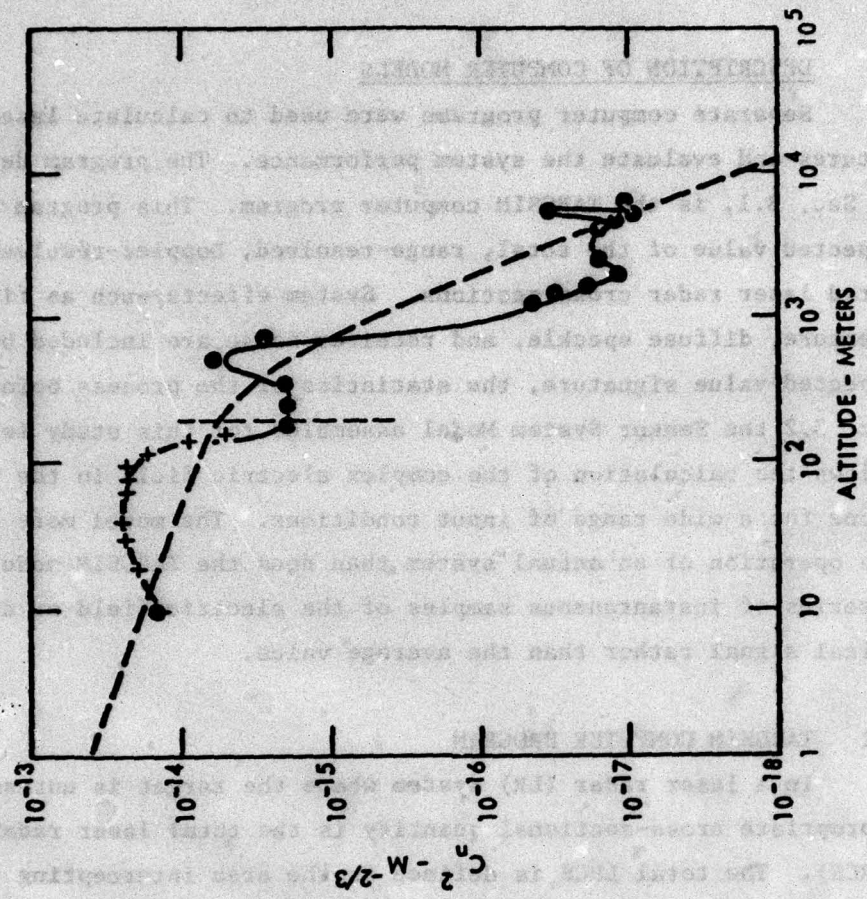


Figure 2-4. Empirical Modeling of the Atmosphere

### 3 DESCRIPTION OF COMPUTER MODELS

Separate computer programs were used to calculate laser radar signatures and evaluate the system performance. The program described first, in Sec. 3.1, is the TARGSIM computer program. This program calculates the expected value of the total, range-resolved, Doppler-resolved and distributed laser radar cross sections. System effects such as finite receiver aperture, diffuse speckle, and receiver noise are included by modifying the expected-value signature, the statistics of the process being known. In Sec. 3.2 the Sensor System Model assembled for this study is described. It allows the calculation of the complex electric field in the receiver focal plane for a wide range of input conditions. The model more closely parallels the operation of an actual system than does the TARGSIM model. It calculates a series of instantaneous samples of the electric field or detected electrical signal rather than the average value.

#### 3.1 TARGSIM COMPUTER PROGRAM

In a laser radar (LR) system where the target is unresolved, the appropriate cross-sectional quantity is the total laser radar cross section (LRCS). The total LRCS is defined as the area intercepting that amount of power which, when scattered equally in all directions, produces a scattered power density at the receiver equal to that produced by the target; or

$$E_1 \sigma = E_2 (4\pi Z_1^2) \quad (3-1)$$

where

$E_1$  = irradiance incident on the target

$E_2$  = (uniform) scattered irradiance at range  $Z_1$

$4\pi Z_1^2$  = area of the spherical surface at distance  $Z_1$  from the target

$\sigma$  = total LRCS

The cross section of rough, diffuse targets is usually calculated using the bidirectional reflectance (BDR) of the material and appropriately summing the contributions from all parts of the target. If the surface is rough, the phase of the radiation scattered by nonoverlapping macroscopic

subregions is uncorrelated, and the total power scattered by any region of the target is the sum of the power scattered by each subregion. For a small, approximately flat portion of the surface, the elemental cross section in the monostatic geometry for a polarization-insensitive, isotropic scatterer can be written

$$\delta\sigma = 4\pi\rho(\theta) \cos^2 \theta \delta A \quad (3-2)$$

where  $\theta$  is the angle between the surface normal and the vector line of sight (VLOS),  $\delta A$  is the area of the surface element, and  $\rho$  is the BDR. The cross-sectional contribution of any region of the target is

$$\Delta\sigma = 4\pi \iint_S M(\vec{r}) \rho\{\theta(\vec{r})\} \cos^2 \theta(\vec{r}) dA \quad (3-3)$$

where  $\vec{r}$  is the position of the surface area element  $dA$ ,  $S$  is the region of interest of the target surface, and  $M(\vec{r})$  is a "mask" function equal to unity if the surface element is facing towards the source/observer and is unshadowed by other parts of the target and is equal to zero otherwise.

The TARGSIM computer model has been developed to calculate total LRCS and resolved (Doppler, range distributed) LRCS signatures. The approach chosen to deal with arbitrarily complex targets at arbitrary viewing angles is to divide the target up into small pieces. If the pieces are small enough such that the integrand of Eq. 3-3 can be considered approximately constant over the area of each piece, the integration can be replaced by a summation over the appropriate region of the target. For modeling a complex target, the program synthesizes the required subarea decomposition data from a simplified input data list. The component surfaces of the target are described in terms of type, orientation, size, and location in relation to the Cartesian target coordinate systems (TCS). The aspect angle used to specify the VLOS for a particular signature calculation is referenced to the TCS. The zenith angle ( $\theta$ ) is measured from the positive  $z$  axis. The azimuthal angle is measured in the  $x$ - $y$  plane, referenced to the positive  $x$  axis.

The general flow of the program is as follows:

1. Decompose target into subareas and store all subarea data.
2. For each subarea, retrieve descriptive data, calculate relevant quantity to be associated with that subarea (e.g., its incremental LRCS) and store the result.
3. In a second pass over the subarea data, process each stored value in a manner appropriate to the signature desired (e.g., for total LRCS, sum all incremental subarea LRCSs).

While the successive storage and retrieval of various types of stored data may seem somewhat unnecessary, this approach leads to a highly flexible, modularized program allowing development and modification of one section of the code with little or no change to portions of the code preceding or following in the execution sequence. Furthermore, the storage process allows minimization of computer storage requirements while resulting in only very modest increases in execution time.

The two subarea-associated quantities which are relevant to the calculation of the signatures are the elemental cross section and normalized radiance of each subarea. The subarea cross section is calculated using Eq. 3-2. The value of experimentally measured BDR is found by linear interpolation between tabled values of  $\rho$  found using a table-search technique. The normalized subarea radiance is calculated using

$$L_i = \rho(\theta_i) \cos \theta_i \quad (3-4)$$

The target's total LRCS is calculated by summing the individual cross-section contributions of each of the unmasked subareas. For random rough (diffuse) surfaces, this process is valid since the scattered radiation from each subarea is completely uncorrelated; hence a simple power summation is sufficient.

The range-resolved LRCS is the distribution of the target LRCS along the VLOS. Since the round-trip transit time of the signal depends on the range to any target element, the range distribution of LRCS can also be considered the distribution in delay; the units of cross-section density would be  $\text{m}^2/\text{sec}$ . Another way of representing the distribution is to integrate the density over finite ranges of delay time. This is equivalent to placing the target's LRCS in "bins" by gating the returned signal and integrating. This latter representation is employed in the TARGSIM program because it is more amenable to numerical computation. In addition, all real systems will be constrained to sample a finite region of the target by virtue of the non-infinite resolution of the system. Analytically, the range-distributed LRCS can be represented by Eq. 3-3, with the surface of integration restricted to that part of the target surface lying between the planes

$$z = z_1 - \Delta z/2 \quad \text{and} \quad z = z_1 + \Delta z/2 \quad (3-5)$$

where  $z = \text{range}$

$z_1 = \text{center of the } i\text{th range bin}$

$\Delta z = \text{range resolution.}$

The range resolution can be found using

$$\Delta z = c\tau/2 \quad (3-6)$$

where  $c = \text{light speed}$

$\tau = \text{effective}^1 \text{ pulse width}$

### 3.1.1 Doppler-Resolved LRCS

The Doppler-distributed cross section is the projection of the target's LRCS along an axis mutually perpendicular to the VLOS and the target's

---

<sup>1</sup>For transmitted waveforms with time-bandwidth products greater than unity, the effective pulse width is equal to the waveform's reciprocal bandwidth.

instantaneous rotation axis. The Doppler distribution of LRCS arises as follows. A target element moving a radial velocity,  $\Delta v$ , can be considered to shift the frequency of the backscattered radiation ( $\nu_0$ ) by an amount

$$f_D = \frac{2\nu_0}{c} v = \frac{2}{\lambda} \Delta v \quad (3-7)$$

If the target is rigid and rotating, the velocity of a point on the target is

$$\Delta v = v_t + \omega x \sin \phi \quad (3-8)$$

where  $v_t$  = translational velocity of the body's center of mass  
 $\omega$  = rotation rate  
 $x$  = distance from the target point to the plane formed by the VLOS and spin axis  
 $\phi$  = angle between the VLOS and the spin axis

Neglecting the simple fixed frequency shift caused by target translation, the Doppler shift can be written

$$f_D = \frac{2\omega}{\lambda} x \sin \phi \quad (3-9)$$

Since the radiation scattered by a section of target at cross-range distance  $x$  is shifted in frequency by the amount given in Eq. 3-9, the Doppler-distributed LRCS can be considered the cross-range distribution.

In a manner similar to the range distribution, the Doppler distribution can be represented by Doppler bins (corresponding to the outputs of a bank of ideal Doppler filters, each centered at a different frequency). The Doppler-distributed LRCS can then be represented by Eq. 3-3 with the surface of integration restricted to that part of the target's surface lying between the planes

$$x = \frac{\lambda}{2\omega \sin \phi} \left( f_1 - \frac{\Delta f}{2} \right)$$

and

(3-10)

$$x = \frac{\lambda}{2\omega \sin \phi} \left( f_1 + \frac{\Delta f}{2} \right)$$

where  $\Delta f$  is the frequency resolution of the system.

The distributed cross section is calculated from the normalized target radiance. The cross section for that portion of the target falling within the projection of a unit normal area can be found by integrating the target radiance over that area. If the target radiance is approximately constant over that area, the resolution cell contains a cross section

$$\Delta \sigma_k = 4\pi \Delta A_k \langle L_k \rangle \quad (3-11)$$

where  $\Delta A_k$  is the cell's area normal to the VLOS and  $\langle L_k \rangle$  is the average radiance of the target within that cell. The target radiance within a given cell is determined by projecting the calculated radiance of each sub-area onto an array of image cells. Since the distributed LRCS is a projection of the target's radiance on a plane perpendicular to the line of sight, it is essentially analogous to the angle-angle type images produced by a conventional telescope.

### 3.2 SENSOR SYSTEM MODEL

A computer simulation program, referred to as the Sensor System Model, has been assembled to calculate the response of a laser transceiver system for a wide variety of input conditions. The program was developed largely by combining and integrating all or part of existing computer models. A block diagram of the model is illustrated in Fig. 3-1.

The model performs the same basic calculations as described in Appendix A for speckle phenomena, the major difference being that the system

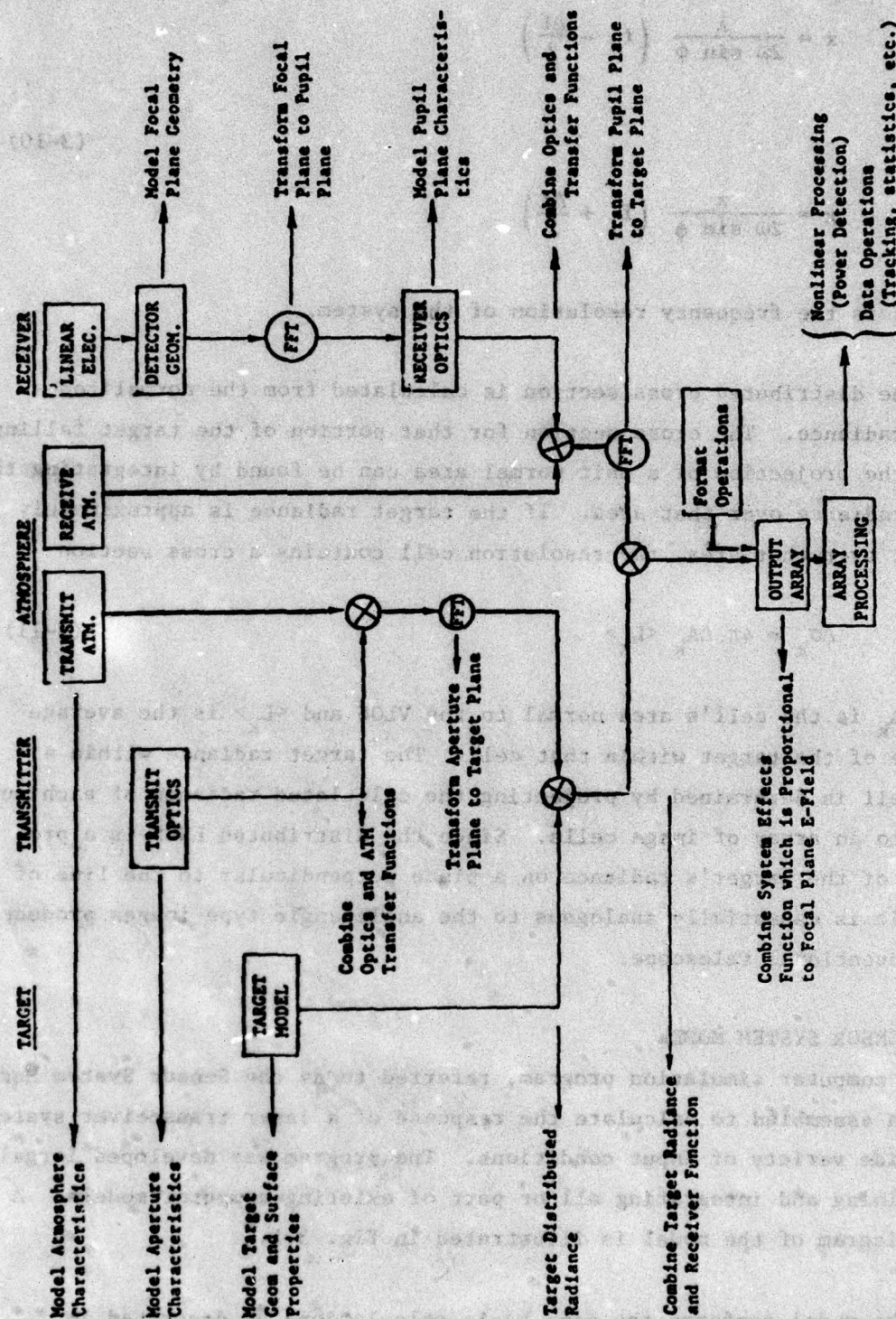


Figure 3-1. Functional Flow Diagram for the Sensor System Model

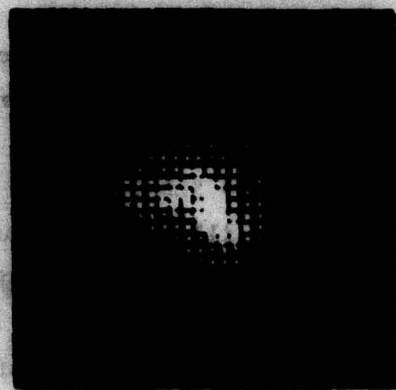
response function is calculated for the focal plane geometry and combined with the scattered electric field from the object in the target plane. Use of the fast Fourier transform (FFT) algorithm allows the calculation to be made for arbitrary focal plane and aperture plane geometries.

Modeling of the target involves using a routine from the TARGSIM program previously described to generate a three-dimensional array describing the geometry and reflectance properties of the target. At the aspect angle of interest, the target is projected onto a plane normal to the line of sight as a two-dimensional array of point scatterers. The initial phase of the scatterers is uniformly distributed between 0 and  $2\pi$ . Rotation of the target about some axis causes a time modulation of the instantaneous phase of the scatterers. The response at a point or area in the focal plane of an optical system is calculated by combining the array of scatterers composing the target with the system response function. This function includes all of the optical effects that are introduced by the propagation path, receiver (and transmitter) optics, and the focal plane geometry. If desired, certain post-detection processes can be included as well. The length of time over which the calculations can correspond are restricted by the duration of the validity of the time-varying atmospheric model, and by the restriction that no apparent change in target aspect angle be allowed.

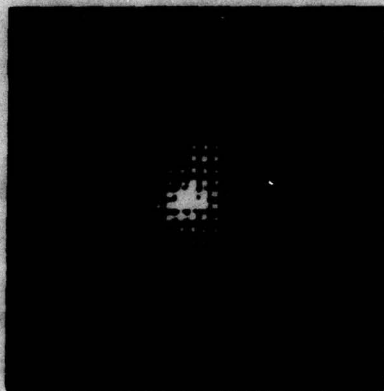
Pointing jitter is included in the simulation by generating a time-correlated series of numbers representing the jitter of the optical axis of the laser receiver about some mean pointing direction. The jitter in the x and y directions in the model is uncorrelated. The required inputs for the model are the probability distribution function for the angular pointing deviations (assumed to be zero-mean Gaussian) and a power spectrum of the uncompensated induced noise perturbations of the optical line of sight. In an actual pointing system, this spectrum would be a function of many factors including servo loop gains, the spectrum of input vibrations,

gimbal static friction, and transmissivity of the mounts. For this study no model for generating a pointing error signal was incorporated; therefore closed-loop simulation was not attempted. Rather than consider a specific pointing system complete with detailed information for all input parameters, a representative jitter spectrum was used for the purposes of checking out and illustrating the model outputs.

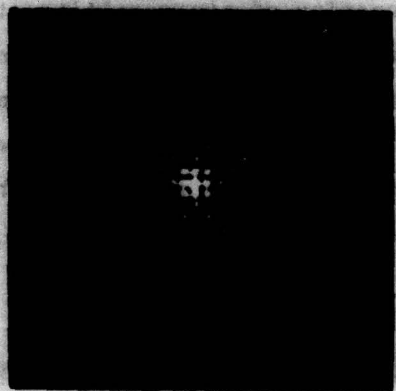
As an example of the output of the sensor system model with and without jitter effects, images of a point source are presented in Fig. 3-2 which represent the output of a direct detection imaging system. In such a system there will be some finite detector response time. Any random movement of the optical system at a rate which is slower than the detector response time will not affect the image quality. Movement which is faster than the detector response time, on the other hand, will appear as a resolution degradation factor. This effect is illustrated in Fig. 3-2. The image in Fig. 3-2A is the familiar Airy pattern of a point source with no jitter included. Figs. 3-2B and 3-2C show the same image for the cases of a pointing jitter standard deviation of 3  $\mu$ rad and 5  $\mu$ rad, respectively. For the jitter spectrum used and the 20-msec duration of the image exposure, 20 independent jitter samples are contained in the images.



(A)



(B)



(C)

Figure 3-2. Gray-Scale Images of a Point Source at 3 dB per Level. Figure A shows the image obtained with no jitter present. Figures B and C show the same image for the cases of 3  $\mu$ rad and 5  $\mu$ rad pointing jitter, respectively.

#### 4 CASE STUDIES

The computer models described in the previous section were exercised to produce a representative sample of effects encountered in laser detection systems. Four targets were used in the analysis: (1) a satellite (Meteor), (2) cruise missile (Styx), (3) SLBM, and (4) an RV. The target geometries used in the simulations and illustrated below are approximations and are not meant to be exact replicas of a particular vehicle. The effects presented in this section were not tied to any specific scenario involving the targets and laser system; the modeling of scenarios is discussed in Sec. 5. All of the results are at  $10.6 \mu\text{m}$  and for copolarized transmitter and receiver.

##### 4.1 DESCRIPTION OF TARGETS

###### 4.1.1 Meteor Satellite

A drawing of the satellite model is shown in Fig. 4-1. The satellite has two large solar paddles (each 2.4 m by 2.4 m in extent) on opposite sides of the central cylindrical section. The solar paddles were covered on one side with a glinty material (maximum BDR  $5000 \text{ sr}^{-1}$ , effective width  $1.5^\circ$ ). The other side of the paddles and the rest of the satellite were coated with white paint.

The distributed cross section of the satellite at six aspect angles is shown in Fig. 4-2. Aspect angles normal to the glinty side of the solar paddles were avoided since they show a return only from the paddles and do not illustrate the satellite structure. The distributed cross section for viewing normal to the painted side of the paddles is shown at the aspect angles  $\theta = 120^\circ$ ,  $\phi = 180^\circ$ . Aspect angles are measured relative to the x, y, z coordinate system as shown in 4-1.

The total cross section of the satellite at various aspect angles is shown in Fig. 4-3. Except for the returns near normal incidence to the solar paddles, the total cross section is less than about  $2 \text{ m}^2$ . The diffuse nature of white paint causes the broad peak in cross section for

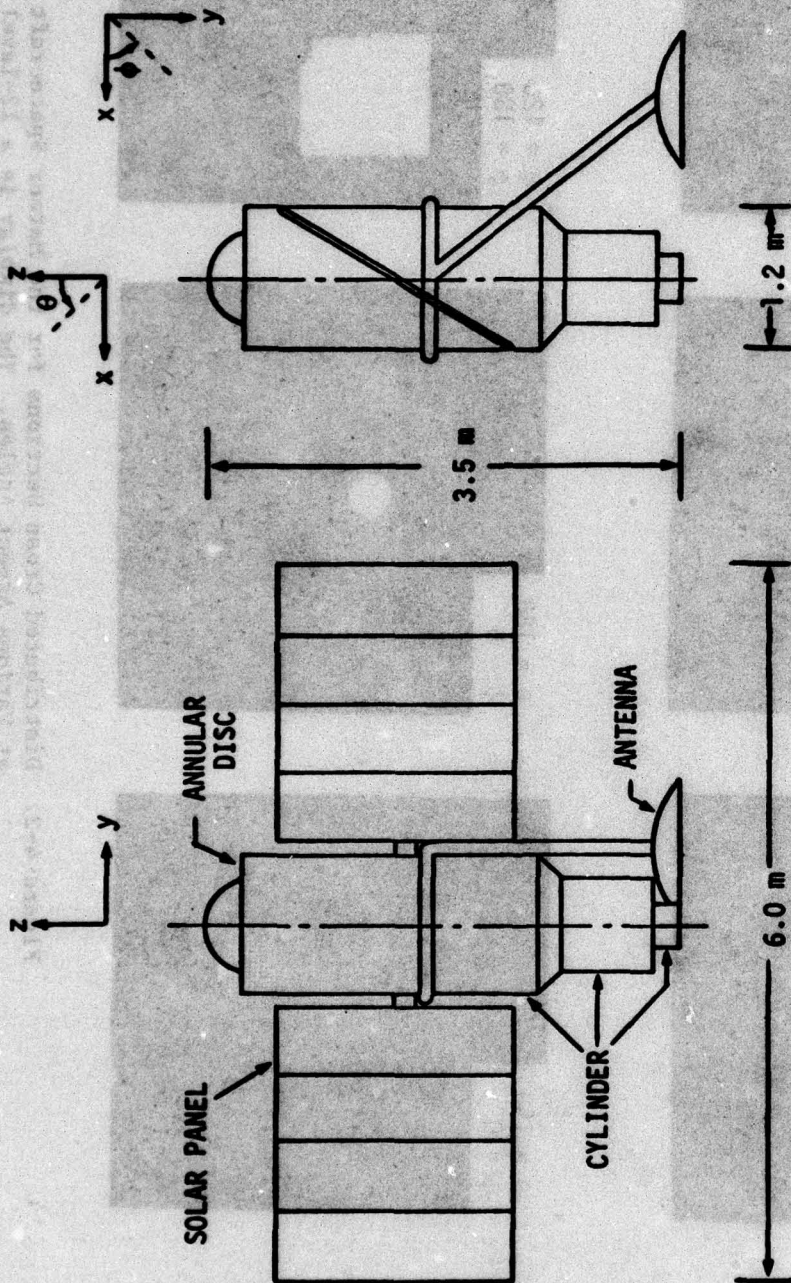


Figure 4-1. Approximate Geometry of Meteor Satellite

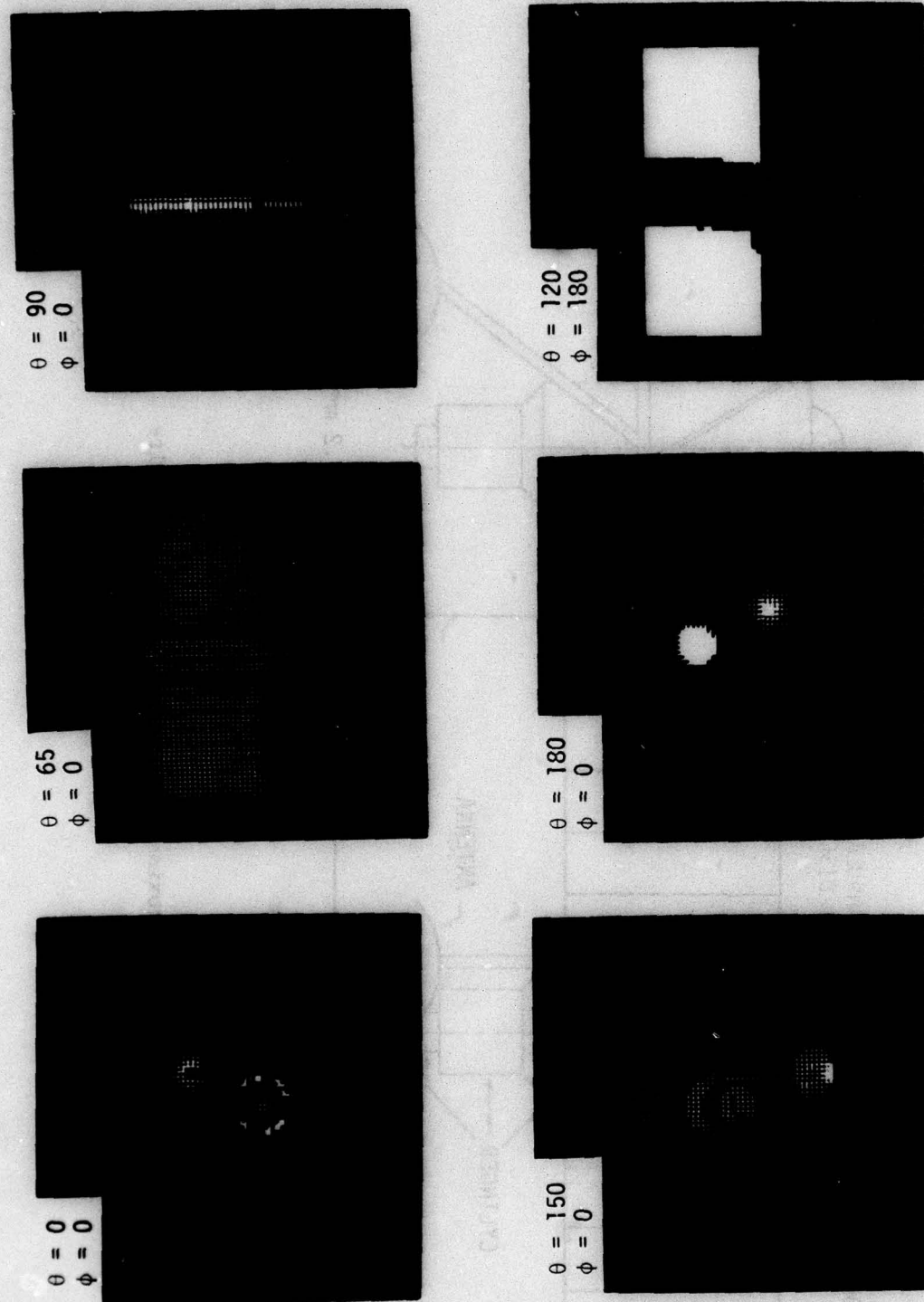


Figure 4-2. Distributed Cross Sections for the Meteor Spacecraft at Various Aspect Angles. The display is a 12-level gray scale with approximately a 30 dB dynamic range from white to black.

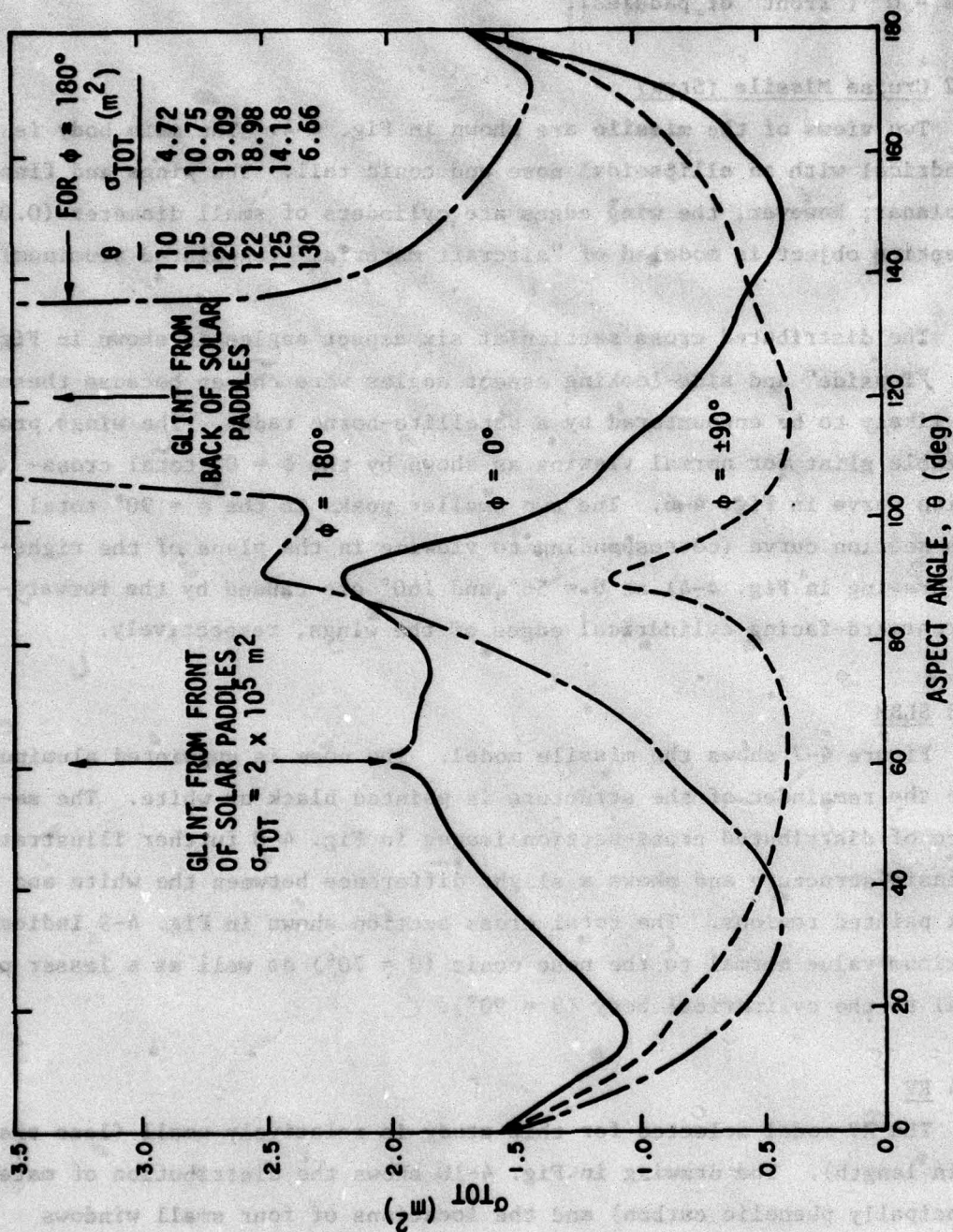


Figure 4-3. Total Cross Section of Meteor Satellite at Various Aspect Angles

$\phi = 180^\circ$  ("back" of paddles) contrasted with the delta-function-like glint for  $\phi = 0^\circ$  ("front" of paddles).

#### 4.1.2 Cruise Missile (Styx)

Two views of the missile are shown in Fig. 4-4. The main body is cylindrical with an ellipsoidal nose and conic tail. The wings and fins are planar; however, the wing edges are cylinders of small diameter (0.04 m). The entire object is modeled of "aircraft material" (unpainted aluminum).

The distributed cross section at six aspect angles is shown in Fig. 4-5. "Topside" and side-looking aspect angles were chosen because these are most likely to be encountered by a satellite-borne radar. The wings produce a sizable glint for normal viewing as shown by the  $\phi = 0^\circ$  total cross-section curve in Fig. 4-6. The two smaller peaks in the  $\phi = 90^\circ$  total cross-section curve (corresponding to viewing in the plane of the right-hand drawing in Fig. 4-4) at  $\theta = 56^\circ$  and  $160^\circ$  are caused by the forward- and rearward-facing cylindrical edges of the wings, respectively.

#### 4.1.3 SLBM

Figure 4-7 shows the missile model. The nose is unpainted aluminum, while the remainder of the structure is painted black or white. The sequence of distributed cross-section images in Fig. 4-8 further illustrates the basic structure and shows a slight difference between the white and black painted regions. The total cross section shown in Fig. 4-9 indicates a maximum value normal to the nose conic ( $\theta = 70^\circ$ ) as well as a lesser peak normal to the cylindrical body ( $\theta = 90^\circ$ ).

#### 4.1.4 RV

The RV model selected for this study is relatively small (less than 2 m in length). The drawing in Fig. 4-10 shows the distribution of materials (principally phenolic carbon) and the locations of four small windows placed symmetrically on the RV. The window material (fused silica) gives a decided glint near normal incidence. The distributed cross-section images are shown in Fig. 4-11. The total cross section curve in Fig. 4-12 shows

NOTE: DIMENSIONS IN METERS

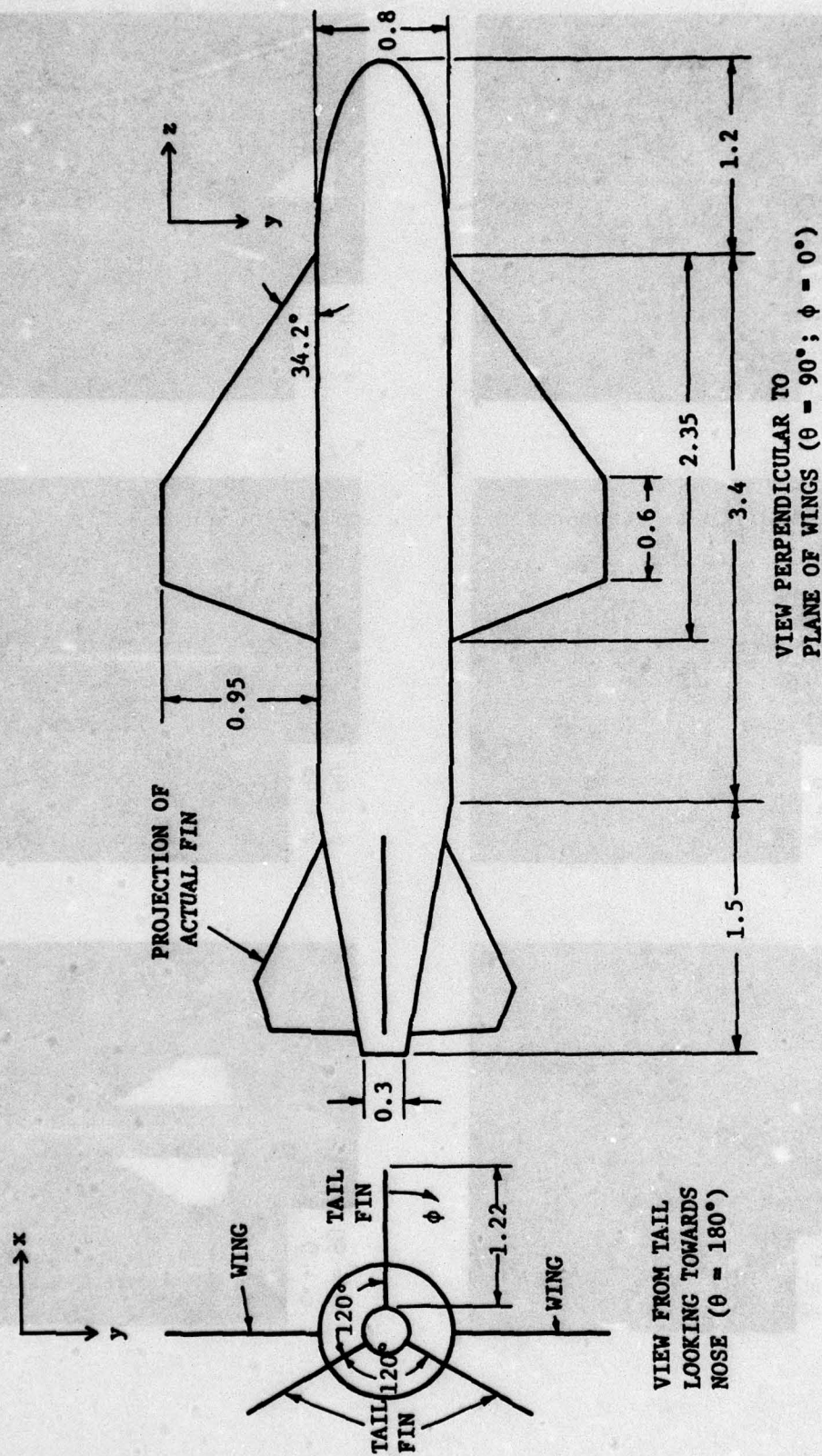


Figure 4-4. Outline Drawing of Styx Cruise Missile

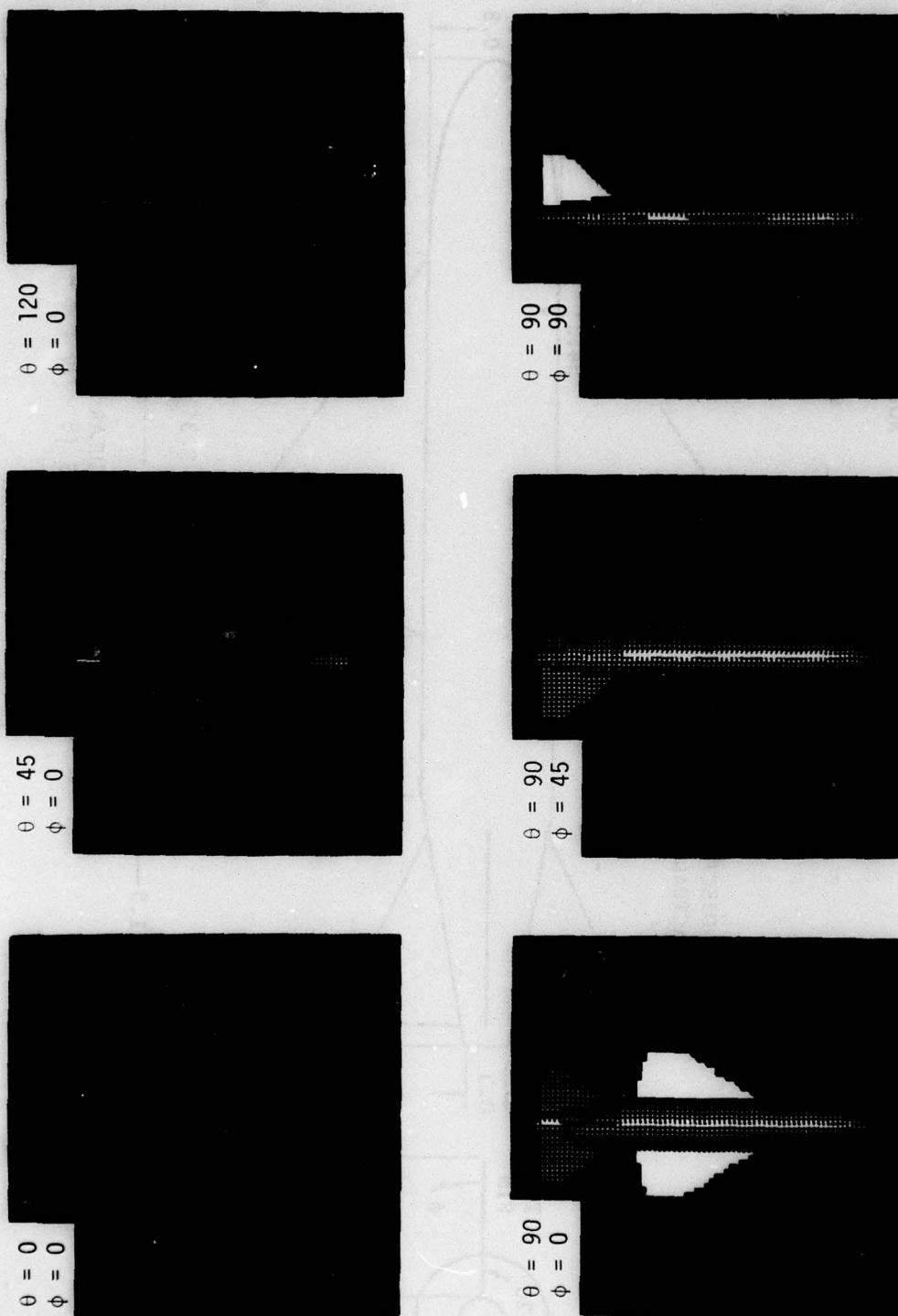


Figure 4-5. Distributed Cross Sections for the Styx Cruise Missile at Various Aspect Angles

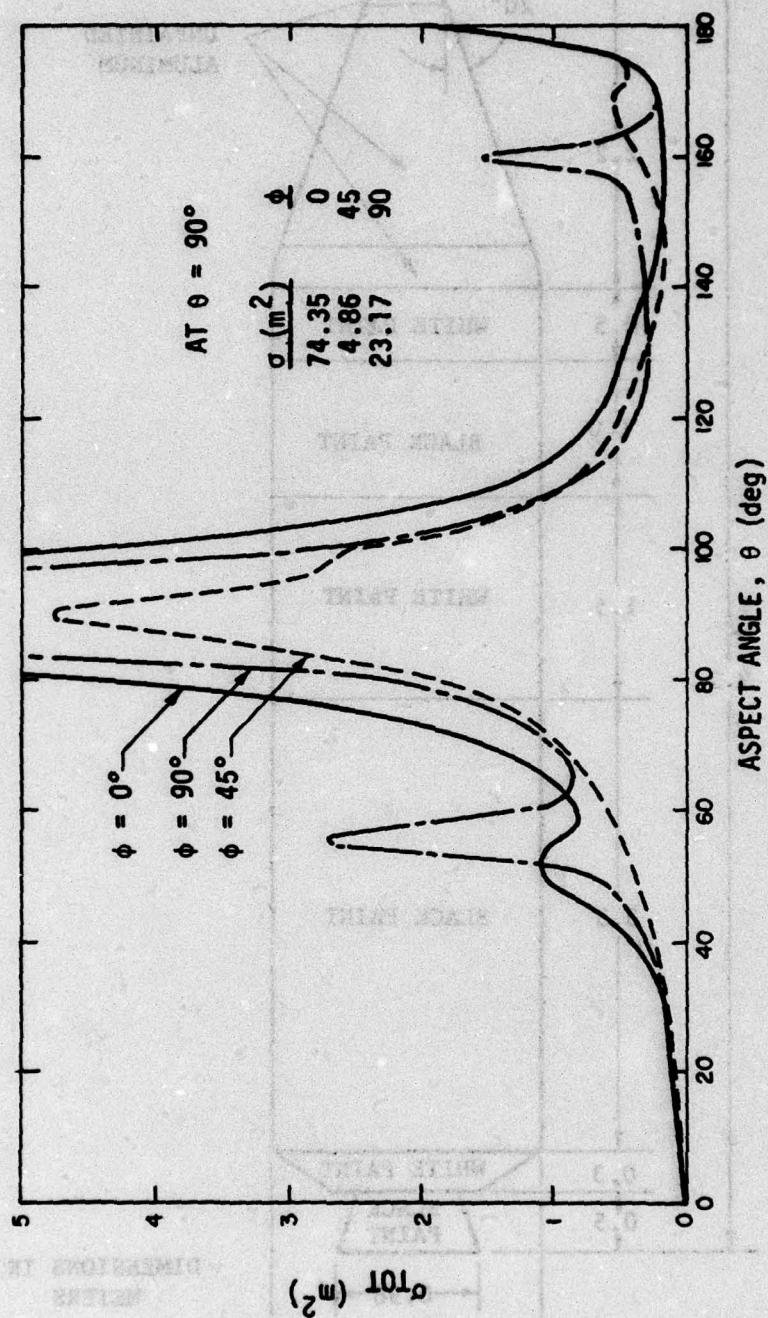


Figure 4-6. Total Cross Section vs. Aspect Angle for Styx Cruise Missile

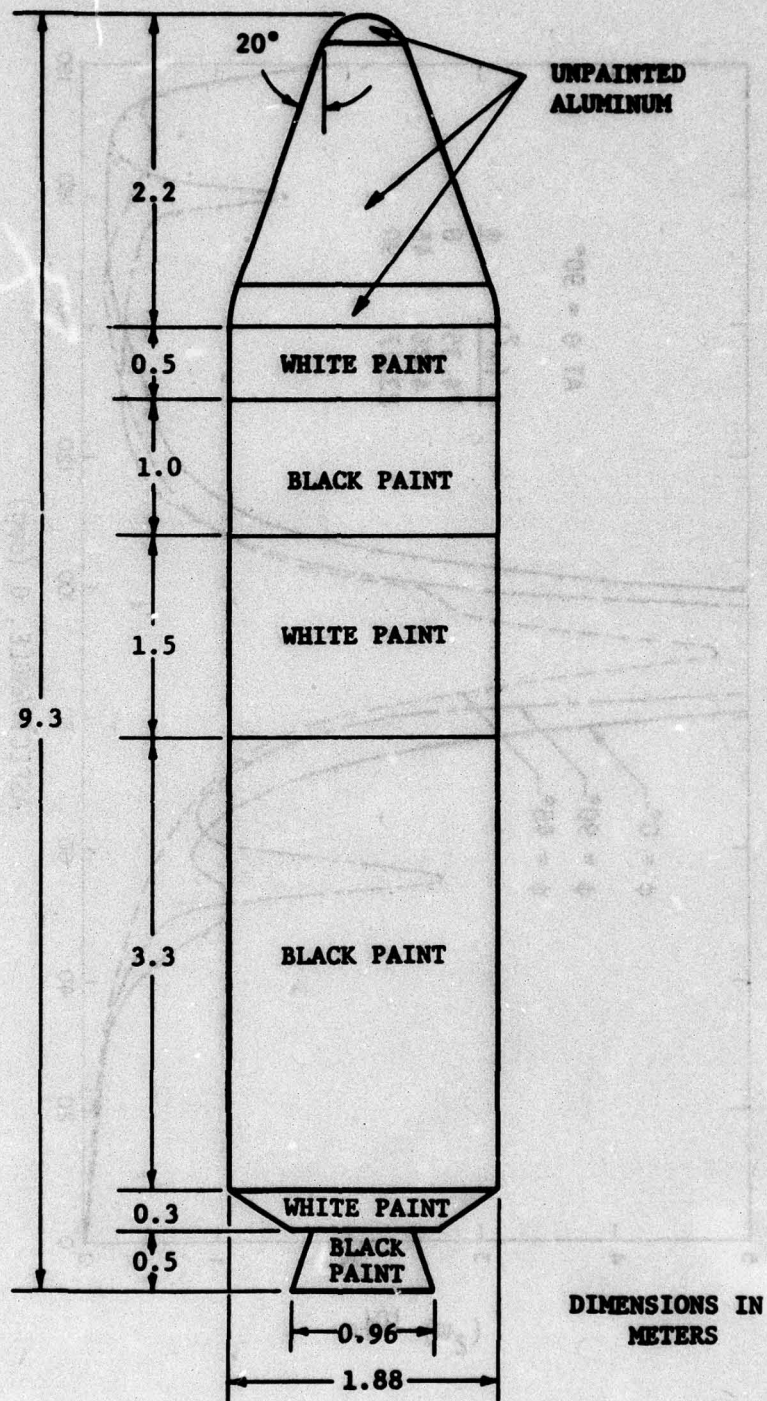


Figure 4-7. SLBM Outline Drawing

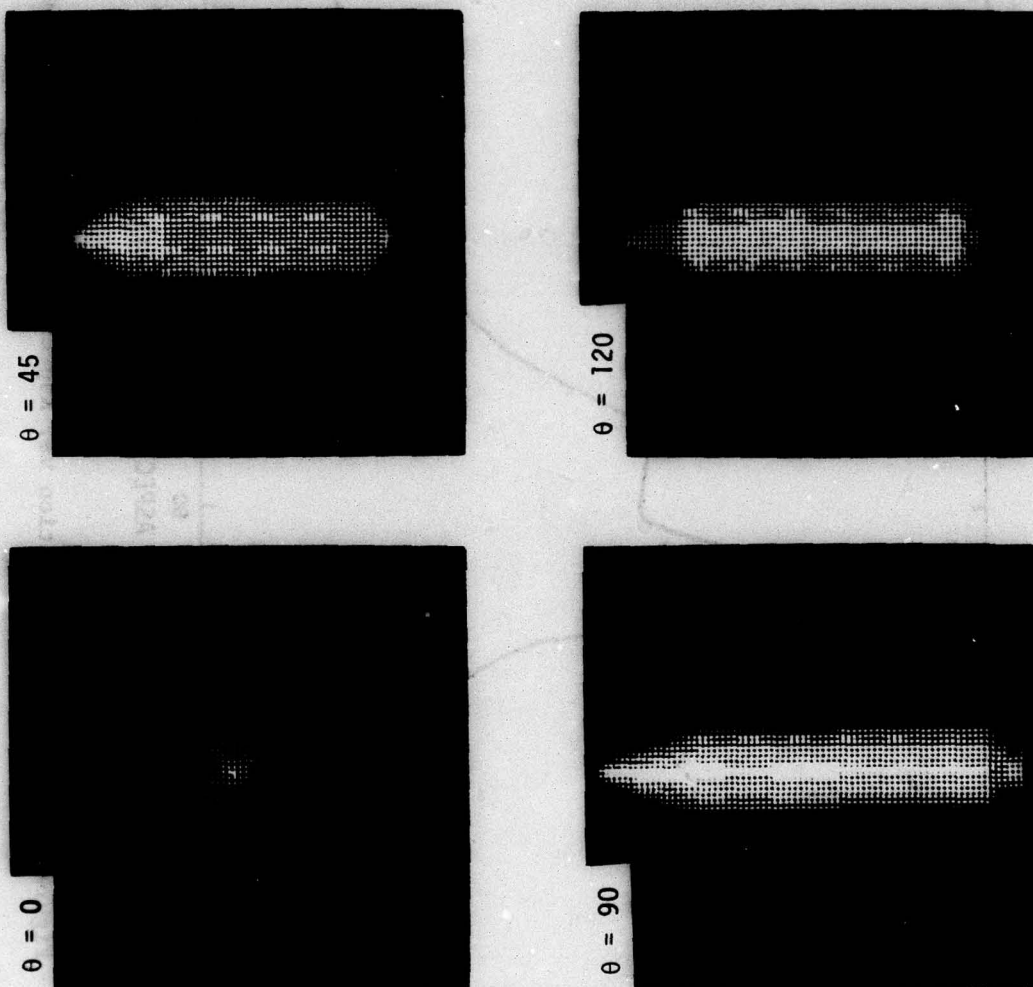


Figure 4-8. Distributed Cross Sections for an SLBM Booster at Various Aspect Angles

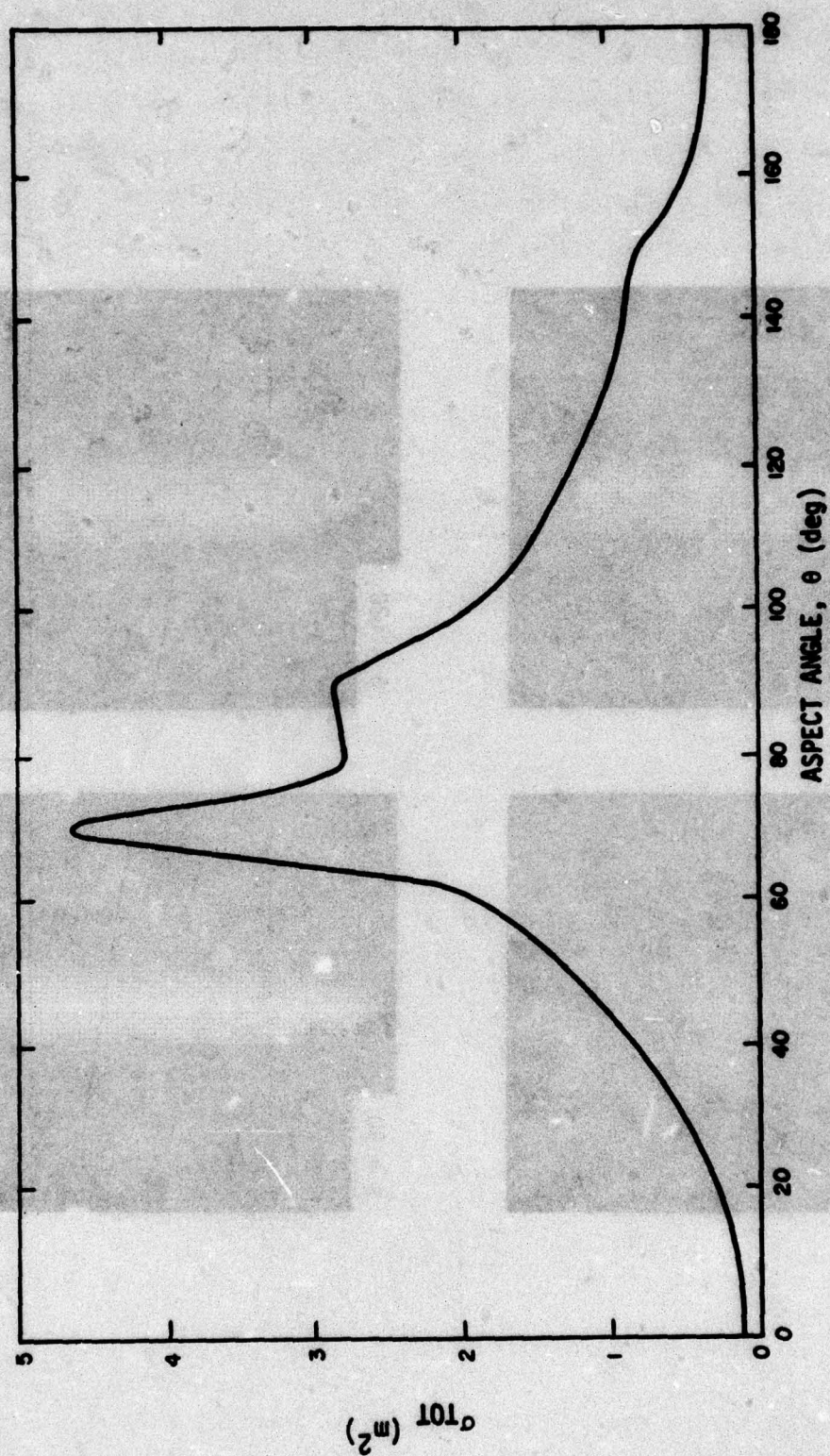


Figure 4-9. Total Cross Section vs. Aspect Angle for SLBM Booster

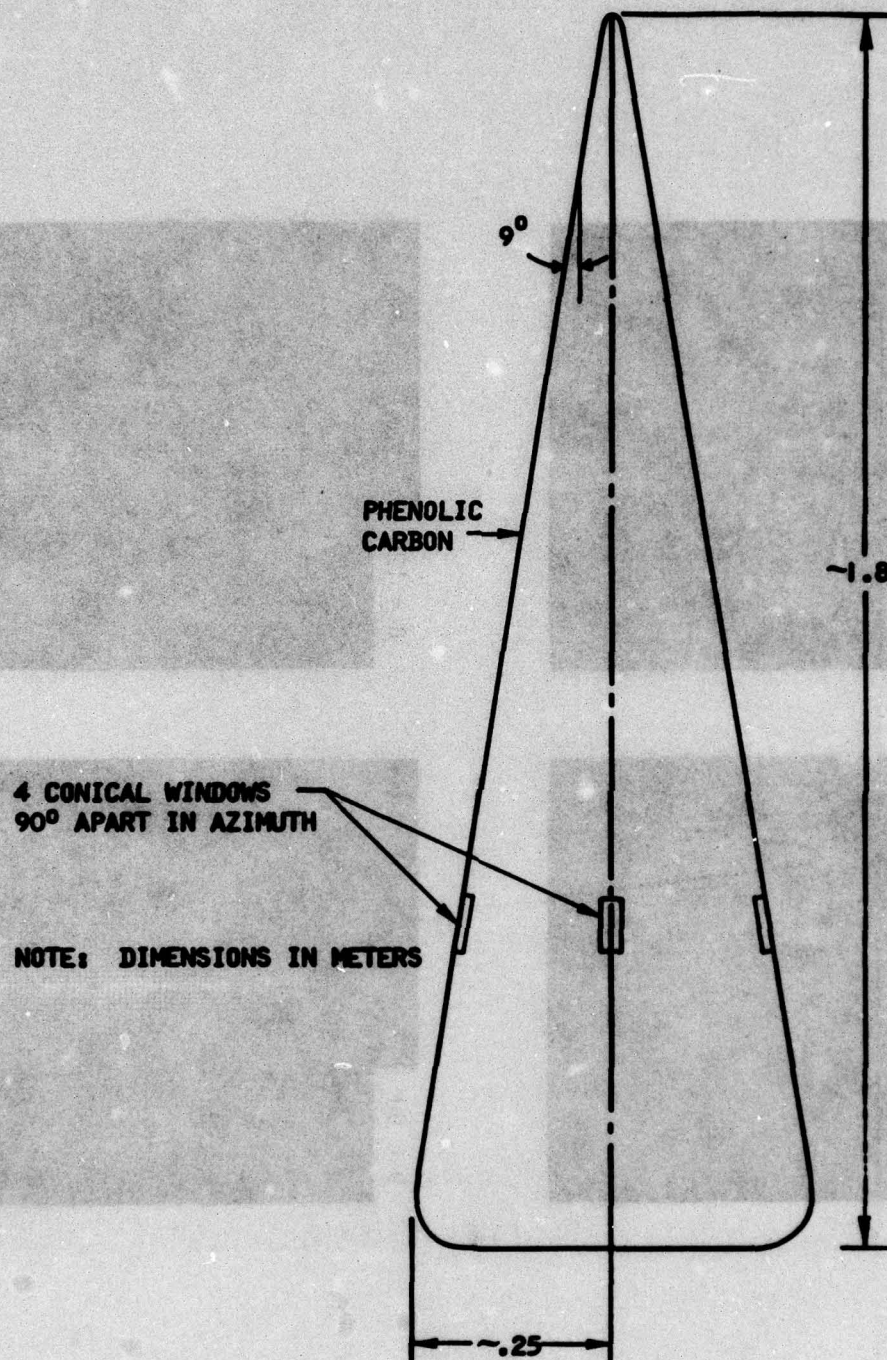


Figure 4-10. Outline Drawing of Reentry Vehicle

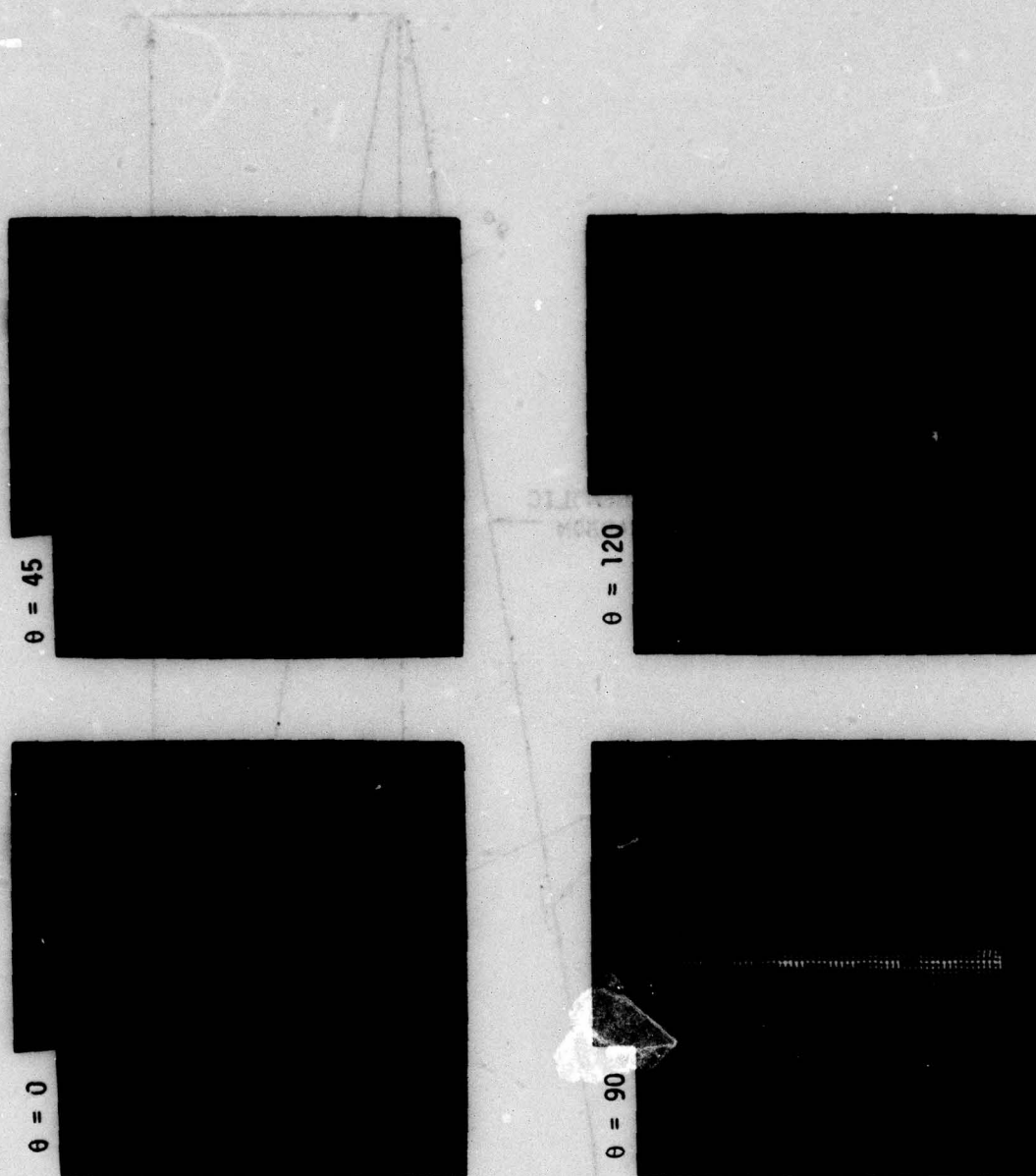


Figure 4-11. Distributed Cross Sections for a Reentry Vehicle at Various Aspect Angles

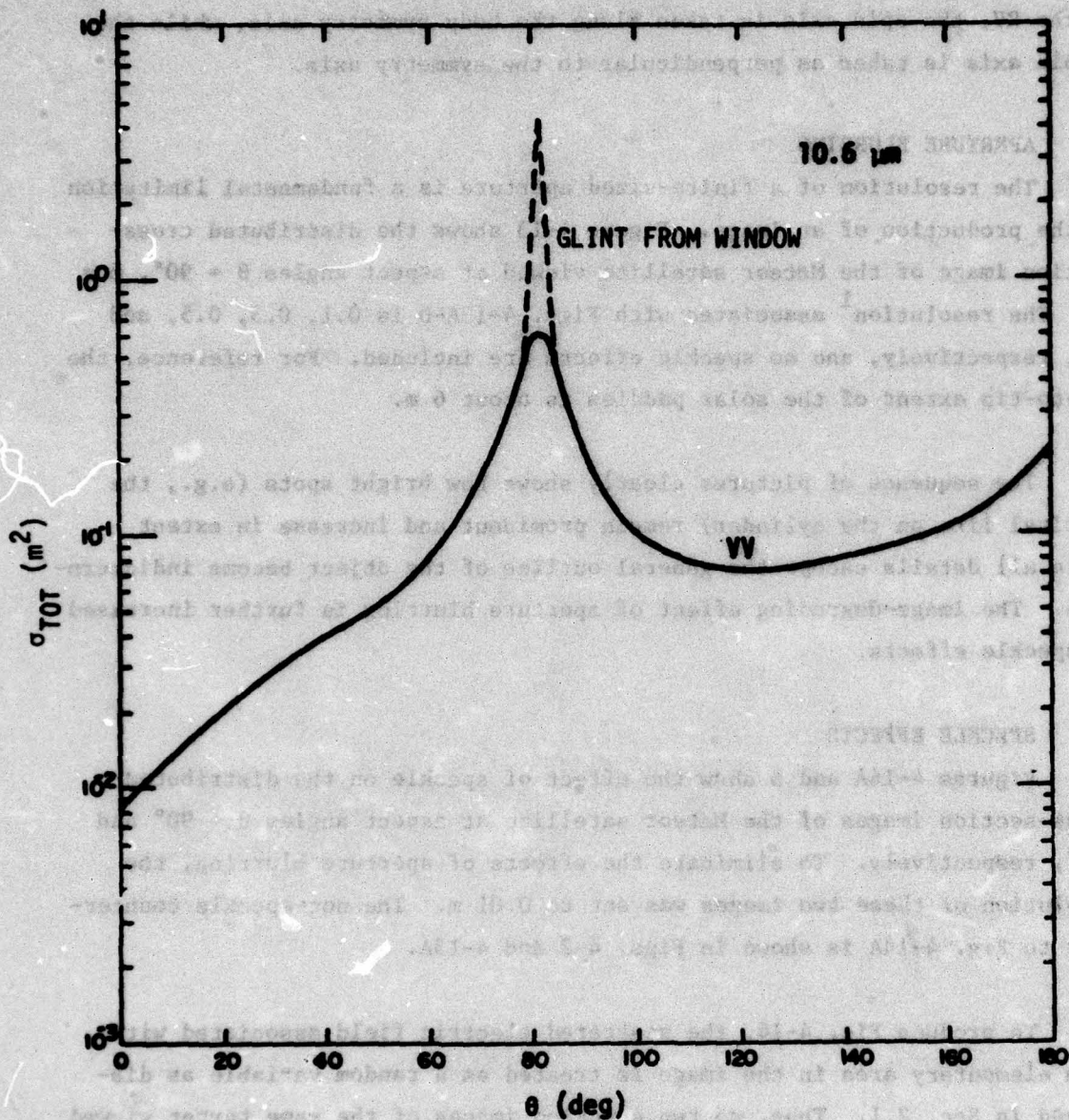


Figure 4-12. Total Cross Section vs. Aspect Angle for Reentry Vehicle

the order-of-magnitude increase at azimuths affording normal viewing to the windows. For those scenarios in Sec. 5 which include proper dynamic motion of the RV, the spin axis is taken along the body symmetry axis, while the tumble axis is taken as perpendicular to the symmetry axis.

#### 4.2 APERTURE BLURRING

The resolution of a finite-sized aperture is a fundamental limitation in the production of an image. Figure 4-13 shows the distributed cross-section image of the Meteor satellite viewed at aspect angles  $\theta = 90^\circ$ ,  $\phi = 0^\circ$ . The resolution<sup>1</sup> associated with Figs. 4-13A-D is 0.1, 0.3, 0.5, and 1 m, respectively, and no speckle effects are included. For reference, the tip-to-tip extent of the solar paddles is about 6 m.

The sequence of pictures clearly shows how bright spots (e.g., the vertical line on the cylinder) remain prominent and increase in extent while all details except the general outline of the object become indiscernible. The image-degrading effect of aperture blurring is further increased by speckle effects.

#### 4.3 SPECKLE EFFECTS

Figures 4-14A and B show the effect of speckle on the distributed cross-section images of the Meteor satellite at aspect angles  $\theta = 90^\circ$  and  $180^\circ$ , respectively. To eliminate the effects of aperture blurring, the resolution of these two images was set to 0.01 m. The non-speckle counterpart to Fig. 4-14A is shown in Figs. 4-2 and 4-13A.

To produce Fig. 4-14, the scattered electric field associated with each elementary area in the image is treated as a random variable as discussed in Sec. 2.1. Thus, no two speckled images of the same target viewed at the same aspect angles would appear exactly the same. However, if many such pictures were compared, the average value of the intensity in the elementary areas comprising the image would approach that of the corresponding areas in the non-speckled picture.

---

<sup>1</sup>Defined in Appendix A.

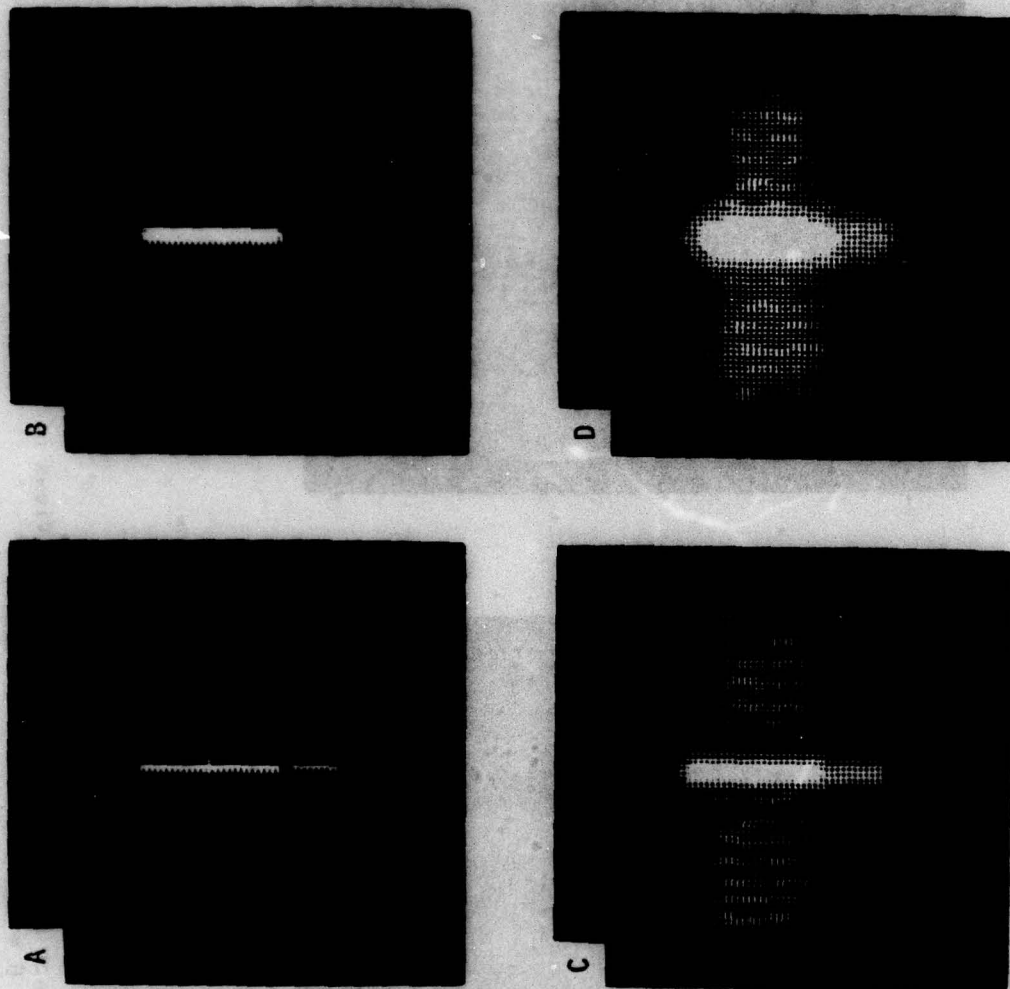
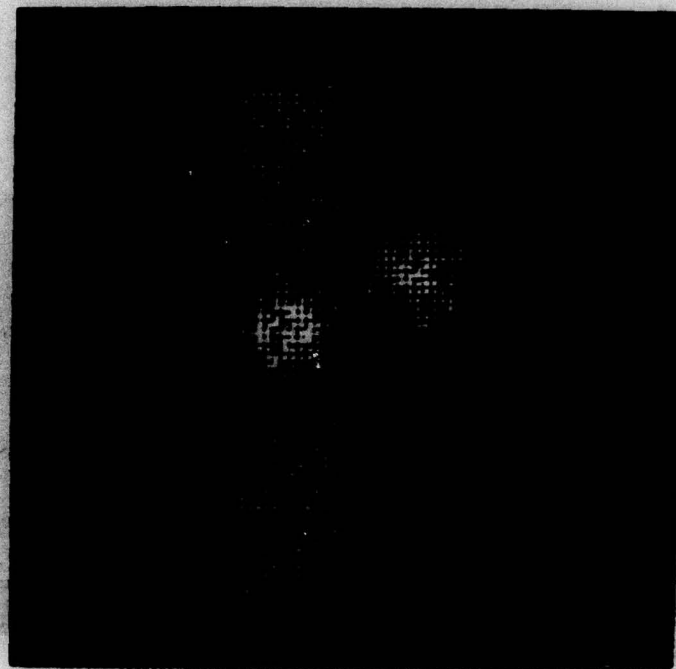


Figure 4-13. A Sequence of Meteor Spacecraft Distributed Cross Sections Which Include the Effects of Finite Resolution. The resolution at the target for the sequence is: (A) 0.1 m, (B) 0.3 m, (C) 0.5 m, (D) 1.0 m.



(B)



(A)

Figure 4-14. The Effect of Diffuse Speckle for Two Views of the Meteor Spacecraft. (A)  $\theta = 90^\circ$  and (B)  $\theta = 180^\circ$ .

An example of speckle effects on Doppler-resolved cross-section measurements is shown in Fig. 4-15. The Meteor satellite is viewed at the aspect angle  $\theta = 90^\circ$  at a rotation rate of 5 mrad/sec about the symmetry axis of the cylindrical section. The Doppler bin spacing is 190 Hz, giving a cross-range resolution at the target of about 0.2 m. The resolved Doppler cross section appears in bins number 10 through 42 inclusive.

Figures 4-15A, B, and C show three independent samples of the resolved cross section. The amplitude of the signal (cross section) appearing in each bin is treated as an exponentially distributed random variable. The average value of these random variables is shown in Fig. 4-15D which simulates the Doppler-resolved cross section in the absence of speckle effects. The central peak corresponds to the return from the cylindrical body of the spacecraft, while the flat portion of the spectrum on either side corresponds to the return from the solar cell panels. It should be noted that, for an exponential probability distribution, the standard deviation is equal to the mean. Thus, it is not surprising that the amplitudes of the bins vary widely in Figs. 4-15A, B, C.

The effects of speckle-induced fluctuations may be reduced by the non-coherent averaging of samples like those discussed above. Figures 4-16A, B, and C show the averaging of 3, 50, and 100 samples, respectively. (The three-sample average corresponds to the data shown in Figs. 4-15A, B, and C.) As above, the amplitude of the Doppler signals was treated as a random variable. However, the appropriate statistics here are those of the gamma probability distribution. Again, Fig. 4-16D shows the speckle-free cross section.

In examining a particular sequence of random variables, it should always be remembered that they are statistical quantities and can be properly interpreted only as such. As an example, note that the standard deviation of a gamma-distributed random variable is its average value divided by the square root of the number of samples averaged. The average value of the cross section in bin 26 is  $0.6 \text{ m}^2$  (Fig. 4-16D), whereas Fig.

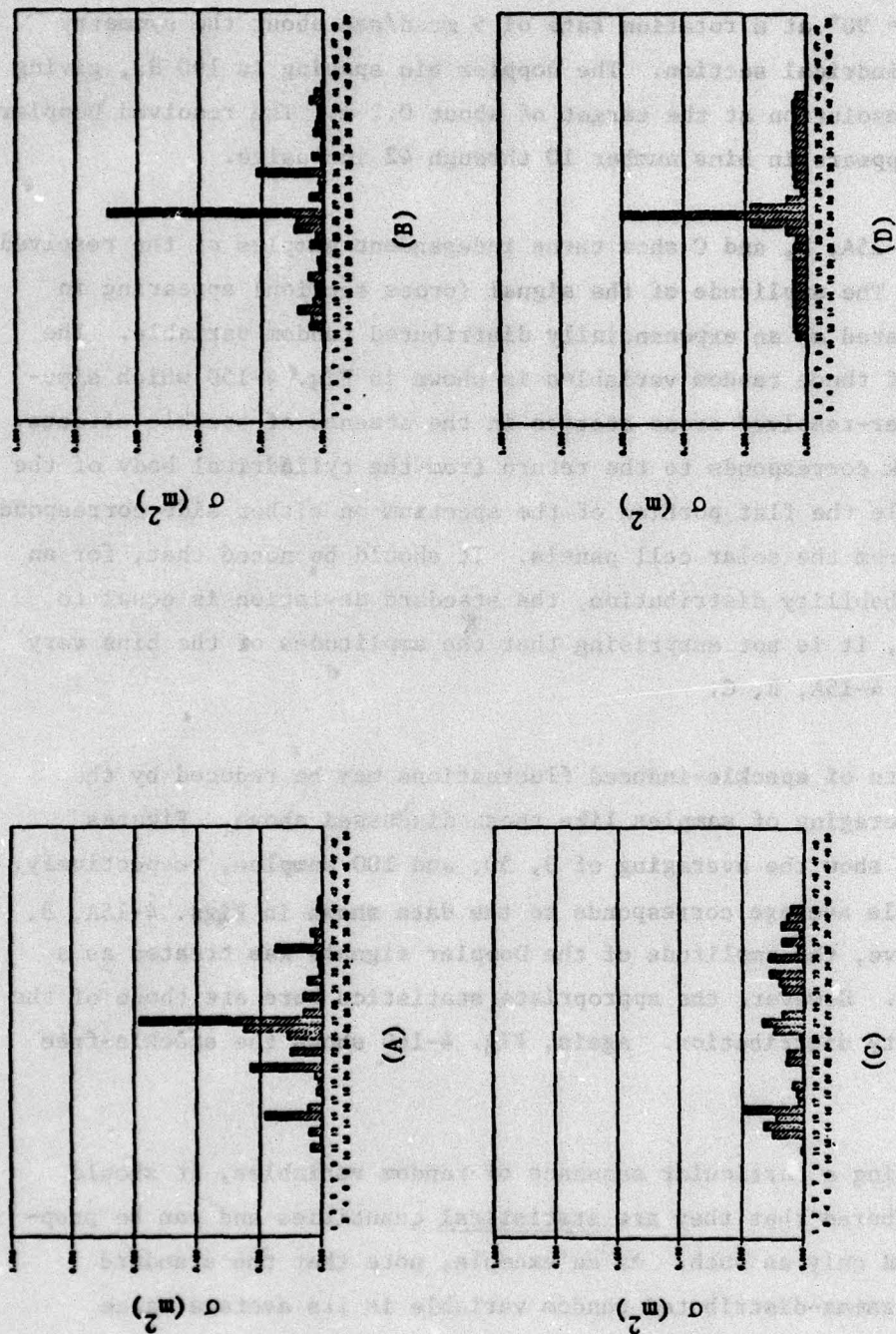


Figure 4-15. Speckle Effects on Doppler-Resolved Cross Section. A, B, C are uncorrelated samples of the Doppler spectrum (exponential statistics); D is the speckle-free spectrum.

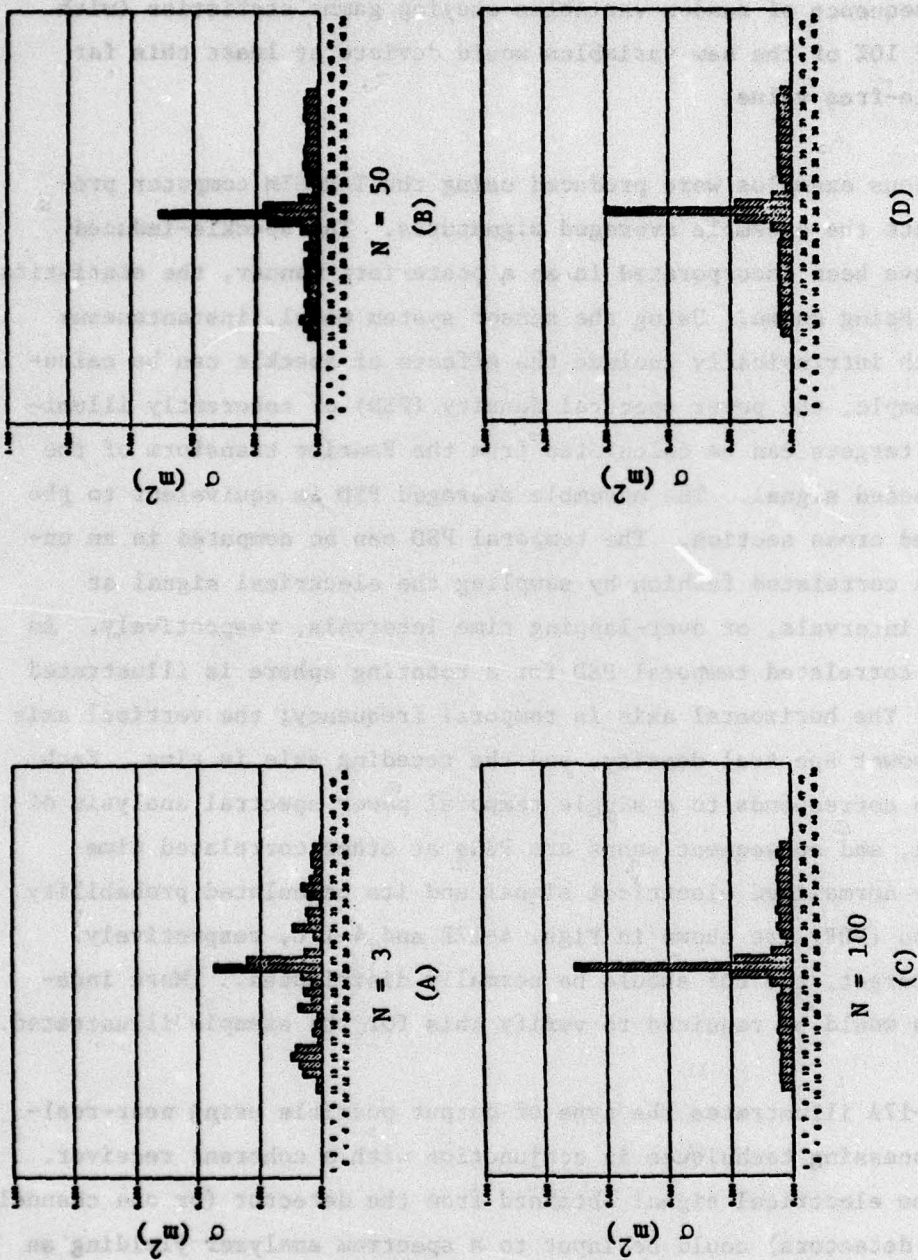


Figure 4-16. Non-Coherent Averaging of Doppler-Resolved Cross Sections. A, B, C are the averages of  $N$  uncorrelated samples of the Doppler spectrum; D is the speckle-free spectrum.

4-16C ( $N = 100$ ) shows a value of  $0.7 \text{ m}^2$  in this bin. The probability of a deviation at least this large ( $1.67\sigma$ ) is about 0.1. In other words, if different sets each containing 100 uncorrelated samples are averaged to produce a new sequence of random variables obeying gamma statistics (with  $N = 100$ ), about 10% of the new variables would deviate at least this far from the speckle-free value.

The previous examples were produced using the TARGSIM computer program to calculate the ensemble averaged signatures. The speckle-induced fluctuations have been incorporated in an a posteriori manner, the statistics of the process being known. Using the sensor system model, instantaneous signatures which intrinsically include the effects of speckle can be calculated. For example, the power spectral density (PSD) of coherently illuminated rotating targets can be calculated from the Fourier transform of the heterodyne-detected signal. The ensemble averaged PSD is equivalent to the Doppler-resolved cross section. The temporal PSD can be computed in an uncorrelated or a correlated fashion by sampling the electrical signal at separated time intervals, or over-lapping time intervals, respectively. An example of the correlated temporal PSD for a rotating sphere is illustrated in Fig. 4-17A. The horizontal axis is temporal frequency; the vertical axis is normalized power spectral density, and the receding axis is time. Each horizontal scan corresponds to a single temporal power spectral analysis of a time interval, and subsequent scans are PSDs at other correlated time intervals. The normalized electrical signal and its calculated probability density function (PDF) are shown in Figs. 4-17B and 4-17C, respectively. For a diffuse target, the PDF should be normally distributed. (More independent samples would be required to verify this for the example illustrated.)

Figure 4-17A illustrates the type of output possible using near-real-time signal-processing techniques in conjunction with a coherent receiver. For example, the electrical signal obtained from the detector (or one channel of a matrix of detectors) could be input to a spectrum analyzer yielding an output equivalent to one of the frequency traces in Fig. 4-17A. Successive time samples of the electrical signal would yield successive frequency traces.

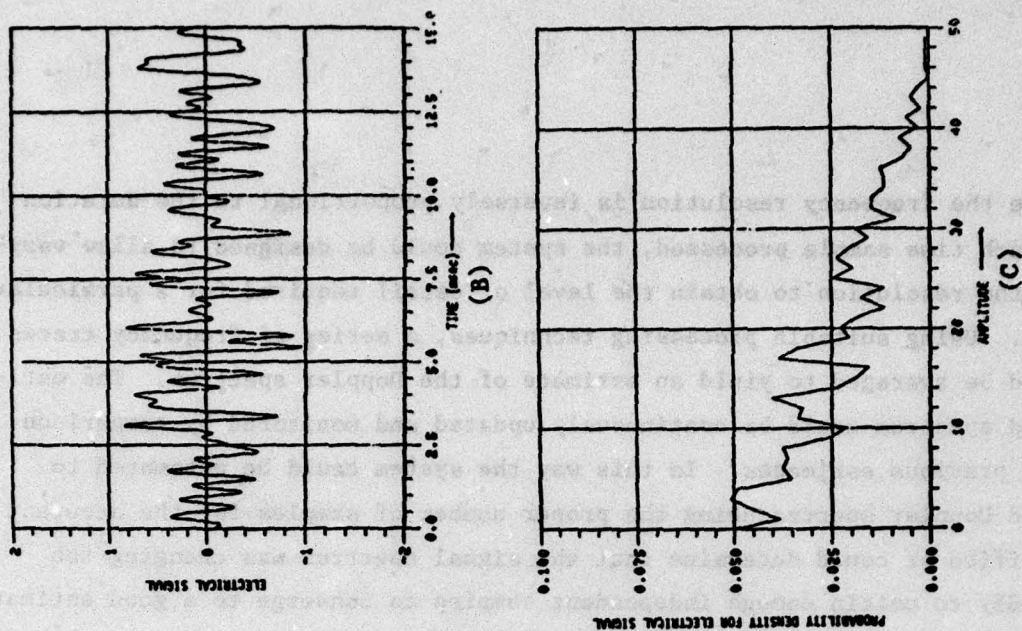


Figure 4-17. Signal Characteristics of a Rotating Sphere. The sphere is 2 m in diameter and is rotating at 0.016 rad/sec. (A) Heterodyne-detection-time-correlated temporal PSD. (B) Electrical signal. (C) Calculated PDF.

Since the frequency resolution is inversely proportional to the duration of each time sample processed, the system could be designed to allow varying the resolution to obtain the level of detail required for a particular case. Using suitable processing techniques, a series of frequency traces could be averaged to yield an estimate of the Doppler spectrum. The estimated spectrum could be continuously updated and monitored by comparison with previous estimates. In this way the system could be automated to yield Doppler spectra using the proper number of samples for the accuracy specified or could determine that the signal spectrum was changing too rapidly to obtain enough independent samples to converge to a good estimate of the true ensemble average.

#### 4.4 COMBINED SPECKLE AND APERTURE-BLURRING EFFECTS

Figure 4-18 shows a sequence of six distributed cross-section images including both speckle and finite aperture effects of a Meteor satellite at aspect angle  $\theta = 90^\circ$ ,  $\phi = 0^\circ$ . As before, the tip-to-tip solar paddle extent is about 6 m, while the overall image width is 8 m.

Table 4-1 gives the resolution associated with each of the images in Fig. 4-18. The table also gives corresponding sample values of aperture diameter and target-sensor range. For the scenarios considered in Sec. 5, typical ranges are from 250 to 1000 km. Thus "conventional" angle-angle imaging (as distinguished from range-Doppler imagery) of targets of interest is not practical for viewing through 1 m optics at  $\lambda = 10.6 \mu\text{m}$ .

#### 4.5 DAMAGE ASSESSMENT EFFECTS

To illustrate the possibilities and difficulties of using a laser to perform damage assessment, a simulated "burn spot" was added to the Meteor satellite and to the RV. Figure 4-19 shows an image of the satellite at aspect angle  $\theta = 65^\circ$  ( $5^\circ$  from normal viewing). The damaged area was simulated by a small disc (diameter 0.6 m) centered on one of the four planes comprising one of the solar paddles. The disc was coated with black paint to provide some contrast with the solar paddle material.

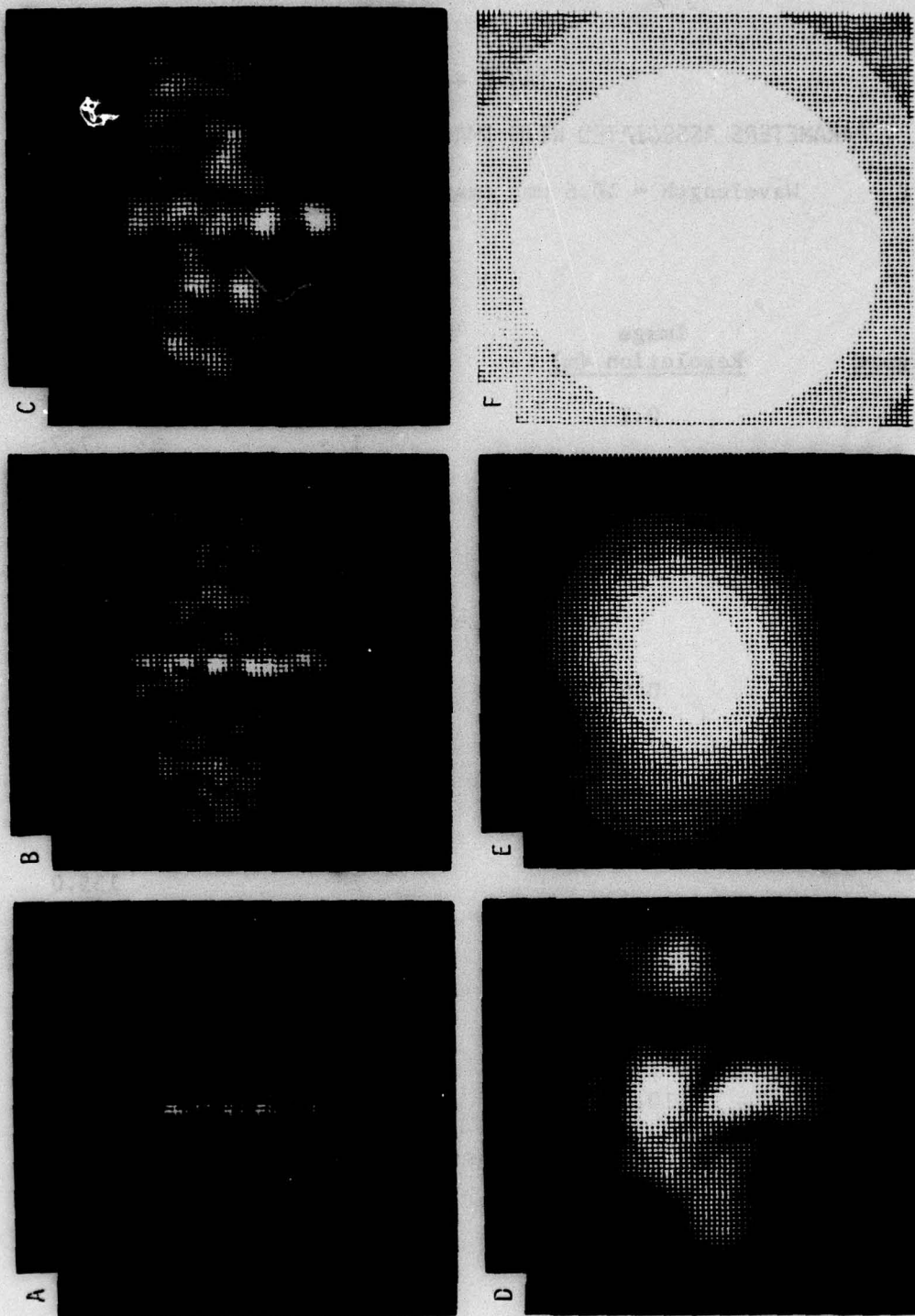


Figure 4-18. A Sequence of Distributed Cross Sections of a Meteor Spacecraft Which Include the Effects of Finite Resolution and Diffuse Speckle

TABLE 4-1

## PARAMETERS ASSOCIATED WITH IMAGES SHOWN IN FIGURE 4-18

Wavelength = 10.6  $\mu\text{m}$ ; Image Scale Width = 8 m

<u>Figure</u>	<u>Image Resolution (m)</u>	<u>Sample Aperture Diameter (m)</u>	<u>Associated Target Range (Km)</u>
A	0.1	0.5	3.9
		1	7.7
		2	15.5
		5	38.7
B	0.3	0.5	11.6
		1	23.2
		2	46.4
		5	116.0
C	0.5	0.5	19.3
		1	38.7
		2	77.3
		5	193.0
D	1.0	0.5	38.7
		1	77.3
		2	155.0
		5	387.0
E	3.0	0.5	116.0
		1	232.0
		2	464.0
		5	1160.0
F	10.0	0.5	387.0
		1	773.0
		2	1547.0
		5	3866.0

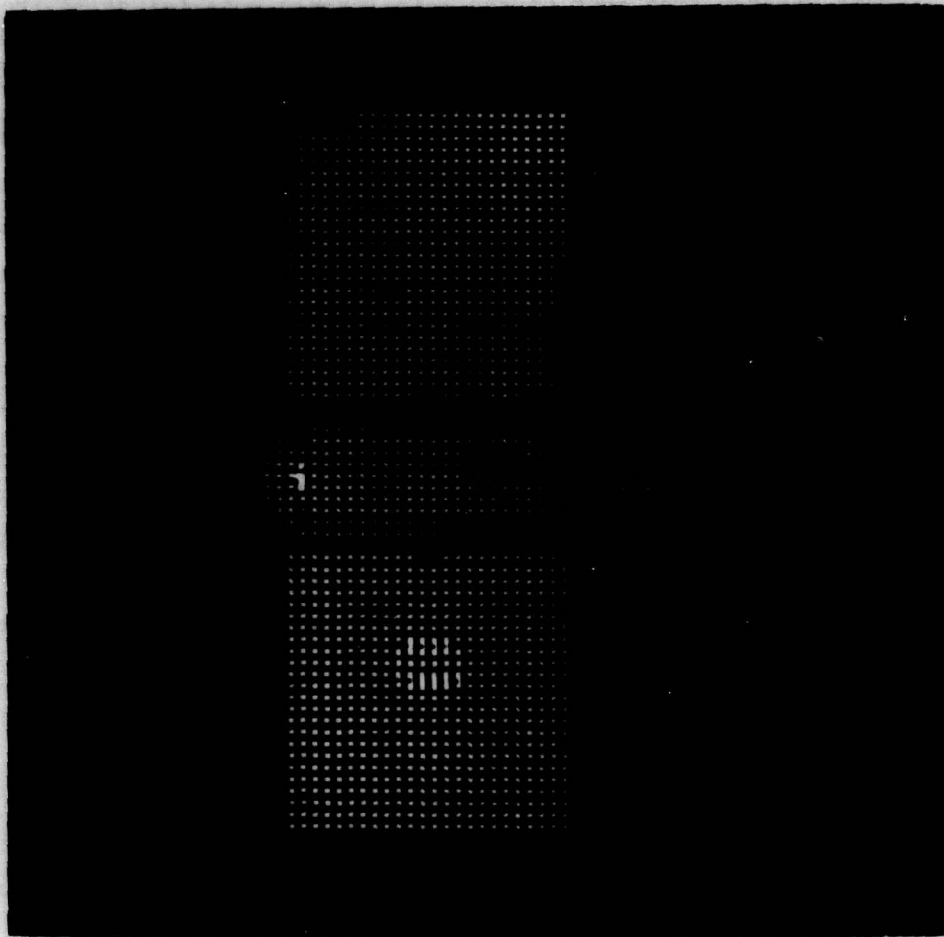


Figure 4-19. Distributed Cross Section of Meteor Satellite at  $\theta = 65^\circ$  Showing Burned Area

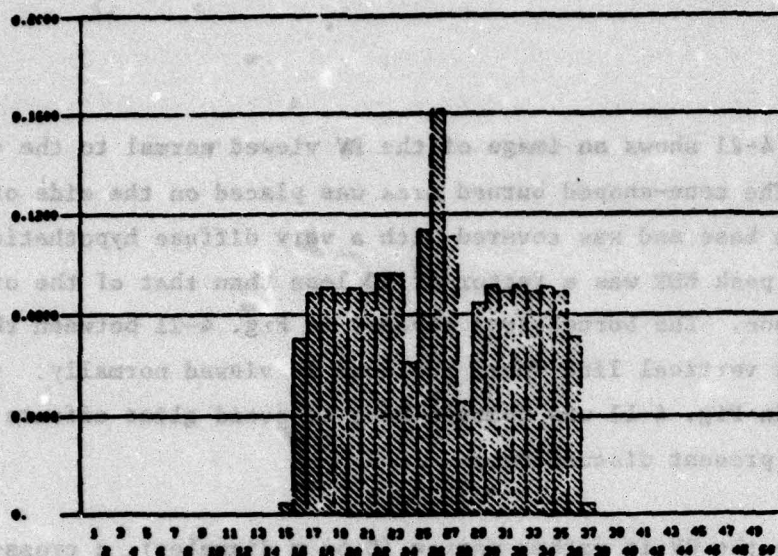
Figure 4-20 shows the effect of the burn spot on the Doppler-resolved cross section by comparing the average Doppler cross section of the usual Meteor satellite (Fig. 4-20A) with that of the altered version (Fig. 4-20B). The satellites were spinning about the cylinder axis. The cross-range resolution was set to 0.3 m, so that the burn spot should affect two or three Doppler bins. In fact, the additional cross section contributed by the spot appears in bins 31 and 32. (The cross section increased because the BDR of black paint is greater than that of the solar paddle material at 5° from the surface normal.)

The observed increase in resolved cross section in bin 31 is from  $0.0887 \text{ m}^2$  to  $0.1007 \text{ m}^2$  in Fig. 4-20B. This gives a contrast ratio of 1.135. As shown in Sec. 4.3, the effect of speckle is to randomize the contribution to each Doppler bin about the average values shown in Fig. 4-20. If only one sample of the Doppler-resolved cross sections is obtained, it can be shown<sup>1</sup> that for exponentially distributed random variables the probability of detecting such a small contrast ratio is 0.53. That is, by examining single sample resolved cross-section measurements of the normal and burned satellites, the chance of correctly determining which satellite has been damaged can just as well be simulated by flipping a coin. For this small a contrast ratio, even averaging many measurements may not be of great help. Some 200 to 300 samples would have to be averaged before a probability approaching 0.9 of reliably discerning the above contrast ratio would be attained.

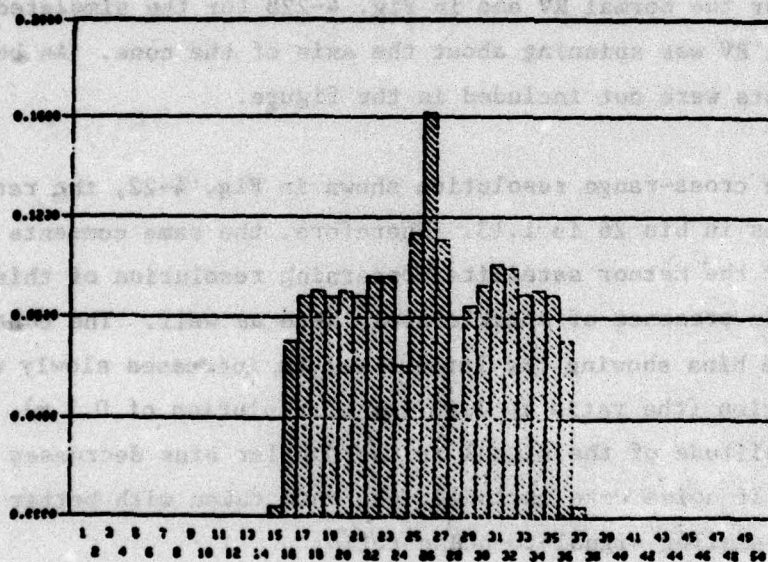
For the materials used here to simulate the burned area, it was observed that the normal vs. burned target Doppler cross-section comparisons retained the general character shown in Fig. 4-20 for 20° to 40° in aspect angle away from the surface normal. In an actual scenario, this leeway in data taking could allow extra time for accumulating the needed measurements to assess the damage.

---

<sup>1</sup>J. Wilson, A Theoretical Evaluation of Laser Range-Doppler Imaging Radar Performance, General Research Corporation, Report 506W-06-TR, December 1974.



(A)



(B)

Figure 4-20. Doppler Resolved Cross Section of Meteor (A) Without burned area, (B) With burned area. Note that burned area appears in bins 31 and 32.

Figure 4-21 shows an image of the RV viewed normal to the cone ( $\theta = 81^\circ$ ). The cone-shaped burned area was placed on the side of the cone near the base and was covered with a very diffuse hypothetical material whose peak BDR was a factor of 10 less than that of the original phenolic carbon. The burned area appears in Fig. 4-21 between the break in the bright vertical line where the cone is viewed normally. (The window seen in Fig. 4-11 was removed here to avoid glint effects extraneous to the present discussion.)

Because the RV is rather narrow (0.54 m diameter), a cross-range (Doppler) resolution of 0.3 m as used for the satellite places the entire target within 3 bins. To improve the display of Doppler-resolved cross section, the resolution was changed to 0.05 m. The results are shown in Fig. 4-22A for the normal RV and in Fig. 4-22B for the simulated burn effects. The RV was spinning about the axis of the cone. As before, speckle effects were not included in the figure.

For the cross-range resolution shown in Fig. 4-22, the ratio of the amplitudes in bin 26 is 1.13. Therefore, the same comments which were made for the Meteor satellite concerning resolution of this small a ratio in the presence of speckle apply here as well. The contrast ratio for the bins showing the largest return increases slowly with finer resolution (the ratio is 1.08 for a resolution of 0.3 m). However, the amplitude of the signal in the Doppler bins decreases with finer resolution. If noise were included, the data taken with better resolution would have a smaller signal-to-noise ratio.

#### 4.6 NOISE EFFECTS

The effect of receiver noise on the target signal is discussed in Appendix B, where the addition of shot noise is analyzed for a heterodyne detection system. Results of the simulation are shown in Figs. 4-23B to F,

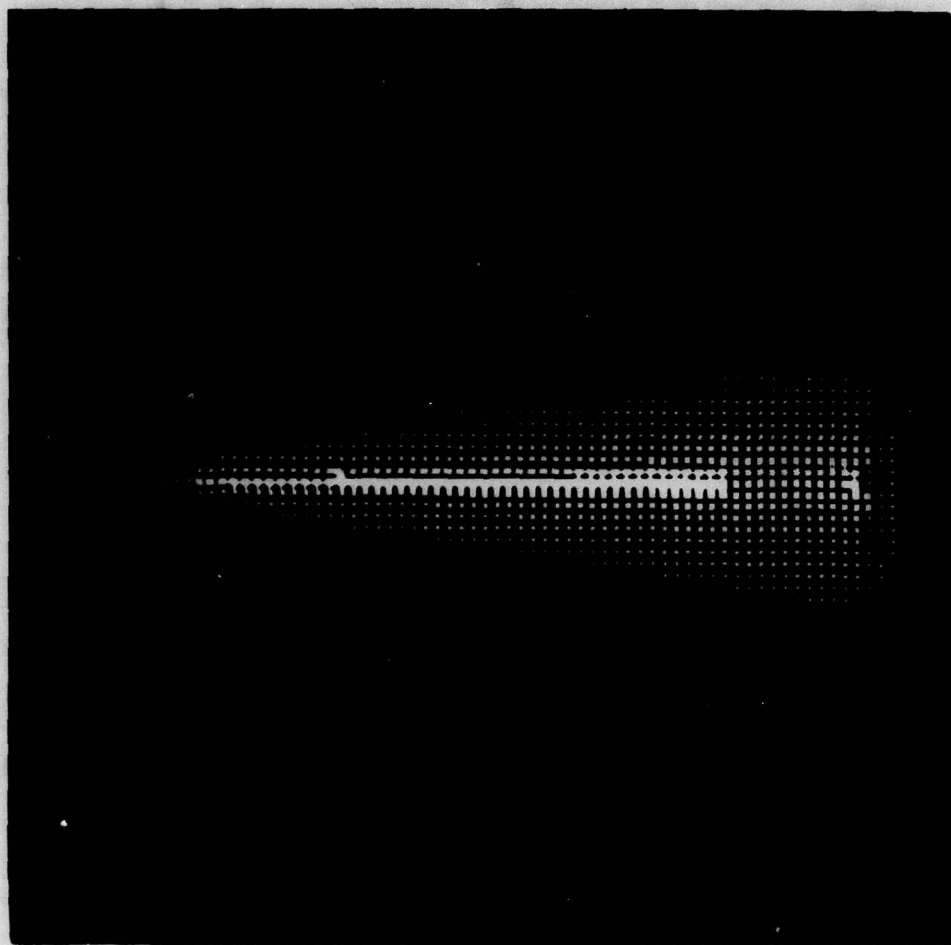
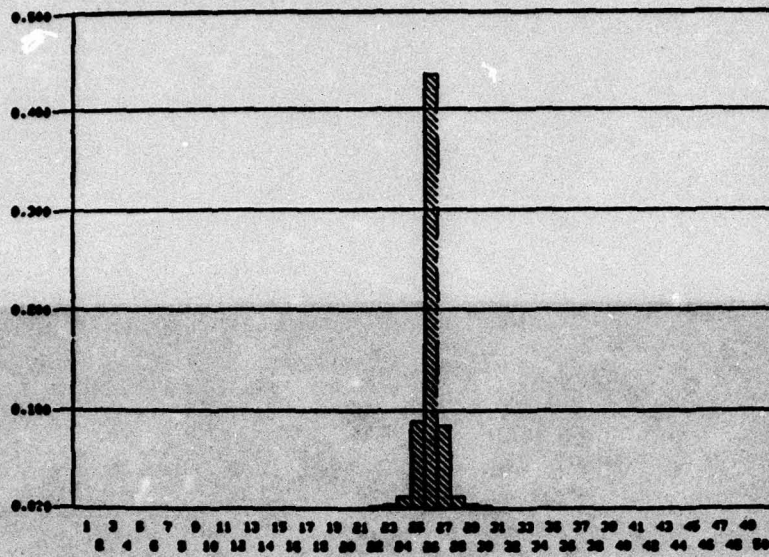
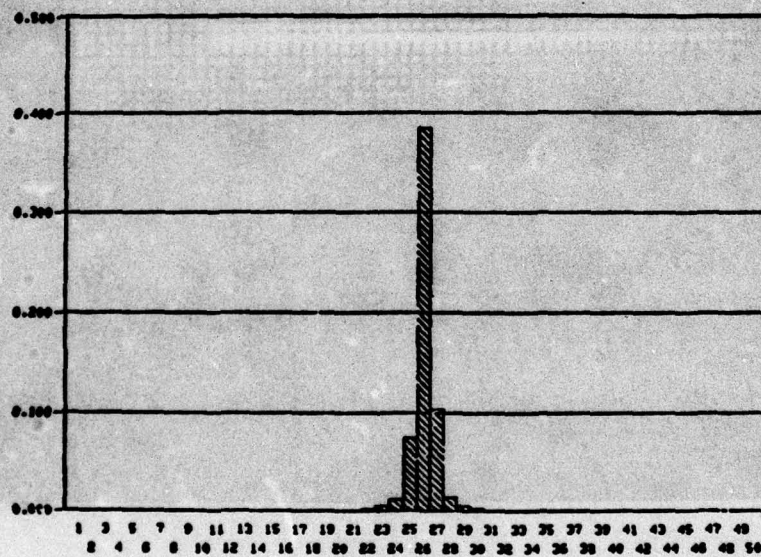


Figure 4-21. Distributed Cross Section of RV at  $\theta = 90^\circ$  Showing Burned Area



(A)



(B)

Figure 4-22. Doppler-Resolved Cross Section of RV. (A) Without burned area. (B) With burned area.

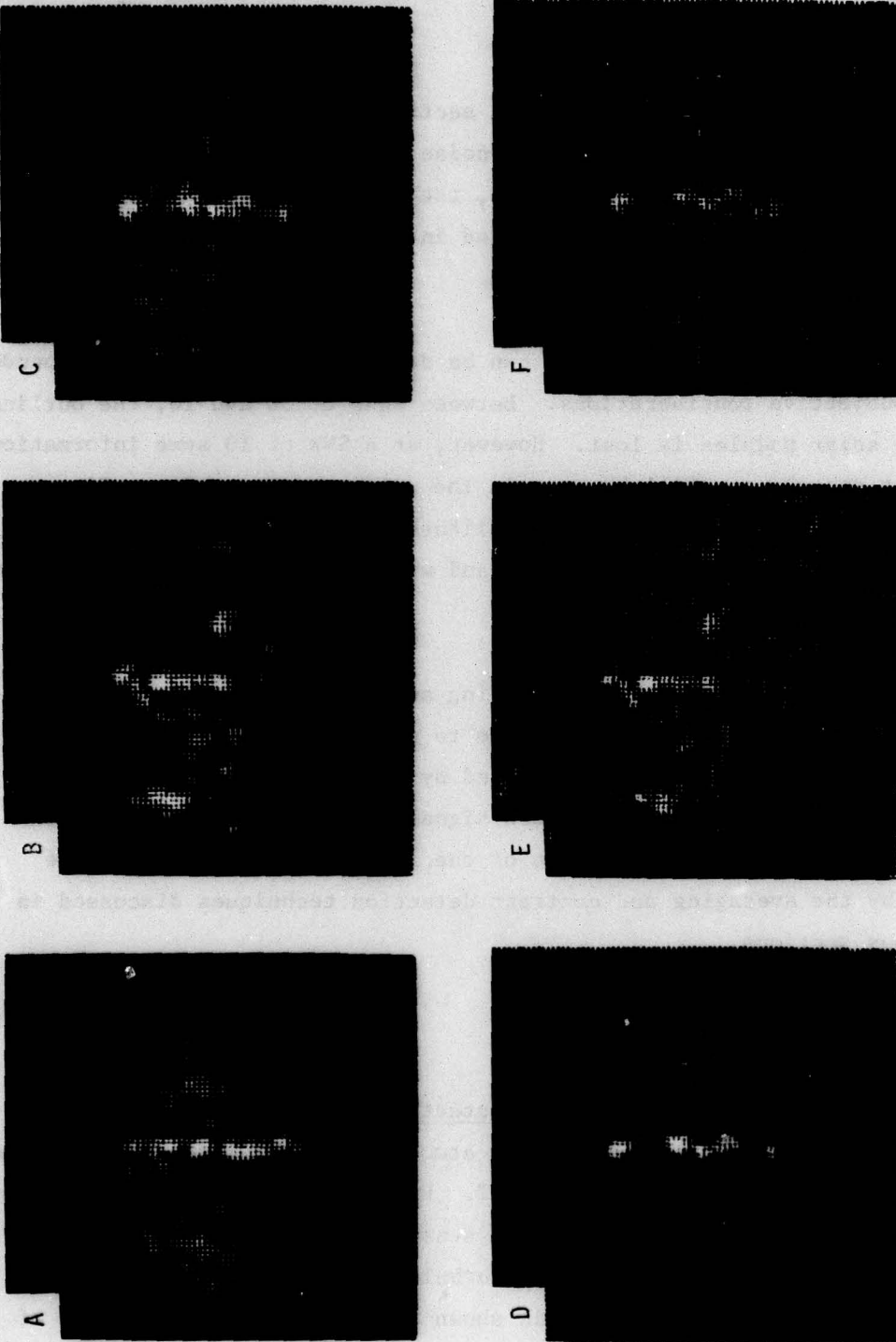


Figure 4-23. Sequence Illustrating the Effect of Finite SNR on Distributed Cross Sections of the Meteor. The SNRs are:  $\infty$ , 100, 50, 30, 10, 5 for A-F, respectively.

which display the distributed cross section of the Meteor satellite at aspect angle  $\theta = 90^\circ$  for signal-to-noise ratios (SNR) of 100, 50, 30, 10, and 5, respectively. For reference, the noise-free image previously illustrated in Fig. 4-18A is repeated in Fig. 4-23A. The resolution associated with Fig. 4-23 is 0.3 m.

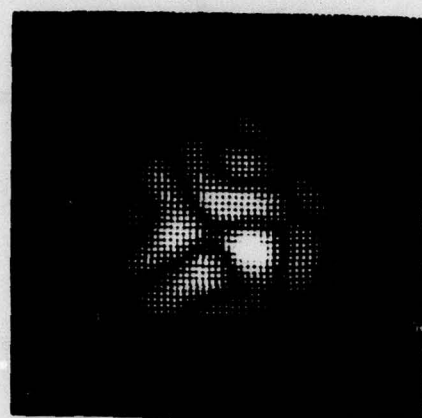
Whether or not the target can be detected in the noise is dependent upon subjective considerations. Between SNRs of 30 and 10, the outline of the solar paddles is lost. However, at a SNR of 10 some information (bright spots) can still be seen in the solar paddle region. Since at this aspect angle the paddles are diffuse reflectors, any such bright spots are statistical fluctuations and will vary in exact location from image to image.

The more glinty return appearing as a vertical line along the cylindrical section is obviously due to normal viewing of that surface. Although the line is somewhat blurred by finite resolution and broken up by speckle effects, some return signal can be seen even with a SNR of 5. Of course, the extraction of the image from the noise can be aided by the averaging and contrast detection techniques discussed in the previous sections.

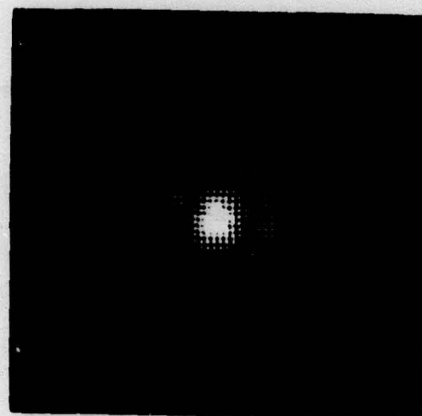
#### 4.7 ATMOSPHERIC EFFECTS

##### 4.7.1 Turbulence Effects on Image Detection

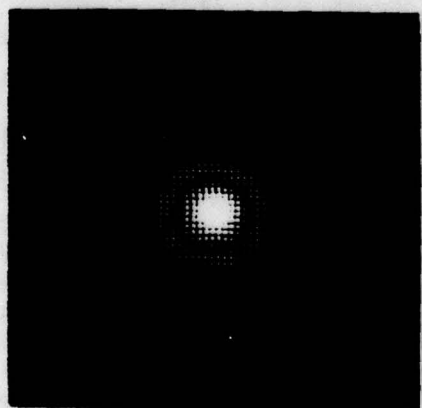
The modeling of the effect of atmospheric turbulence on laser beam propagation is discussed in Sec. 2.2. Examples of exercising the turbulence model in conjunction with the sensor system model are shown in Figs. 4-24 through 4-27. The effect of turbulence on the far-field diffraction pattern of a circular aperture is shown in Fig. 4-24. The top row of images (Fig. 4-24A-C) compares the diffraction with no turbulence to the diffraction patterns with increasing levels of turbulence for a constant



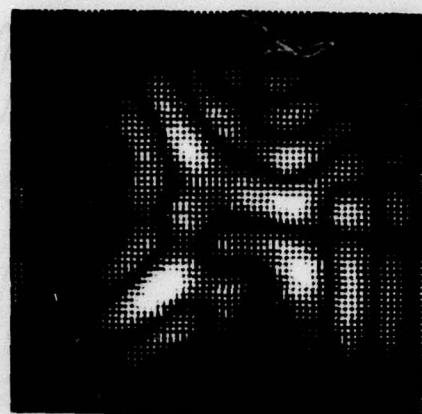
(C)  $\sigma_n = 2.4, L_0 = 10$



(B)  $\sigma_n = 0.75, L_0 = 10$



(A)  $\sigma_n = 0$



(F)  $\sigma_n = 6.0, L_0 = 20$



(E)  $\sigma_n = 3.4, L_0 = 10$



(D)  $\sigma_n = 1.9, L_0 = 5$

Figure 4-24. A Sequence of 3 dB/Level Gray-Scale Images of the Far-Field Diffraction Pattern of a Circular Aperture for Various Turbulence Levels

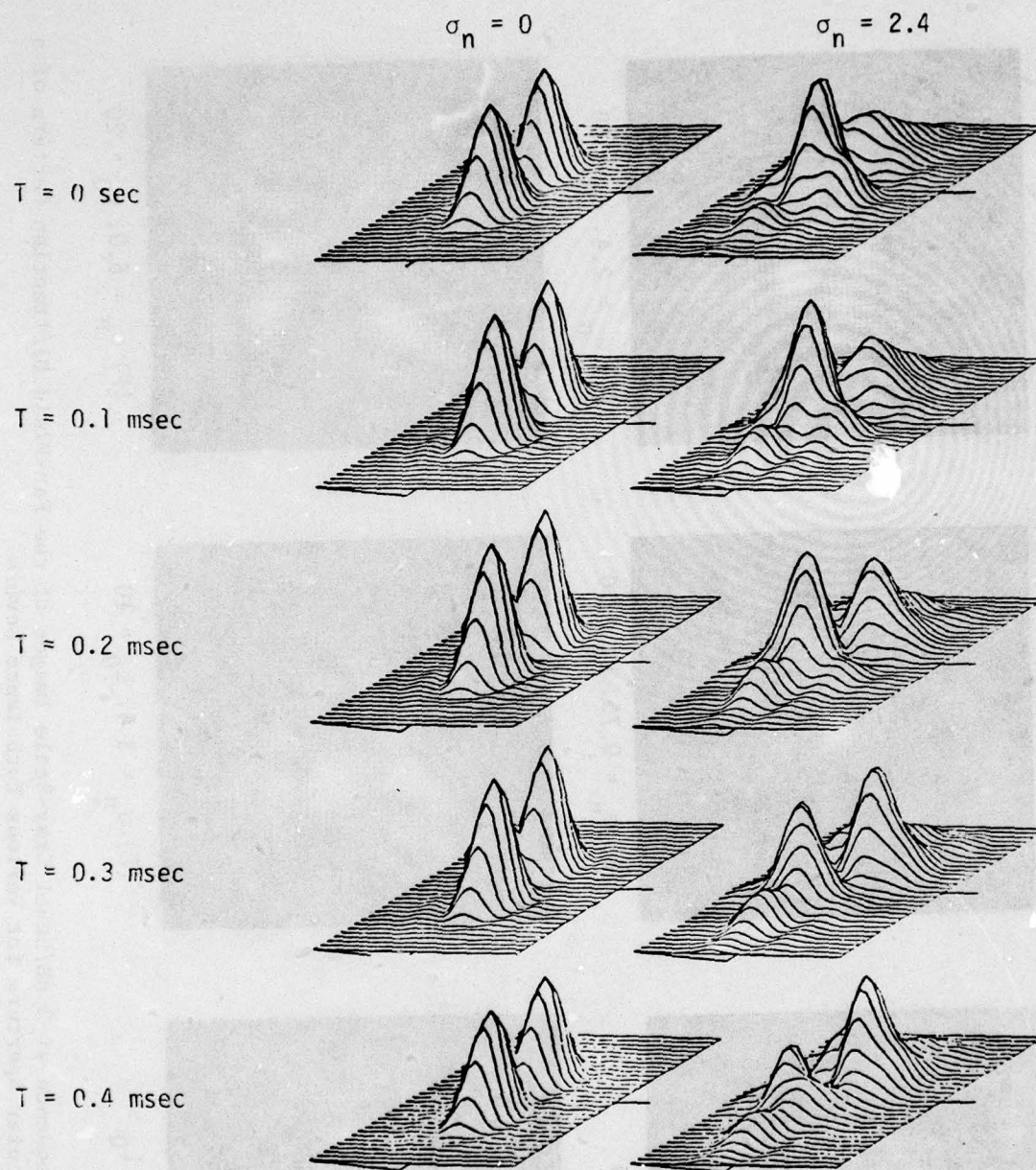


Figure 4-25. Intensity Contour Maps of the Resolved Image of a Uniformly Illuminated Two-Point Target.  $D = 4$  m. Viewed through a 0.65-m circular aperture at a range of 150 km using 10.6- $\mu$ m radiation. A static atmosphere with no absorption was assumed. The changes occurring with time are a result of the target's 1.65 mrad/sec rotation rate.  $\sigma_n$  = RMS phase variation of the atmosphere.

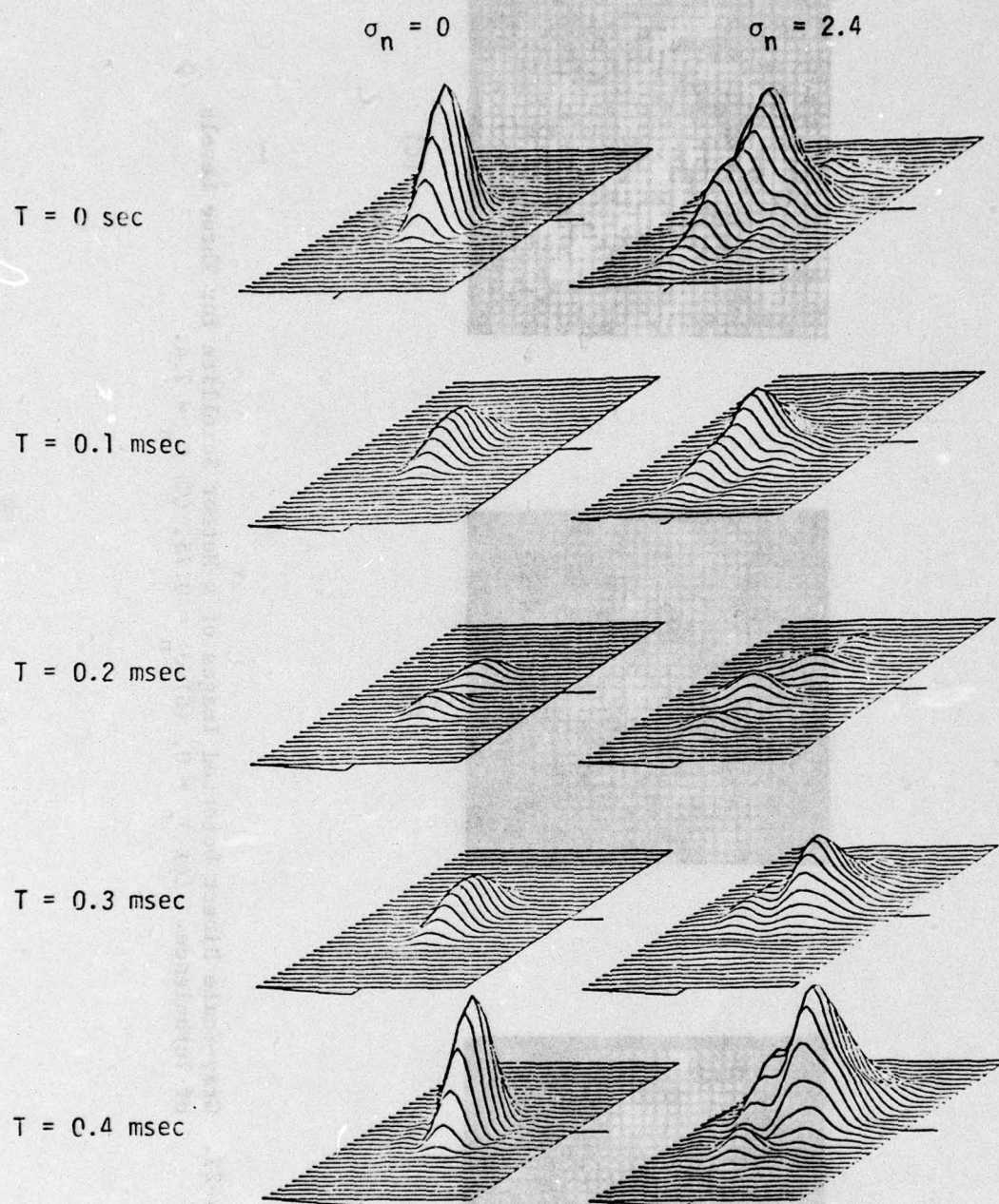
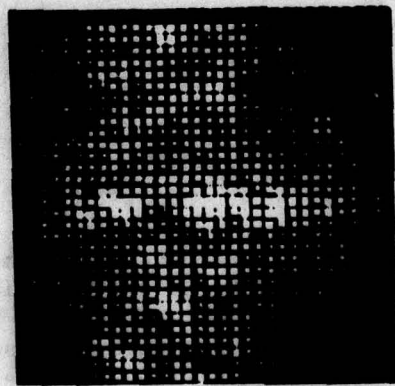
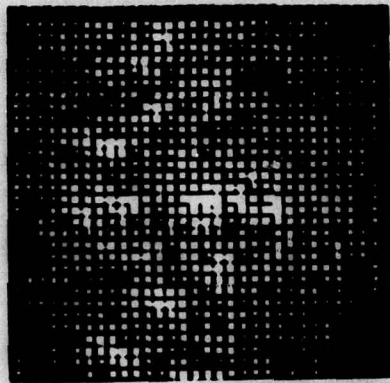


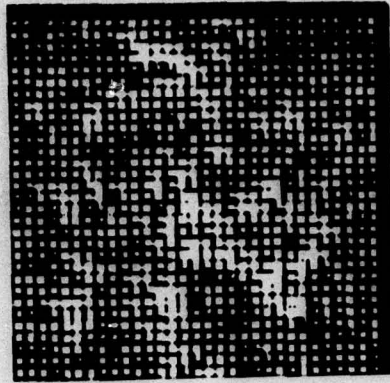
Figure 4-26. Intensity Contour Maps of the Unresolved Image of a Uniformly Illuminated Two-Point Target.  $D = 4 \text{ m}$ . Viewed through a  $0.65\text{-m}$  circular aperture at a range of  $450 \text{ km}$  using  $10.6 \mu\text{m}$  radiation. A static atmosphere with no absorption was assumed. The changes occurring with time are a result of the target's  $1.65 \text{ mrad/sec}$  rotation rate.



(A)



(B)



(C)

Figure 4-27. Gray-Scale Direct Detected Images of a Meteor Satellite for Three Levels of Turbulence. (A)  $\sigma_n \approx 0$ , (B)  $\sigma_n = 0.75$ , (C)  $\sigma_n = 2.4$ .

value of the outer scale,  $L_0$ . (See Sec. 2.2 and Fig. 2-3 for the definition of  $\sigma_n$  and  $L_0$ .) The bottom row of images (Fig. 4-24D-F) displays the change in the diffraction pattern for different values of  $L_0$ . In the computer model used, a change in  $L_0$  affects not only the value of  $\sigma_n$  computed, but also the cut-off frequency used for the spatial frequency spectrum. The effect of this cut-off frequency can be seen by comparing Fig. 4-24C with Fig. 4-24D. The pattern in Fig. 4-24D shows more random structure and dispersion of the beam even though the value of  $\sigma_n$  is less than for Fig. 4-24C.

Using the same phase array as for Fig. 4-24C (i.e.,  $\sigma_n = 2.4$ ), contour maps of direct-detected images of a two-point rotating target with and without turbulence are illustrated in Figs. 4-25 and 4-26. Figure 4-25 shows the two points resolved; Fig. 4-26 shows the two points unresolved. For the duration of the computer experiment (0.5 msec) the atmosphere was stationary. The effect of target rotation in the images with no atmosphere turbulence is to introduce fluctuations in the intensity of the two points. The phenomenon of "super-resolution" displayed in Fig. 4-26 where the two points appear to be resolved at  $T = 0.2$  msec, occurs for the special case of a two-point target, but is not of general interest for complex, diffuse objects. For the cases with turbulence present, the intensity of the two points appears to fluctuate and move about with time. The average of several images would result in increased blurring of the two points, with a corresponding decrease in resolution. If the averaging process encompassed a time interval over which the atmosphere changed significantly, an additional loss of resolution would be incurred. It might be mentioned that the decrease in resolution could be offset somewhat by correlating the peak intensities of successive images prior to averaging, but this technique would quickly break down for more complex objects.

The effects of turbulence on the direct-detected image of the Meteor spacecraft at an aspect angle normal to the cylindrical main body is

illustrated in Fig. 4-27. Resolution at the target was approximately 0.6 m and uniform illumination was used for each image. Figure 4-27A illustrates the speckled, blurred image with no turbulence. Figures 4-27B and C illustrate the images obtained for  $L_0 = 10$  m and  $\sigma_n = 0.75$  and 2.4 rad, respectively. The images illustrate that even a relatively small amount of turbulence severely degrades the image quality. The quality of the image could be improved simply by incoherently averaging a set of independent samples to reduce the effects of diffuse speckle as discussed in Sec. 4.2. Since both compensated imaging systems and non-imaging adaptive systems to reduce atmospheric effects on system performance have been the subject of numerous studies, they will not be pursued here.

#### 4.7.2 Atmospheric Effects on Synthetic Resolution

The atmosphere is often characterized as a time-invariant loss for the performance analysis of laser radar systems. However, the intensity and phase perturbations of the detected wavefront have a temporal power spectrum that sometimes exceeds 1 kHz. This temporal modulation can severely distort the received signal and subsequently reduce the performance of a radar system. In this section we will bound the magnitude of these effects by utilizing both experimental and theoretical data. To simplify the presentation of the data, we have assumed that the receiver has an aperture of 1 m and is operating at a wavelength of 10  $\mu$ m. The values are listed in Table 4-2 and can be scaled to other wavelengths as required.

The first link analyzed is an (space object identification) SOI application with a ground-based receiver interrogating a satellite in a low orbit. This mission will be referred to as Scenario 1.<sup>1</sup> The second mission (Scenario 2b)<sup>1</sup> assumes that the receiver is in a low-orbit satellite viewing a subsonic aircraft in level flight. In all cases it is assumed that the target is illuminated by a laser that is operating at a single wavelength and that the target has a distributed return that is generally diffuse.

<sup>1</sup>See Section 5.2 for scenario descriptions.

#### 4.7.2.1 Detection Technique

The characterization of the atmospheric degradation is highly dependent upon the type of optical detection used [i.e., (1) incoherent or direct detection, and (2) coherent or heterodyne detection] as well as the type of post-detection processing that is being used. The following post-detection techniques are representative of the three major classes of receivers.

Range Measurement with Incoherent Optical Detector. This is the commonly encountered detection scheme that is used in range finders that operate in a photon-counting mode.

Doppler Measurement. This system assumes that an optical heterodyne receiver is utilized to obtain the spectrum of the rotating target. An interval of the output signal is subsequently subjected to a Fourier analysis to determine the spectral characteristics of the received signal.

R/D Imaging. The matched filter detection of a large time-bandwidth product signal is assumed with the detector output signal being used for the generation of a synthetic image having the dimensions of time delay (range) and Doppler shift (cross range).

#### 4.7.2.2 Reciprocity Theorem

An important reference in the following discussions is the Reciprocity Theorem of the atmosphere, as first stated by Fried.<sup>1</sup> This theorem states that the scintillation detected by a point receiver from a point source with an intervening atmosphere will have the identical depth of scintillation when the roles of the source and the receiver are interchanged. Care must be taken in the application of this theorem since the introduction of a source or receiver that is larger than some characteristic dimension of the atmosphere will alter the reciprocity of the propagation of the wavefront.

---

<sup>1</sup>D. L. Fried and H. T. Yura, "Telescope Performance Reciprocity for Propagation in a Turbulent Medium," J. Opt. Soc. Am. 62, 600 (1972).

#### 4.7.2.3 Scintillation

The scintillation of the received signal for a typical vertical path through the atmosphere has been determined analytically<sup>1</sup> and experimentally<sup>2,3</sup> for the case of a point receiver. This value may be reduced by aperture averaging for satellite viewing (Scenario 1) due to the possible existence of high spatial frequencies in the received wavefront. However, calculations for Scenario 2b indicate that the spatial frequencies of the upward propagating beam will be extremely small (large spatial extent). Thus, the satellite optical receiver aperture of Scenario 2b does not average the received signal to reduce the depth of modulation of the received signal. From the Reciprocity Theorem, the two scenarios would have the same scintillation if the element located near the earth were physically small relative to the characteristic length of the atmosphere (less than a small fraction of a meter). However, since we have chosen a ground-based 1-m receiving aperture for Scenario 1 and a cruise missile for Scenario 2b, the conditions for the Reciprocity Theorem are violated. Since the turbulent medium is concentrated near the earth, the scintillation of Scenario 2b may be severe.

#### 4.7.2.4 Phase Modulation

The phase distortion of the wavefront propagating through the atmosphere is best characterized by the parameter,  $\sigma_\phi$  = RMS which is the deviation from the best fitting plane wavefront. In this calculation we have assumed that the tilt term of the phase-front modulation can be removed by the tracking operations of the receiver. This parameter has two components: the phase modulation that is associated with the scintillation that was previously discussed, and the phase modulation that is induced by perturbations that are optically near the receiving aperture. This parameter is important in that it indicates the efficiency of the

<sup>1</sup>W. N. Peters, "Phenomenological Model of Scintillation," Applied Optics, October 1976.

<sup>2</sup>AMOS Annual Report 1 January 1973-1 December 1973, AVCO Everett Research Laboratory, Inc., Report No. F04701-72-C-0081, December 1973.

<sup>3</sup>P. O. Minott et al., Results of Balloon Atmospheric Propagation Experiment Flights of 1970, Goddard Space Flight Center Document X-524-72-125 (March 1972).

of the receiver heterodyne process and also indicates that magnitude of of the phase jitter that is present in the detected heterodyne signal.

#### 4.7.2.5 Frequency Response of Perturbations

In the two scenarios that have been identified in this section, the relative velocities of the receiver and the target induce a slewing motion of the line of sight through the atmosphere. It is the translation of the atmospheric disturbances through the line of sight that gives rise to the temporal modulation of the received signal. Also, the boundary layer and the inviscid region surrounding the cruise missile of Scenario 2b have the potential of introducing high frequency modulation. Because of the uncertainty in the calculation of the boundary layer and engagement parameters, the frequencies listed in Table 4-2 for the phase and amplitude modulation should be considered as only representative.

#### 4.7.2.6 Differential Time Errors

It is conceivable that the dispersion of the atmosphere could induce differential time errors that could in turn induce a blurring in the range resolution of the system. However, when we consider that the phase errors (that are associated with the optical carrier frequency of  $3 \times 10^{13}$  Hz) are of the order of only a few cycles, it is obvious that the differential time delay between any two scattering centers of the target will be exceedingly small.

#### 4.7.2.7 Illumination

The illuminator wavefront will suffer both phase and amplitude perturbations as it propagates through the atmosphere. The absolute phase of the illumination beam impinging upon a diffuse target is unimportant due to the random nature of the diffuse surface. However, temporal modulation of the phase may adversely effect phase-sensitive measurements such as range-Doppler imaging. The intensity variations introduced by the atmosphere can have an adverse effect upon the system performance since this

TABLE 4-2

## DESCRIPTION OF ATMOSPHERIC EFFECTS ON SYSTEM OBSERVABLES

Mission Observable	Scintillation	Phase Front Modulation	Maximum Frequency	Aperture Averaging	Differential Timing Errors
Scenario 1 SOF	Range (Power)	N/A	100 → 300 Hz	Yes	$<10^{-12}$ sec
	Doppler (E-field)	$\Delta A \sim 0.5 \rightarrow 2\lambda$		No	
	R/D (E-field)	0			
	Illumination (Power)	RMS ~ 1 → C.T. 20%			
Scenario 2b	Range (Power)	N/A			
	Doppler (E-field)	RMS ~ 0.1 → 5%			
	R/D (E-field)	RMS ~ 0.1 → 5%			
	Illumination (Power)	RMS ~ 1 → L.T. 20%			

perturbation of the beam will both spatially and temporally modify the target-distributed radiance. The atmospheric noise will be especially detrimental to the system performance if it has a bandwidth that exceeds the characteristic frequencies of the post-detection processing electronics.

#### 4.7.2.8 Effect of Errors upon System Operation

The time delays and phase modulation of the detected wavefront reduce the accuracy to which we may make the range, Doppler, and the R/D imaging operations. For example, the phase errors will be one of the factors that determine the lower limit of the frequency resolution of the Doppler measurements. From the values listed in Table 4-2, it appears that the systems of Scenarios 1 and 2b cannot expect to have a Doppler resolution better than a few hundred hertz. The limits in the accuracy of the range measurements as determined from atmospheric considerations will be sufficiently small to be ignored. By this we do not imply that the measurement of the absolute time delay (as would be required for the calculation of the range to the target) will be exact. In practice, the uncertainty introduced by the unknown refractive index profile will limit the accuracy of this measurement.

## 5 SCENARIO STUDIES

In order to provide a more realistic assessment of the type of laser radar data likely to be observed for the targets discussed in Sec. 4.1, a geometrical and dynamical computer model was assembled, describing an encounter between each target and a hypothetical satellite-borne radar. An encounter between a ground-based radar and a satellite was also modeled. The following section describes the simulator itself, with some results for the observed total cross section presented in Sec. 5.2.

### 5.1 SIMULATOR DESCRIPTION

The computer simulator was designed to provide a time sequence of both scalar (e.g., range, aspect angles) and vector (e.g., rotation axis) quantities of interest for a laser radar viewing a target. A few considerations are common to all the scenarios. In all cases, time zero corresponds to the occurrence of minimum range between the radar and the target, with negative times describing the period during approach to minimum range, etc. Because of the relative motion between the radar and target center of mass, the latter has an apparent rotational motion with respect to the former. Where appropriate, this quantity was combined (vectorially) with any motion of the target about its center of mass. Since the various targets are oriented only relative to the radar (and not with respect to the earth) the rotation of the earth was not included.

Five scenarios were modeled. Table 5-1 lists their targets, the radar locations, the user-supplied parameters and their symbols, and representative values chosen for some of the exercises in Sec. 5.2.

Figure 5-1 shows the parameters modeled for a ground-based radar viewing a satellite (Scenario 1). The radar antenna is placed at a specified height above the surface of the earth. The orbital plane of the satellite intersects the surface of the earth at a minimum distance  $D$  (measured along the surface of the earth) from the radar site. The space object is placed in a circular orbit at altitude  $H_s$ . Since the

TABLE 5-1  
ENCOUNTER SIMULATOR PROGRAM INPUT PARAMETERS

Scenario Number	Radar Location	Target	User-Supplied Parameters	Value	Figure Number
1	Attached to Earth Surface	Satellite (Meteor)	Radar antenna height (above earth surface) Satellite orbital altitude, $H_S$ Minimum distance from radar to satellite ground track (along earth surface), $D$ Angle between satellite solar paddle axis and satellite orbital plane, $\psi$	0 1000 km 0, 250, 500 km 0°, 90°, 180°	5-1
2a	Satellite	Satellite (Meteor)	Radar orbital altitude, $H_R$ Satellite orbital altitude, $H_S$ Angle between radar and satellite orbital planes, $\beta$ Angle between satellite solar paddle axis and satellite orbital plane, $\psi$	500 km 1000 km 0°, 20° 0°, ±90°	5-2
2b	Satellite	Cruise Missile (Styx)	Radar orbital altitude, $H_R$ Missile altitude Missile velocity Angle between radar orbital plane and plane of missile motion, $\beta$	500 km 0.1 km 0.25 km/sec 20°	5-2
2c	Satellite	SLBM Near Launch	Radar orbital altitude, $H_R$ Rocket altitude at closest approach to radar, $H_a$ Rocket spin rate Rocket average velocity during encounter Angle between radar orbital plane and rocket (line) trajectory, $\beta$	500 km 25 km 0 1 km/sec 0°, 10°, 20°	5-3
2d	Satellite	RV	Radar orbital altitude RV apogee altitude, $H_A$ RV ground range, $R_g$ Angle between radar orbital plane and RV trajectory plane, $\beta$ RV spin or tumble rate	500 km 250 km 10,000 km 0°, 20° 0.85 Hz	5-4

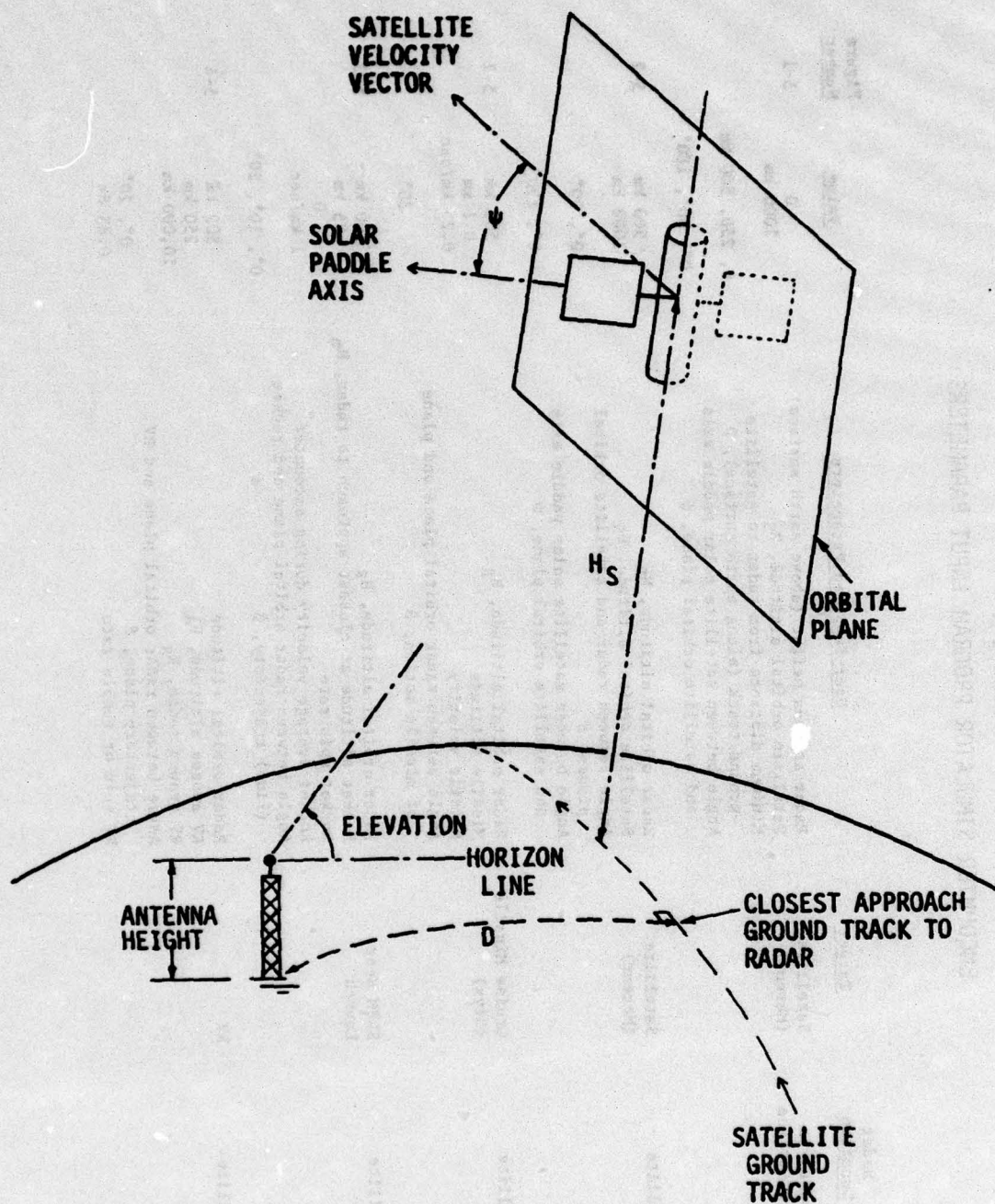


Figure 5-1. Encounter Between Ground-Based Radar and a Satellite (Scenario 1)

Meteor satellite is not azimuthally symmetric, provision was made to specify the orientation of the solar paddle axis with respect to the orbital plane (angle  $\psi$ ). Utilization of the parameters  $D$  and  $\psi$  can provide a wide variety of viewing aspects.

The Meteor satellite is an earth-center stabilized object. Thus, the symmetry axis of the cylindrical section always points to the center of the earth. This requires that the satellite rotate about its center of mass with a period equal to the orbital period (and with the rotation axis perpendicular to the orbital plane). For the parameters selected in Sec. 5.2, this "proper" motion accounts for 10% to 30% of the satellite rotation rate as seen by the radar.

Figure 5-2 shows the parameters relevant for describing the encounter between a satellite-borne radar and another satellite or a cruise missile (Scenario 2a). Both objects are placed in circular orbits at altitudes  $H_R$  and  $H_S$ , respectively. The angle between the orbital planes ( $\beta$ ) is arbitrary. The orientation of the Meteor's solar paddles is again specified by  $\psi$ . An additional consideration in describing the motions of two space objects is the direction of their orbital rotations relative to each other. Both co- and counter-rotating motions are allowed in the simulator. In either case, at time zero the two objects are located along the line of intersection of their orbital planes.

The same basic configuration shown in Fig. 5-2 can be used to describe the encounter with a cruise missile (Scenario 2b). The missile altitude ( $H_S$ ) is, of course, very small compared with orbital altitudes. The most important difference between satellite and cruise missile targets is that the velocity of the former is determined by orbital mechanics, while that of the latter is specified in the simulator by the user. The Styx missile was maintained in a horizon-stabilized flight by rotating the object about its center of mass in a manner analogous to that of the stabilized satellite.

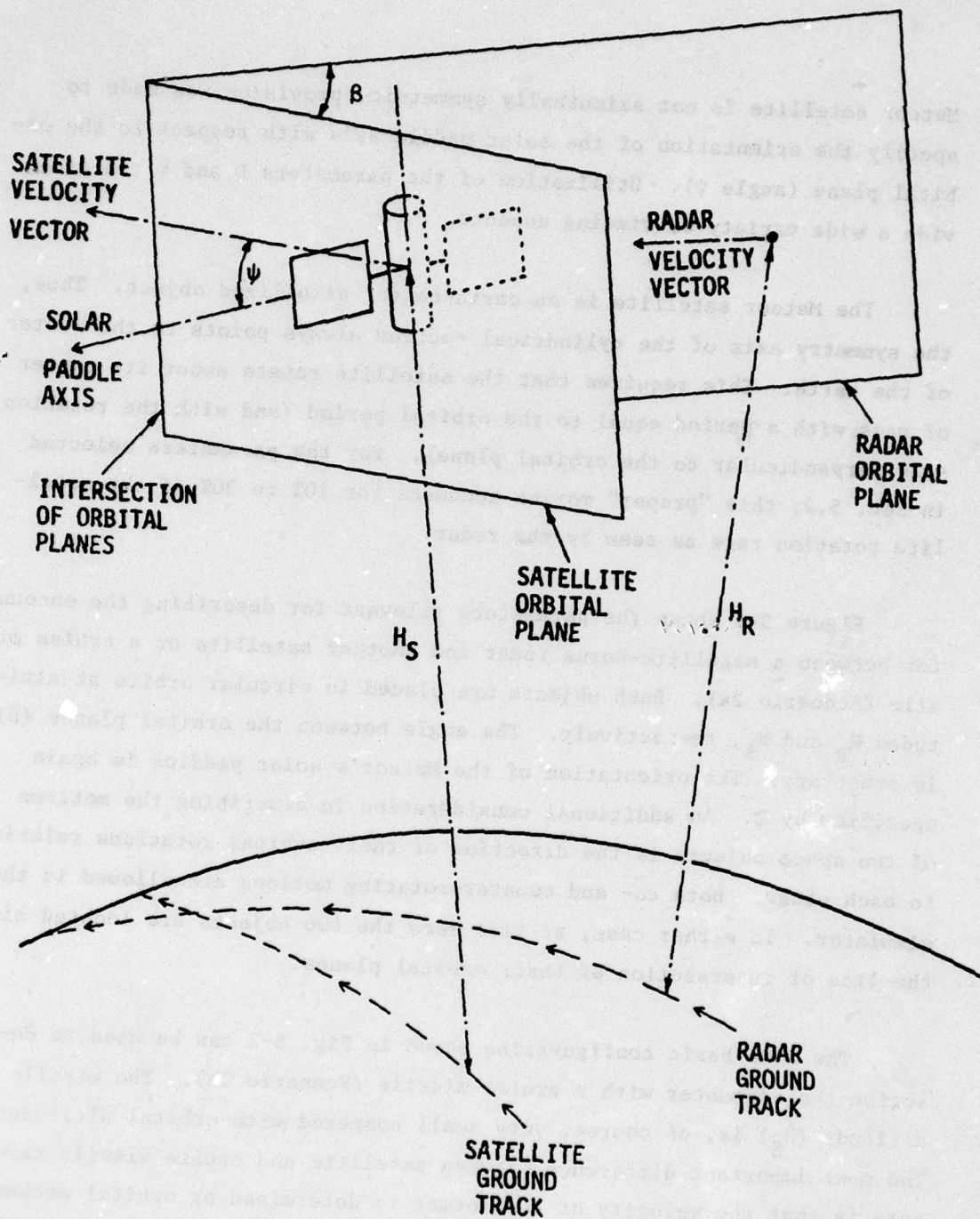


**Figure 5-2.** Encounter Between Satellite-Borne Radar and a Satellite (Scenarios 2a and 2b)

The encounter between the satellite-borne radar and an SLBM near launch is shown in Fig. 5-3 (Scenario 2c). Since the main interest for this case was for times very near the launch point of the rocket, no detailed modeling of the rocket trajectory was performed. Rather, the object was moved along the straight line connecting the center of the earth and the launch point ( $R_e$  is the earth radius). Further, the velocity of the rocket was set to some average value likely to occur during the first few minutes of flight. Time zero occurred when the rocket was at a user-specified altitude,  $H_m$ , and the radar was at its minimum distance from that point. Note that the straight-line trajectory can make an angle  $\beta$  with the radar orbital plane. Finally, the simulator allows the SLBM to spin about its symmetry axis during flight.

The last encounter (Scenario 2d) to be simulated relates the satellite-borne radar and an RV as shown in Fig. 5-4. Two parameters are required to fit an ellipse to the RV trajectory. The two selected here are ground range,  $R_g$ , and altitude at apogee,  $H_A$ . As before,  $\beta$  is the angle between the two planes of motion, time zero occurs when the two objects lie along the line of intersection of these two planes, and the radar and target may rotate in the same or opposite directions.

The dynamical motion of the RV is, in general, a complicated six-degree-of-freedom problem. A much simplified model was used here. The RV symmetry axis was held fixed along a line in the plane of the trajectory and parallel to the tangent line to the trajectory at the impact point. In this manner, the RV was oriented properly for reentry. The spinning RV was maintained in a "nose down" position while being spun about its symmetry axis; the tumbling RV rotated about an axis perpendicular to the symmetry axis and in the trajectory plane.

## 5.2 RESULTS OF SIMULATIONS

The variety of input parameters listed in Table 5-1 for the computer simulator shows that a very large number of different cases can be modeled.

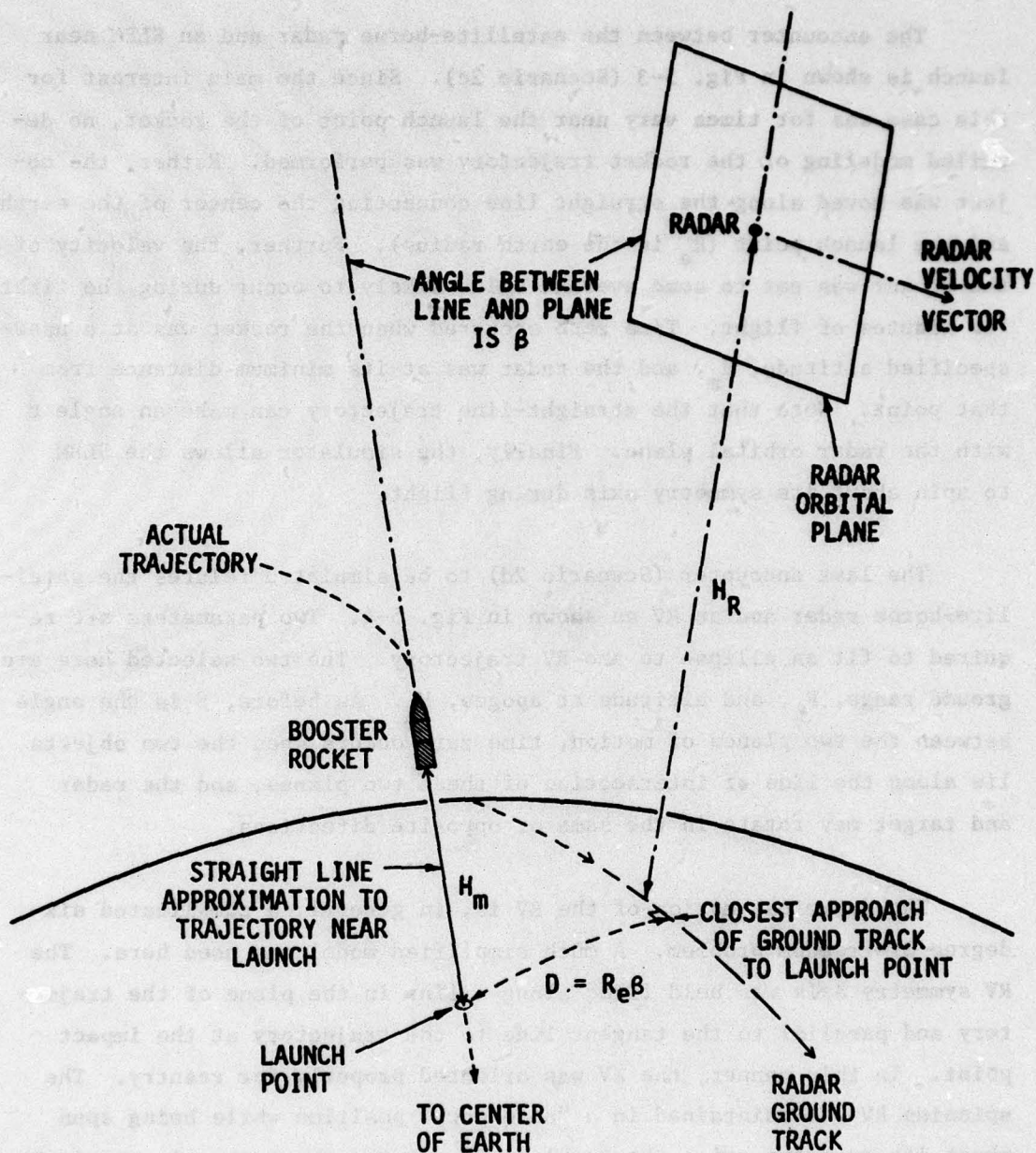


Figure 5-3. Encounter Between Satellite-Borne Radar and a Booster Rocket Near Launch (Scenario 2c)

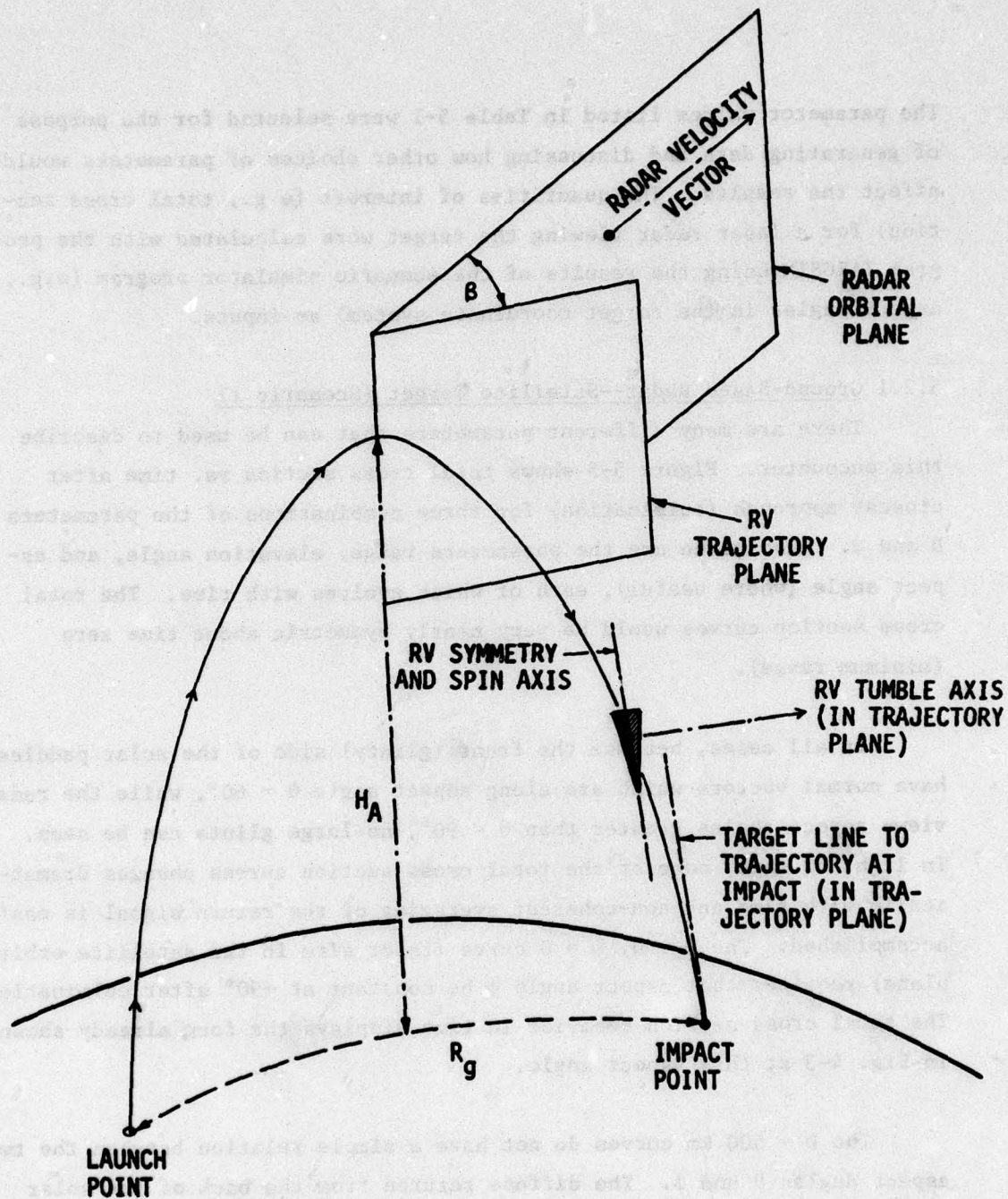


Figure 5-4. Encounter Between Satellite-Borne Radar and an RV (Scenario 2d)

The parameter values listed in Table 5-1 were selected for the purpose of generating data and discussing how other choices of parameters would affect the results. The quantities of interest (e.g., total cross section) for a laser radar viewing the target were calculated with the program TARGSIM using the results of the scenario simulator program (e.g., aspect angles in the target coordinate system) as inputs.

#### 5.2.1 Ground-Based Radar--Satellite Target (Scenario 1)

There are many different parameters that can be used to describe this encounter. Figure 5-5 shows total cross section vs. time after closest approach (culmination) for three combinations of the parameters  $D$  and  $\psi$ . Also given are the parameters range, elevation angle, and aspect angle (where useful), each of which evolves with time. The total cross section curves would be very nearly symmetric about time zero (minimum range).

In all cases, because the front (glinty) side of the solar paddles have normal vectors which are along aspect angle  $\theta = 60^\circ$ , while the radar views aspect angles greater than  $\theta = 90^\circ$ , no large glints can be seen. In light of this, none of the total cross section curves changes dramatically with time and non-coherent averaging of the return signal is easily accomplished. The  $D = 0, \psi = 0$  curve (radar site in the satellite orbital plane) requires that aspect angle  $\phi$  be constant at  $+90^\circ$  after culmination. The total cross section behavior in time displays the form already shown in Fig. 4-3 at this aspect angle.

The  $D = 500$  km curves do not have a simple relation between the two aspect angles  $\theta$  and  $\phi$ . The diffuse return from the back of the solar paddles is always larger for this scenario than that from the front of the paddles. This causes the increase by a factor of three in total cross section near culmination for  $\psi = 0^\circ$  vs.  $\psi = 180^\circ$ . However, the proper combination of aspect angles needed to view the glint at or near normal incidence to the back of the solar paddles does not occur.

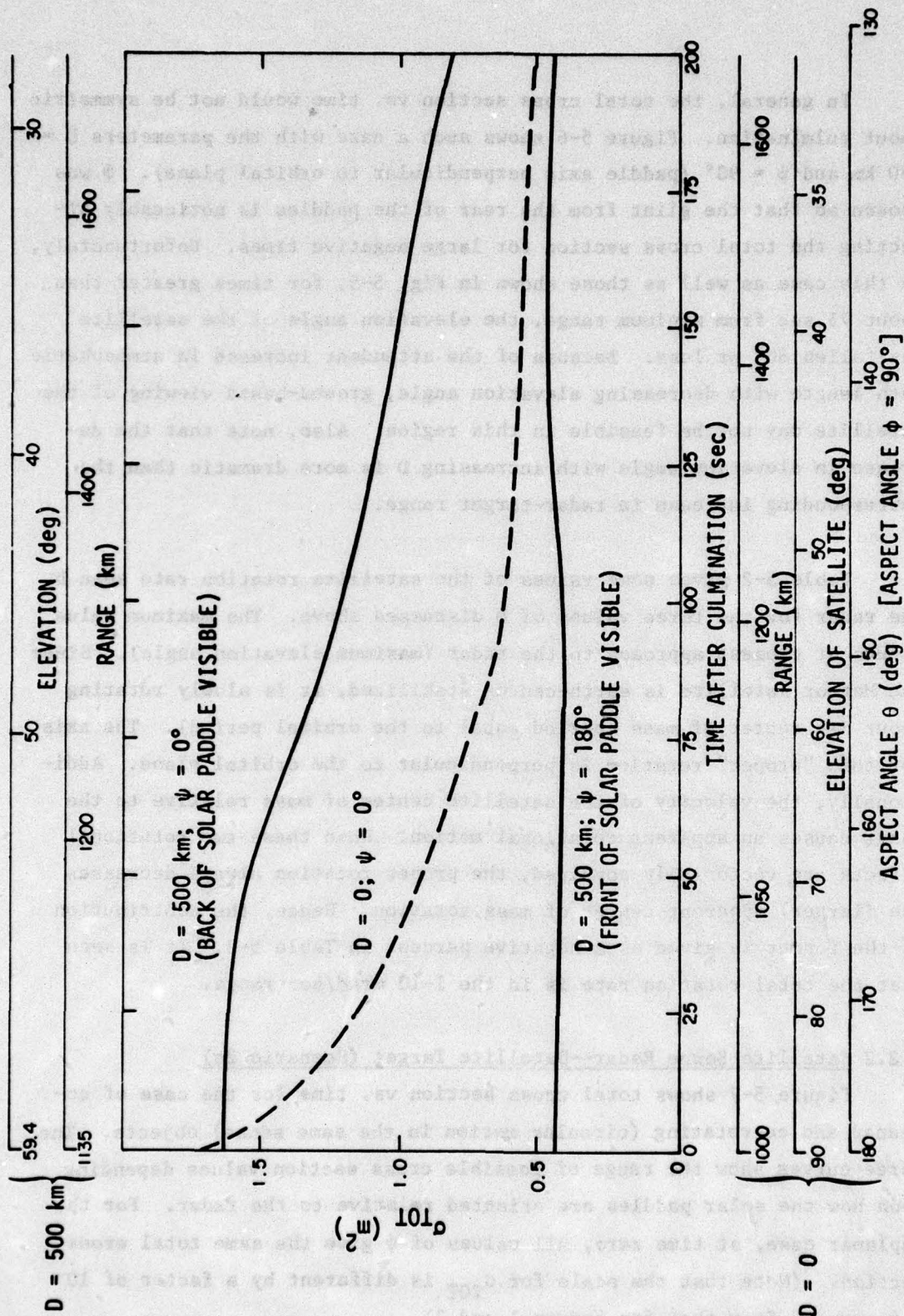


Figure 5-5. Total Cross Section After Minimum Approach Observed by Ground-Based Radar for Satellite Encounter

In general, the total cross section vs. time would not be symmetric about culmination. Figure 5-6 shows such a case with the parameters  $D = 250$  km and  $\psi = 90^\circ$  (paddle axis perpendicular to orbital plane).  $\psi$  was chosen so that the glint from the rear of the paddles is noticeably affecting the total cross section for large negative times. Unfortunately, in this case as well as those shown in Fig. 5-5, for times greater than about 75 sec from minimum range, the elevation angle of the satellite has fallen  $60^\circ$  or less. Because of the attendant increase in atmospheric path length with decreasing elevation angle, ground-based viewing of the satellite may not be feasible in this region. Also, note that the decrease in elevation angle with increasing  $D$  is more dramatic than the corresponding increase in radar-target range.

Table 5-2 gives some values of the satellite rotation rate seen by the radar for the three values of  $D$  discussed above. The maximum value occurs at closest approach to the radar (maximum elevation angle). Since the Meteor satellite is earth-center stabilized, it is slowly rotating about its center of mass (period equal to the orbital period). The axis for this "proper" rotation is perpendicular to the orbital plane. Additionally, the velocity of the satellite center of mass relative to the radar causes an apparent rotational motion. When these two rotational effects are vectorially combined, the proper rotation always decreases the (larger) apparent center of mass rotation. Hence, the contribution of the former is given as a negative percent in Table 5-2. It is seen that the total rotation rate is in the 1-10 mrad/sec range.

#### 5.2.2 Satellite-Borne Radar--Satellite Target (Scenario 2a)

Figure 5-7 shows total cross section vs. time for the case of coplanar and co-rotating (circular motion in the same sense) objects. The three curves show the range of possible cross section values depending upon how the solar paddles are oriented relative to the radar. For the coplanar case, at time zero, all values of  $\psi$  give the same total cross section. (Note that the scale for  $\sigma_{TOT}$  is different by a factor of 10 for curve 3 from that for curves 1 and 2).

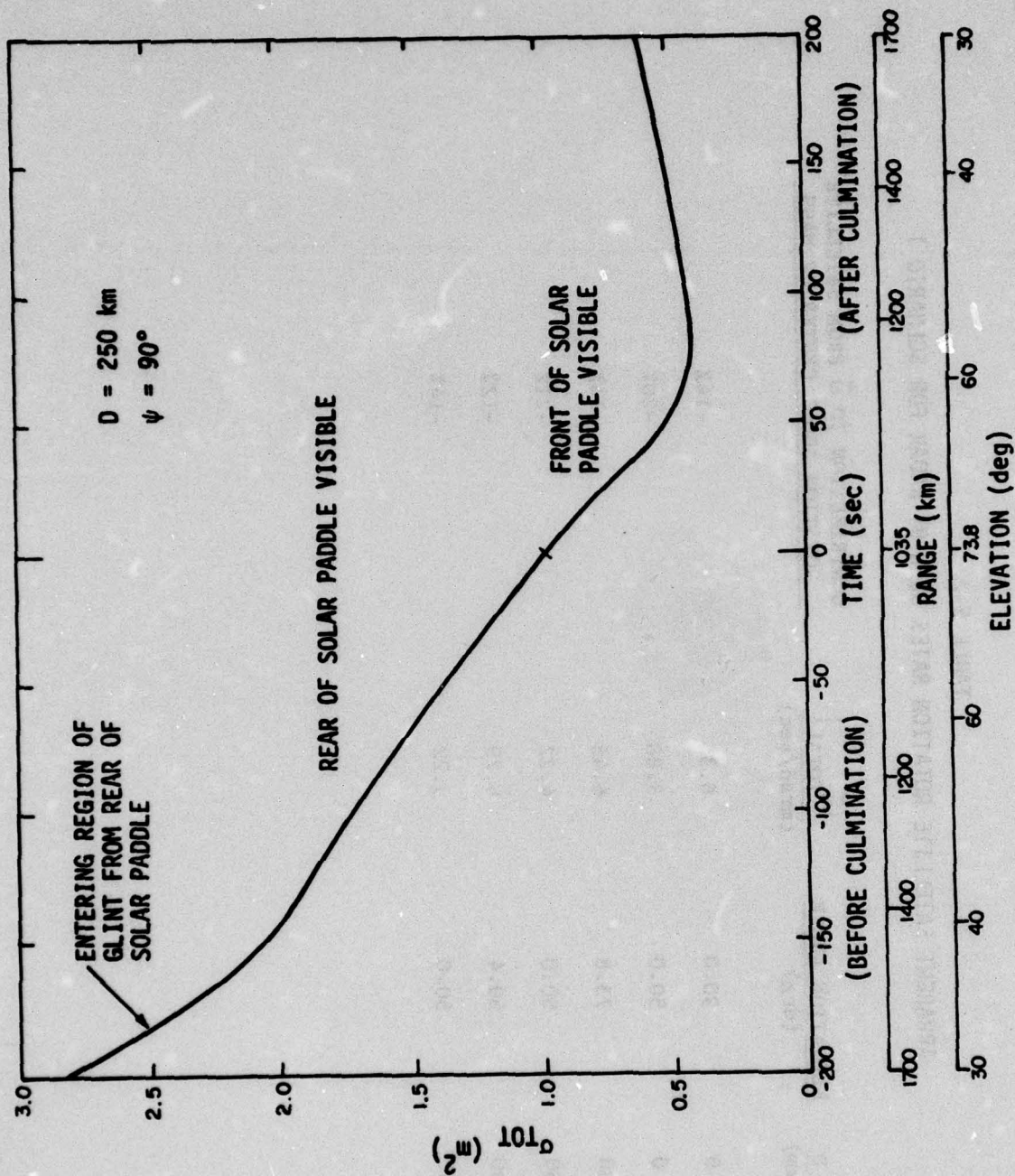


Figure 5-6. Total Cross Section Observed by Ground-Based Radar During Satellite Encounter

TABLE 5-2  
APPARENT SATELLITE ROTATION RATES SEEN BY RADAR FOR SCENARIO 1

$\frac{D}{(km)}$	ELEVATION ANGLE (deg)	$\left  \vec{\omega}_{TOTAL} \right $ (mrad/sec)	CONTRIBUTION TO $\vec{\omega}$ FROM SATELLITE ROTATION ABOUT CENTER OF MASS
0	90.0	6.35	-14%
0	50.0	3.88	-20%
250	73.8	6.45	-14%
250	50.0	4.22	-21%
500	59.4	6.29	-12%
500	50.0	5.22	-14%

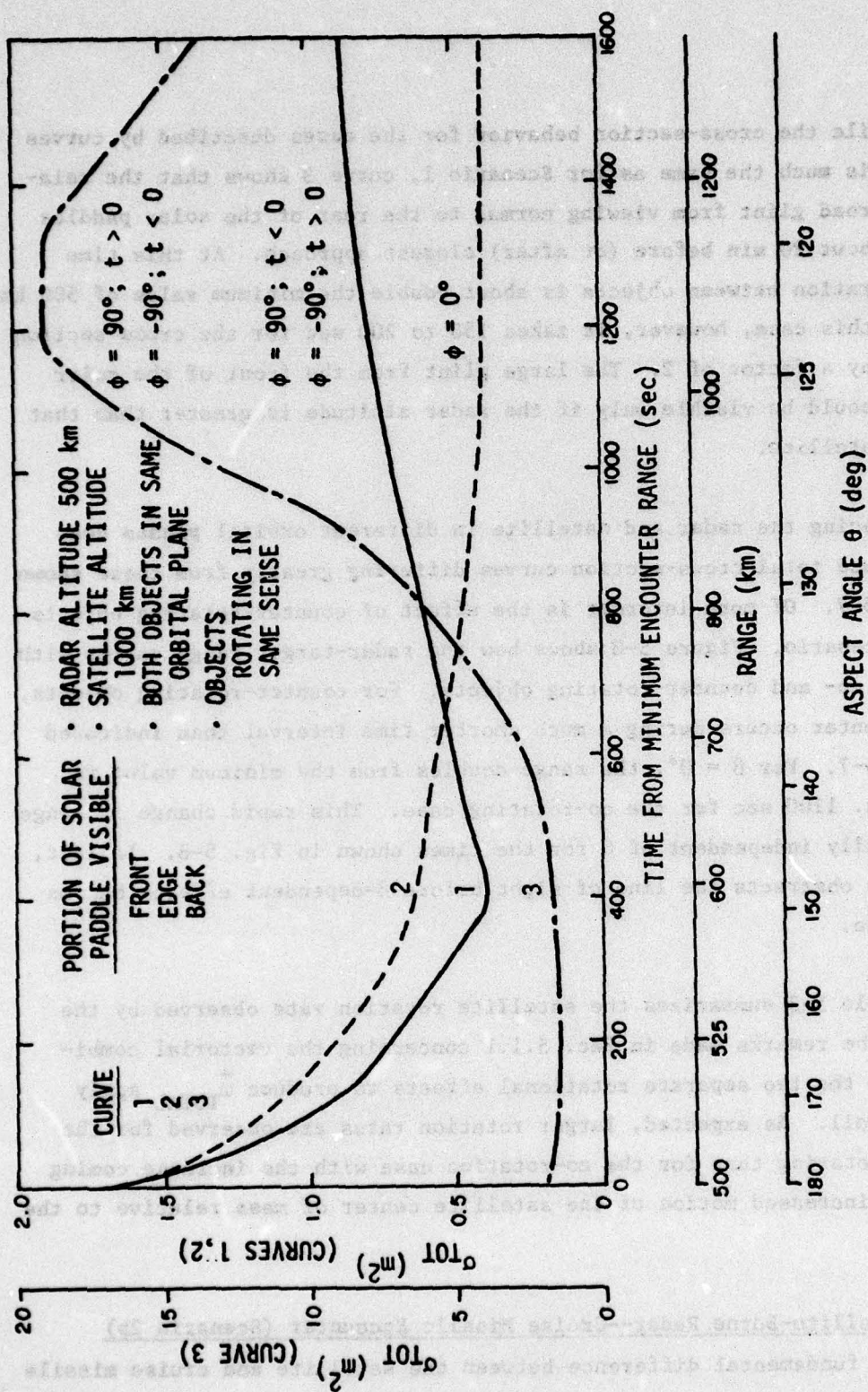


Figure 5-7. Total Cross Section Observed by Satellite-Borne Radar During Satellite Encounter

While the cross-section behavior for the cases described by curves 1 and 2 is much the same as for Scenario 1, curve 3 shows that the relatively broad glint from viewing normal to the rear of the solar paddles occurs about 20 min before (or after) closest approach. At this time the separation between objects is about double the minimum value of 500 km. Even in this case, however, it takes 150 to 200 sec for the cross section to vary by a factor of 2. The large glint from the front of the solar paddles could be visible only if the radar altitude is greater than that of the satellite.

Placing the radar and satellite in different orbital planes does not produce total cross-section curves differing greatly from those shown in Fig. 5-7. Of more interest is the effect of counter-rotating objects on the scenario. Figure 5-8 shows how the radar-target range varies with time for co- and counter-rotating objects. For counter-rotating objects, the encounter occurs during a much shorter time interval than indicated in Fig. 5-7. For  $\beta = 0^\circ$ , the range doubles from the minimum value in 55 sec vs. 1100 sec for the co-rotating case. This rapid change in range is virtually independent of  $\beta$  for the times shown in Fig. 5-8. In fact, the earth obstructs the line of sight before  $\beta$ -dependent effects become noticeable.

Table 5-3 summarizes the satellite rotation rate observed by the radar. The remarks made in Sec. 5.1.1 concerning the vectorial combination of the two separate rotational effects to produce  $\vec{\omega}_{TOTAL}$  apply here as well. As expected, larger rotation rates are observed for the counter-rotating than for the co-rotation case with the increase coming from the increased motion of the satellite center of mass relative to the radar.

### 5.2.3 Satellite-Borne Radar--Cruise Missile Encounter (Scenario 2b)

The fundamental difference between the satellite and cruise missile encounters is that the missile velocity is much smaller than the satellite

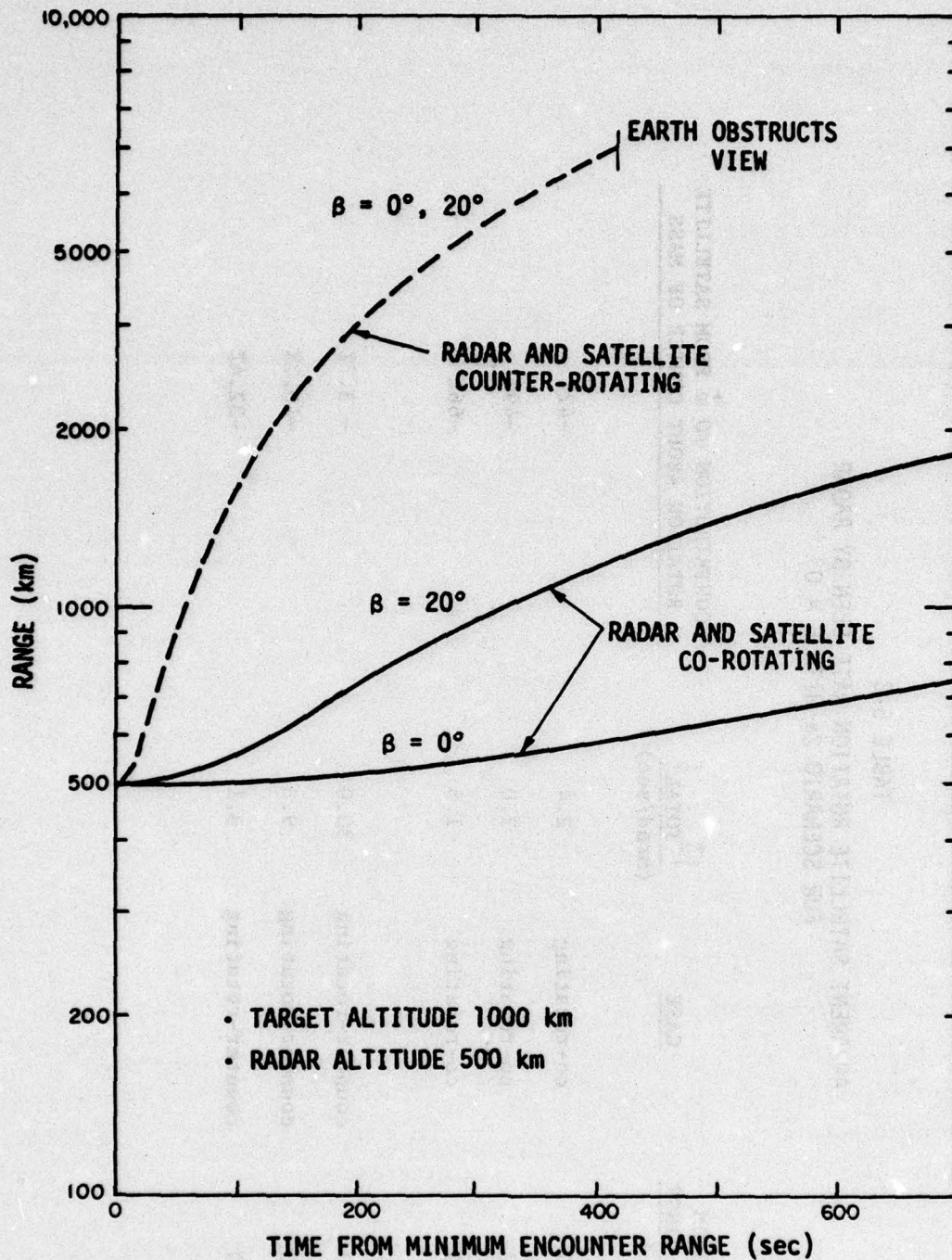


Figure 5-8. Range vs. Time Comparisons for Co- and Counter-Rotating Satellite-Satellite Encounter

TABLE 5-3  
APPARENT SATELLITE ROTATION RATE SEEN BY RADAR  
FOR SCENARIO 2a WITH  $\beta = 0^\circ$

TIME FROM MINIMUM RANGE (sec)	CASE	$ \vec{\omega}_{TOTAL} $ (mrad/sec)	CONTRIBUTION TO $\vec{\omega}$ FROM SATELLITE ROTATION ABOUT CENTER OF MASS
0	co-rotating	2.4	-42%
500	co-rotating	2.0	-49%
1000	co-rotating	1.5	-66%
0	counter-rotating	30.0	- 3.7%
50	counter-rotating	9.3	-10.7%
100	counter-rotating	3.1	-32.4%

orbital velocity. A value of 560 mph (0.25 km/sec) is used here. Because the radar velocity is about 7.6 km/sec (500-km altitude orbit), the encounter is virtually unaffected by whether the radar and missile are co- or counter-rotating. The missile altitude is 100 m.

The major feature of the total cross section of the Styx missile (Fig. 4-6) is the large peak at normal viewing to the wings. Since the encounter simulator places the radar and target along the line of intersection of their respective planes of motion at time zero, the total cross section vs. time curve will always display this feature independent of  $\beta$ . Figure 5-9 shows such a curve for  $\beta = 20^\circ$ . While the large value of  $\sigma_{TOT}$  would seem to ensure a measurable return signal, it should be remembered that the effect of the atmosphere has not been included. Also, for this scenario, the earth is in the background during the encounter.

Like the Meteor satellite, the Styx missile is in an attitude-stabilized position during flight. However, as Table 5-4 shows, the principal source of apparent rotation is caused by the relative motion of the missile center of mass relative to the radar. Again, rotation rates of about 1-10 mrad/sec are observed.

#### 5.2.4 Satellite-Borne Radar--Booster Rocket Encounter (Scenario 2c)

As described previously, the booster rocket was flown along a straight-line trajectory from launch with a constant velocity. For the SLBM modeled here, the average velocity during the first minute or so of flight is between 1 and 2 km/sec. Figure 5-10 shows the observed total cross section vs. time after launch for three values of  $\beta$ . Because only the first 80 sec of flight are covered, the radar-rocket range is relatively constant. Minimum range occurs when the rocket reaches an altitude of 25 km. For longer times, the straight-line approximation would certainly not be valid.

AD-A035 880

GENERAL RESEARCH CORP MCLEAN VA WASHINGTON OPERATIONS  
SENSOR MODULATION EFFECTS UPON LASER SIGNATURES.(U)

F/G 17/8

UNCLASSIFIED

DEC 76 J L GILBERT, P J KRAMER, W N PETERS

F30602-75-C-0292

905-01-CR

RADC-TR-76-391

NL

2 of 2  
ADA035880



END

DATE  
FILMED  
3 - 77

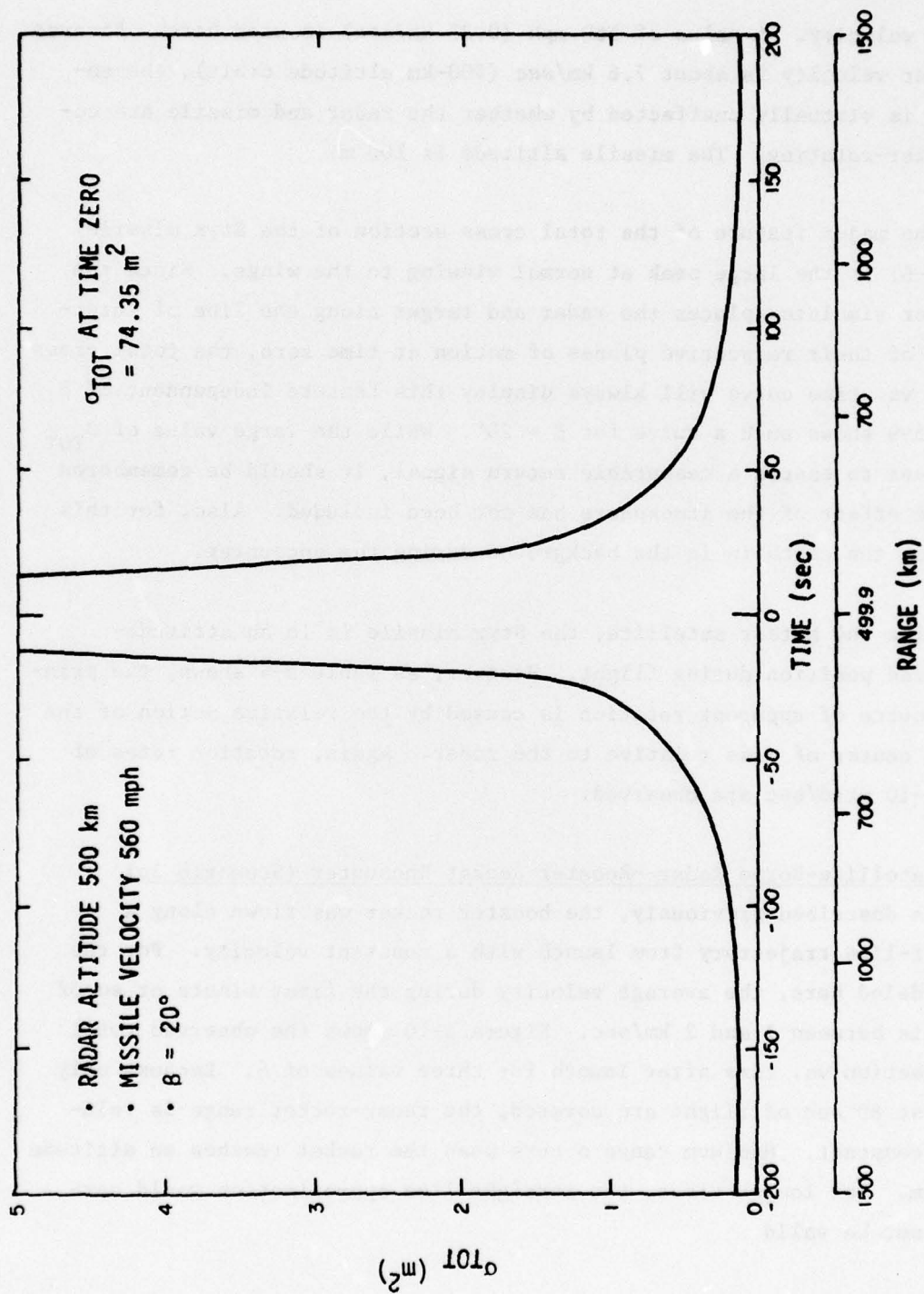


Figure 5-9. Total Cross Section Observed by Radar During Cruise Missile Encounter

TABLE 5-4  
 APPARENT MISSILE ROTATION RATE SEEN BY RADAR  
 FOR SCENARIO 2b WITH  $\beta = 20^\circ$

TIME FROM MINIMUM RANGE (sec)	$ \vec{\omega}_{\text{TOTAL}} $ (mrad/sec)	CONTRIBUTION TO $\vec{\omega}$ FROM MISSILE ROTATION ABOUT CENTER OF MASS
0	13.6	-0.25%
50	8.9	-0.41%
100	4.1	-0.79%

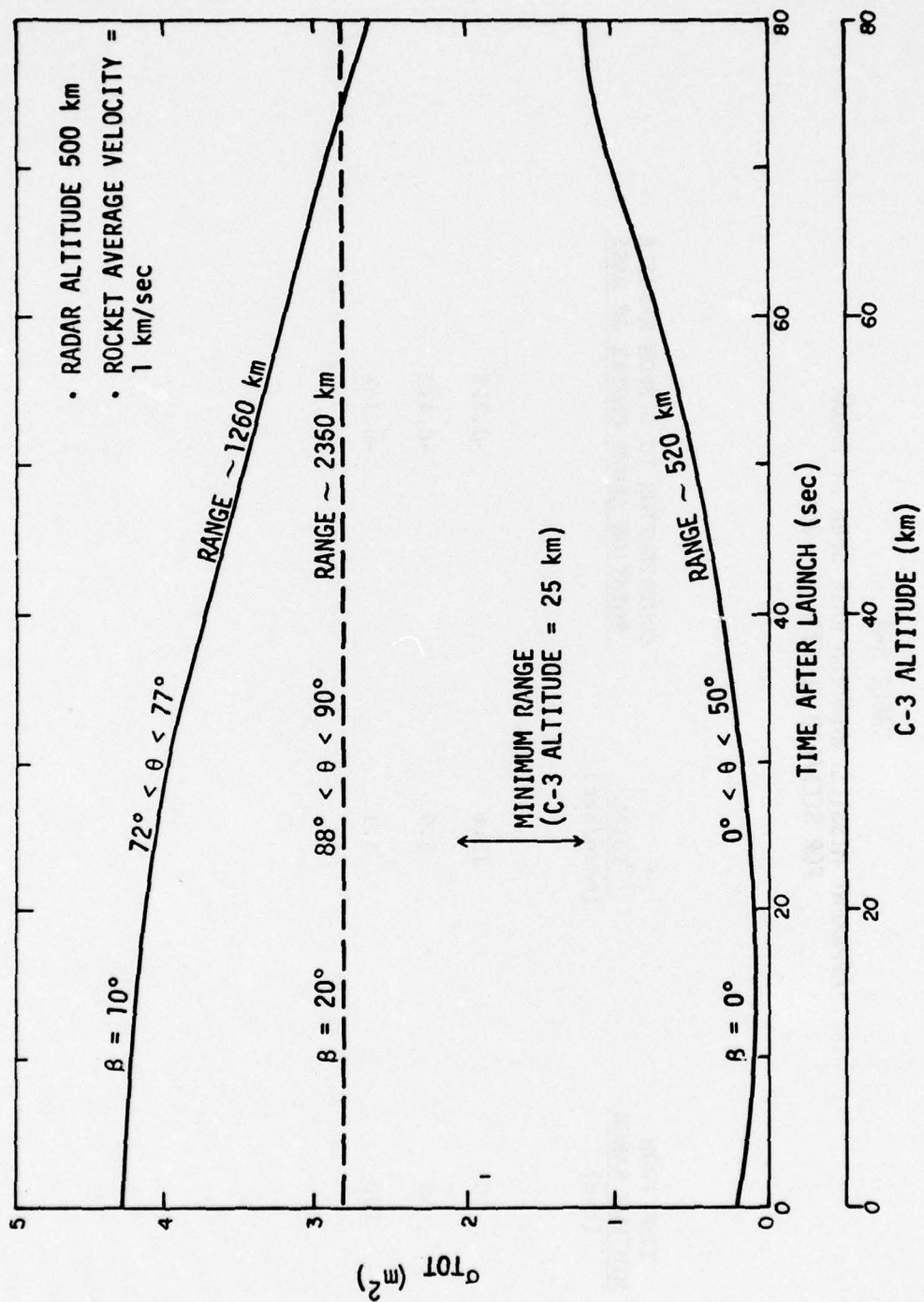


Figure 5-10. Total Cross Section Observed During Radar Encounter with Booster Rocket

The  $\beta = 0^\circ$  (coplanar) case shows a  $50^\circ$  change in viewing aspect; however, the  $\beta \neq 0$  cases allow much more restricted viewing. The  $\beta = 10^\circ$  case displays values of  $\sigma_{TOT}$  occurring on the steep portion of the complete total cross section curve shown in Fig. 4-9 ( $\theta$  between  $72^\circ$  and  $77^\circ$  in Fig. 4-9). In the actual encounter, this 25% change in cross section is spread over more than 1 min and does not appear as a rapid variation in  $\sigma_{TOT}$ .

Two general comments may be made concerning this scenario. (1) For  $\beta > 22^\circ$ , the radar cannot view the rocket until some minimum altitude is attained. (For  $\beta = 30^\circ$ , this minimum altitude is 63 km; alternatively, for  $\beta = 30^\circ$ , the radar orbital altitude would have to be greater than 987 km to view the launch site.) (2) Changing the average rocket velocity merely scales the time of the encounter in an inverse manner.

No motion of the booster rocket about its center of mass was included. The rotation rates given in Table 5-5 are once again in the mrad/sec range. The rates peak at minimum range (time after launch = 25 sec for 1 km/sec average velocity).

#### 5.2.5 Satellite-Borne Radar--RV Encounter (Scenario 2d)

The RV encounter was simulated for two different types of RV motion; spin and tumble. In each case, the rotation rate used was 0.85 Hz. For an azimuthally symmetric RV, the spinning motion does not affect the total cross section vs. time data. The RV used for the simulation (Fig. 4-10) was not symmetric because of the presence of the four small windows on the principal conic section. If at some time the radar-RV line-of-sight vector is nearly normal to the cone (within the width of the BDR of the window materials), the total cross section will oscillate between two values at a rate up to four times that of the spin motion.

Figure 5-11 gives the observed total cross section vs. time for the spinning RV for both co-rotating and counter-rotating scenarios. The

TABLE 5-5  
APPARENT BOOSTER ROCKET ROTATION RATES SEEN BY RADAR FOR SCENARIO 2c

<u>TIME FROM LAUNCH</u> (sec)	$\beta$ (deg)	$ \vec{\omega}_{TOTAL} $ (mrad/sec)
0	0	12.8
25	0	14.9
50	0	13.0
0	10	5.49
25	10	5.63
50	10	5.53
0	20	2.83
25	20	2.86
50	20	2.85

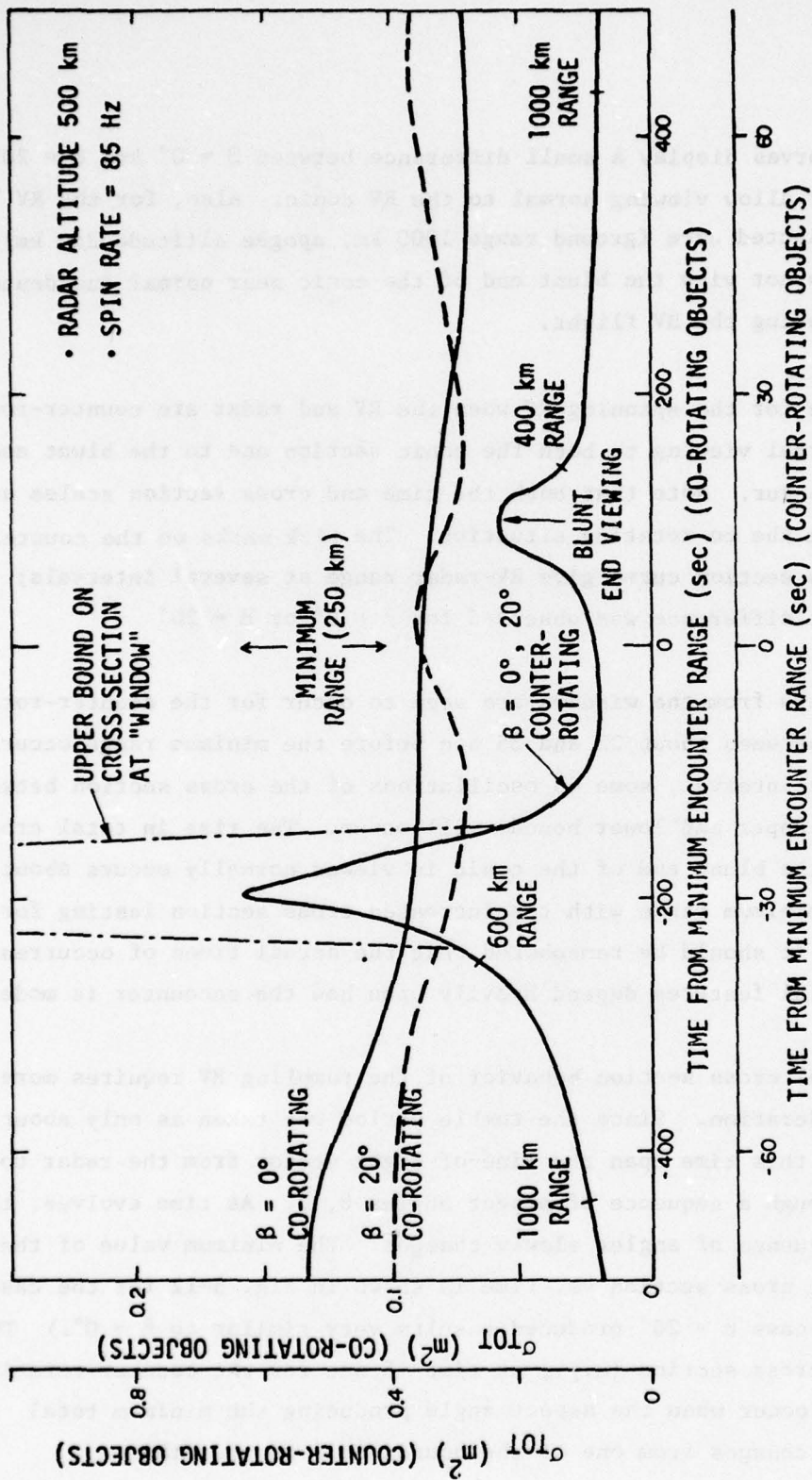


Figure 5-11. Total Cross Section Observed During Radar Encounter with Spinning RV

co-rotating curves display a small difference between  $\beta = 0^\circ$  and  $\beta = 20^\circ$ , but they never allow viewing normal to the RV conic. Also, for the RV trajectory selected here (ground range 1000 km, apogee altitude 250 km), the radar does not view the blunt end of the conic near normal incidence at any time during the RV flight.

The data for the spinning RV when the RV and radar are counter-rotating shows that normal viewing to both the conic section and to the blunt end of the RV can occur. Note that both the time and cross section scales are different from the co-rotating situation. The tick marks on the counter-rotating cross section curve give RV-radar range at several intervals; no significant difference was observed for  $\beta = 0^\circ$  or  $\beta = 20^\circ$ .

The glints from the windows are seen to occur for the counter-rotating RV and radar between about 22 and 35 sec before the minimum range occurs. In this 13-sec interval, some 45 oscillations of the cross section between the indicated upper and lower bounds will occur. The rise in total cross section when the blunt end of the conic is viewed normally occurs about 15 sec after minimum range with the increased cross section lasting for about 7 sec. It should be remembered that the actual times of occurrence of these special features depend heavily upon how the encounter is modeled.

The total cross section behavior of the tumbling RV requires more careful consideration. Since the tumble period was taken as only about 1.2 sec, over this time span the line-of-sight vector from the radar to the RV sweeps through a sequence of aspect angles  $\theta$ ,  $\phi$ . As time evolves, the particular sequence of angles slowly changes. The minimum value of the observed total cross section vs. time is shown in Fig. 5-12 for the case  $\beta = 0^\circ$ . (The case  $\beta = 20^\circ$  produced results very similar to  $\beta = 0^\circ$ .) The cusps in the cross section (e.g., at time -5 sec for the counter-rotating objects case) occur when the aspect angle producing the minimum total cross section changes from one of the bounds on  $\theta$  to the other.

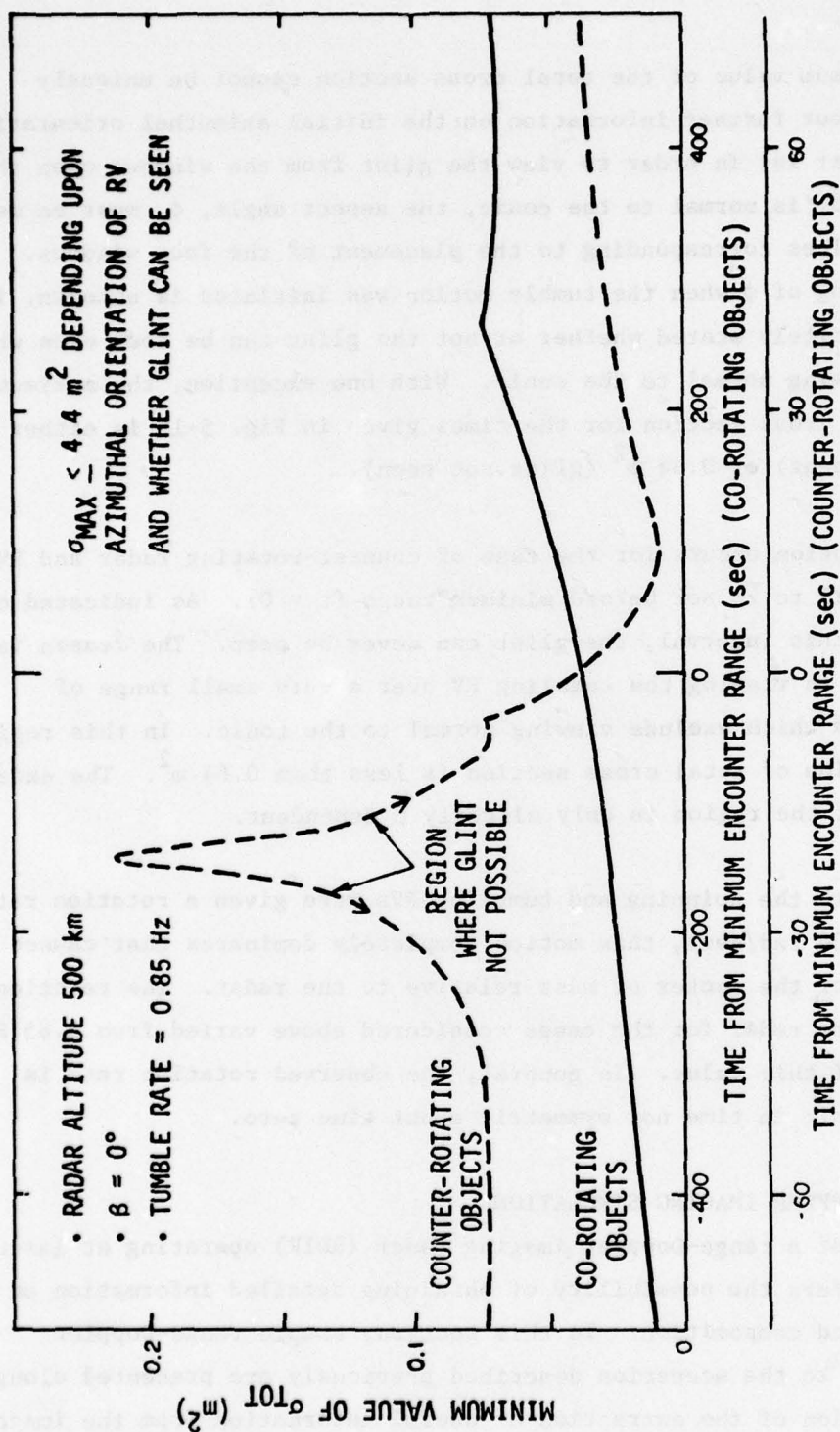


Figure 5-12. Minimum Value of Total Cross Section Observed During Radar Encounter with Tumbling RV

The maximum value of the total cross section cannot be uniquely specified without further information on the initial azimuthal orientation of the RV. That is, in order to view the glint from the windows when the aspect angle,  $\theta$ , is normal to the conic, the aspect angle,  $\phi$ , must be near one of four values corresponding to the placement of the four windows. Since the phasing of  $\phi$  when the tumble motion was initiated is unknown, it cannot be definitely stated whether or not the glint can be seen even when  $\theta$  provides viewing normal to the conic. With one exception, the maximum value of total cross section for the times given in Fig. 5-12 is either  $4.4 \text{ m}^2$  (glint seen) or  $0.64 \text{ m}^2$  (glint not seen).

The exception occurs for the case of counter-rotating radar and RV at times from 15 to 28 sec before minimum range ( $t < 0$ ). As indicated on Fig. 5-12, in this interval, the glint can never be seen. The reason is that the radar is viewing the tumbling RV over a very small range of aspect angles  $\theta$  which exclude viewing normal to the conic. In this region, the maximum value of total cross section is less than  $0.64 \text{ m}^2$ . The extent and location of the region is only slightly  $\beta$  dependent.

Since both the spinning and tumbling RVs were given a rotation rate of 0.85 Hz (5.34 rad/sec), this motion completely dominates that caused by the motion of the center of mass relative to the radar. The rotation rate seen by the radar for the cases considered above varied from 0.85 Hz to about 0.2 of this value. In general, the observed rotation rate is neither monotonic in time nor symmetric about time zero.

### 5.3 RANGE-DOPPLER IMAGING SIMULATIONS

The use of a range-Doppler imaging radar (RDIR) operating at laser frequencies offers the possibility of obtaining detailed information on target shape and composition. In this section, sample range-Doppler images related to the scenarios described previously are presented along with a discussion of the extraction of useful information from the images in the presence of noise.

The theory of RDIR for the case of a two-dimensional array of matched filters is briefly outlined in Appendix D. The computer program used to simulate the images is also discussed there. Two of the scenarios were selected to illustrate the type of output possible with RDIR: a ground-based observer and satellite target (Scenario 1, see Table 5-2), and the satellite-to-satellite case (Scenario 2a).

Some of the parameters of the hypothetical ground- and space-based RDIRs are given in Table 5-6. The former reflect state of the art component technology; the latter are estimates of capabilities in a more restrictive (space-based) operating environment.

Figure 5-13 shows a sequence of noise- and speckle-free range-Doppler images of the Meteor satellite with spin rate and aspect angles determined by the Scenario 1 encounter with parameters  $D = 0$  (direct overhead pass) and  $\Psi = 0$  (solar paddles lie in the orbital plane). Figure 5-1 illustrates the geometry. Each of the images is a grid 50 cross-range (Doppler) resolution cells wide and 50 range resolution cells high. As indicated in Table 5-6, one range resolution cell corresponds to 30 cm. The ranges, aspect angles, and cross-range resolutions are indicated below each image.

Because of the particular target parameters and resolutions associated with Fig. 5-13, the target shape as seen in the range-Doppler images bears a reasonable resemblance to its actual geometric shape as revealed in conventional angle-angle images (cf. Fig. 4-2). In general this need not be the case. A discussion of this point is included elsewhere.<sup>1</sup>

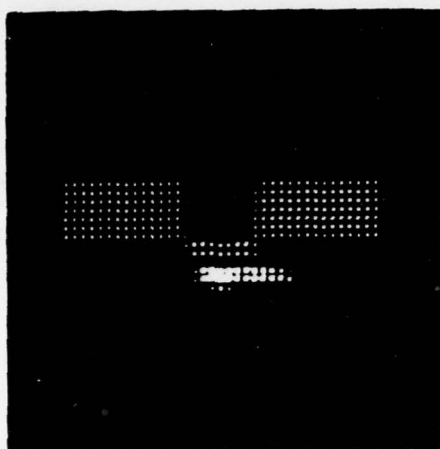
The scales below Fig. 5-5 show the relations between range, aspect angle, and elevation angle for this scenario. At a range of 1150 km, the

---

<sup>1</sup>J. Wilson, op. cit.

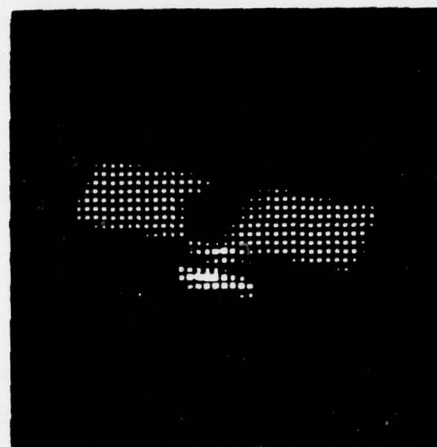
TABLE 5-6  
COMPARISON OF ASSUMED PARAMETERS FOR  
TWO RANGE-DOPPLER IMAGING RADARS

<u>Parameter</u>	<u>Ground-Based System</u>	<u>Space-Based System</u>
Wavelength	10.6 $\mu\text{m}$	10.6 $\mu\text{m}$
Pulse Width	5000 $\mu\text{sec}$	1000 $\mu\text{sec}$
Bandwidth	0.5 GHz	0.5 GHz
Range Resolution	30 cm	30 cm
Doppler Resolution	200 Hz	1000 Hz
Peak Transmitted Power	200 kW	200 kW
Pulse Repetition Rate	10 Hz	5 Hz



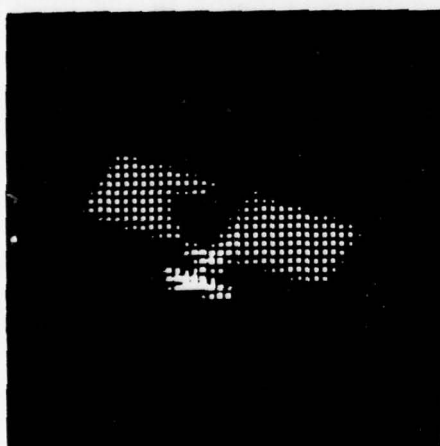
(A)

$R = 1000 \text{ km}$   
 $\theta = 180^\circ$   
 $\Delta X = 16.7 \text{ cm}$



(B)

$R = 1050 \text{ km}$   
 $\theta = 163.6^\circ$   
 $\phi = 90^\circ$   
 $\Delta X = 18.5 \text{ cm}$



(C)

$R = 1100 \text{ km}$   
 $\theta = 155.4^\circ$   
 $\phi = 90^\circ$   
 $\Delta X = 20.5 \text{ cm}$



(D)

$R = 1150 \text{ km}$   
 $\theta = 152.7^\circ$   
 $\phi = 90^\circ$   
 $\Delta X = 22.6 \text{ cm}$

Figure 5-13. Noise- and Speckle-Free Range-Doppler Images of the Meteor Satellite at Four Ranges from a Ground-Based Observer. The dynamical parameters correspond to Scenario 1.  $\Delta X$  is the cross-range (Doppler) resolution.

satellite elevation angle has decreased from 90° (overhead) to about 58°. Viewing at still smaller elevation angles is difficult because of the increased atmospheric path length. In any case, the aspect angles at which the (earth-stabilized) satellite can be viewed change more slowly at larger ranges, and the additional information available from the images is limited.

The effect of non-infinite signal-to-noise ratio (SNR) on range-Doppler images is illustrated in Fig. 5-14, where the effect of various noise levels on Fig. 5-13A is shown. As discussed in Appendix B and shown in Fig. 4-22 for conventional images, shot noise has been added to the assumed heterodyne detection system; also, speckle effects associated with scattering from a diffuse surface (Sec. 4.3) are included. The specified SNR is the ratio of the largest mean square signal amplitude (brightest pixel intensity) in Fig. 5-13A to the mean square noise amplitude. The latter is the same in each resolution element in the range-Doppler image. Clearly, even with a large maximum SNR (>100), target information can be lost through these two effects.

Before discussing the use of non-coherent averaging to enhance information extraction, some comment is made about what SNRs could be expected for Scenario 1. It is shown in Appendix B that SNR can be expressed as the ratio of target cross section to a noise-equivalent cross section through the relations

$$\frac{S}{N} = \frac{\sigma_{\text{Target}}}{\sigma_N} \quad (5-1)$$

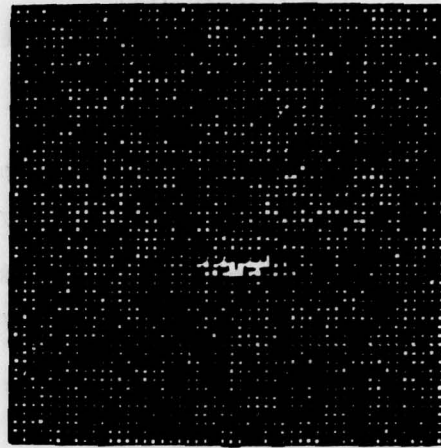
$\sigma_N$  = noise-equivalent cross section

$$= \frac{(4.05 \times 10^{-15}) \lambda R^4}{\eta D^4 \tau P_t L} \quad (5-2)$$



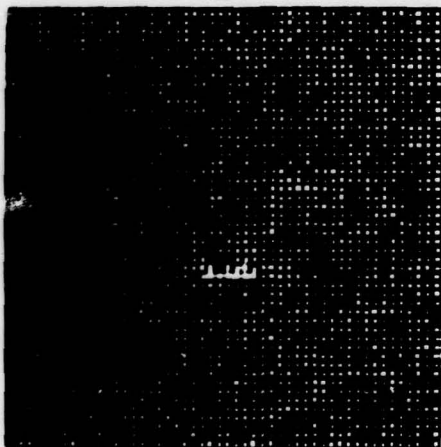
(A)

Maximum SNR = 500



(B)

Maximum SNR = 100



(C)

Maximum SNR = 50



(D)

Maximum SNR = 10

Figure 5-14. The Effect of Finite Signal-to-Noise Ratio (SNR) and Speckle on the Range-Doppler Image Corresponding to Fig. 5-13A

where  $\lambda$  = wavelength (m)  
 $R$  = range (km)  
 $\eta$  = detector efficiency  
 $D$  = receiver aperture diameter (m)  
 $\tau$  = transmitted pulse width (sec)  
 $P_t$  = peak transmitted power (kW)  
 $L$  = propagation and system loss factor

In the following, the parameters given in Table 5-6, a detector efficiency of 0.5, and an aperture diameter of 1 m are used.

The magnitude of the loss term in Eq. 5-2 is difficult to predict a priori. Using the cross section of the brightest resolved target element in Fig. 5-13A ( $0.119 \text{ m}^2$ ) and the above equations, Fig. 5-15 shows the maximum SNR vs. loss factor for the minimum range (1000-km) case. From the figure, a loss factor of -41.4 dB produces a maximum SNR of 100. This was chosen as the operating point for the system.

With the loss specified, the change in maximum SNR during the encounter is determined. Figure 5-16 shows SNR vs. the same Scenario 1 parameters used in Fig. 5-5. The actual falloff of the SNR would be faster than shown because of increasing loss at small elevation angles (increased atmospheric path length).

The extraction of useful information from range-Doppler images can be examined in two stages: first, the presence and extent of the target must be ascertained above the noise; second, an assessment can be made of the relative brightness (contrast ratio) between different parts of the target. Since the statistics of the observed image intensity are known (see Appendix B), the probabilities corresponding to detection and contrast discernment in the presence of noise can be calculated.

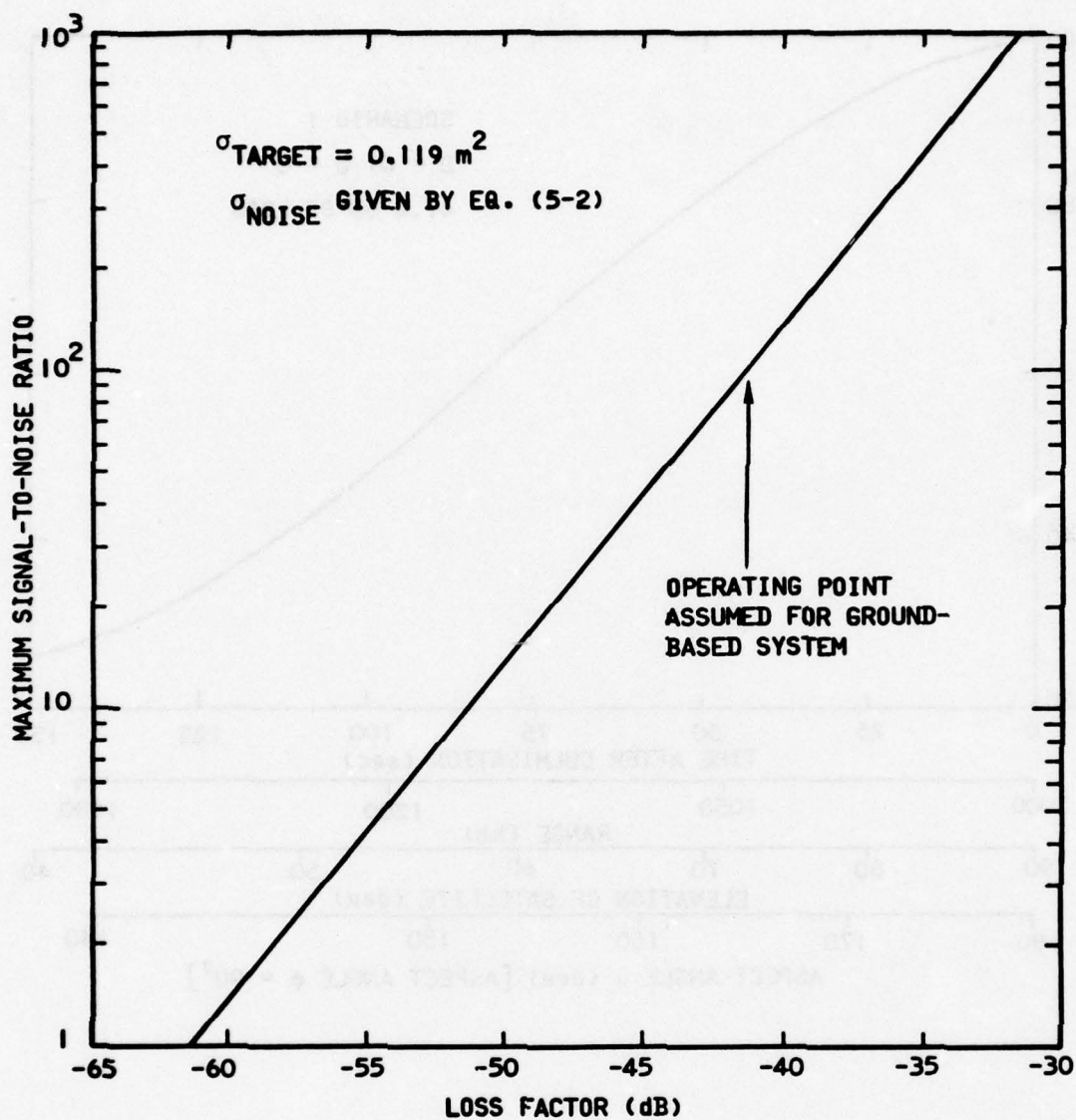


Figure 5-15. Effect of System and Transmission Losses on  
 Maximum Signal-to-Noise Ratio

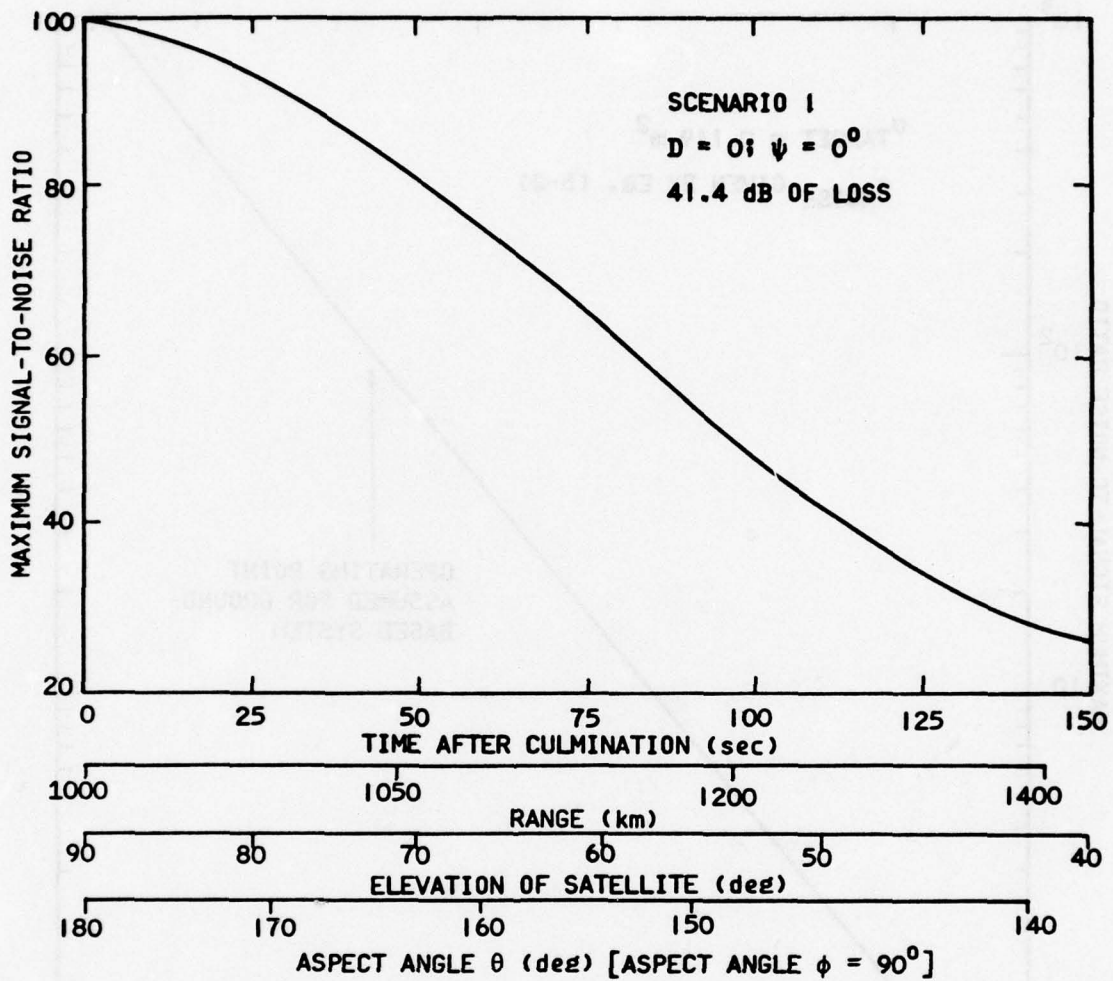


Figure 5-16. Behavior of Maximum Signal-to-Noise Ratio for Scenario 1

Figure 5-17 shows the number of range-Doppler images which must be non-coherently averaged (in the manner demonstrated in Sec. 4.3 for Doppler-resolved cross sections) to insure a desired probability of detection for the given SNR. For SNRs greater than about 10, it is seen that a single sample is sufficient for detection.

An alternative criterion<sup>1</sup> for detection of signal above noise is illustrated in Fig. 5-18. The probability density functions (PDF) of the image intensity in the cases of noise alone and signal plus noise have the same shape but different means and standard deviations. As more samples are averaged, the PDFs become more sharply peaked (decreased standard deviations) about their respective mean values. A target is said to be reliably detected above the noise when sufficient samples are averaged so that the separation of the means of the two PDFs is equal to or greater than the sum of the standard deviations of the two distributions. The number of samples required to meet this criterion is also shown in Fig. 5-17 and is seen to correspond to a probability of detection of between 0.9 and 0.95.

As a practical matter, the target rotation rate imposes some limitations on the number of samples which can be averaged. Figure 5-19 shows the maximum number of samples which can be obtained before a point 3 m from the target rotation axis moves from one range or Doppler resolution cell to another. The distance 3 m corresponds to the maximum extent of the satellite used here (Fig. 4-1). For slower rotation rates, the range resolution cell size limits the sample number, while for higher rates the Doppler resolution cell size is most important. Scenario 1 involves rotation rates less than 7 mrad/sec (Table 5-2); consequently, averaging of 75 samples or more is possible.

---

<sup>1</sup>J. Wilson, op. cit.

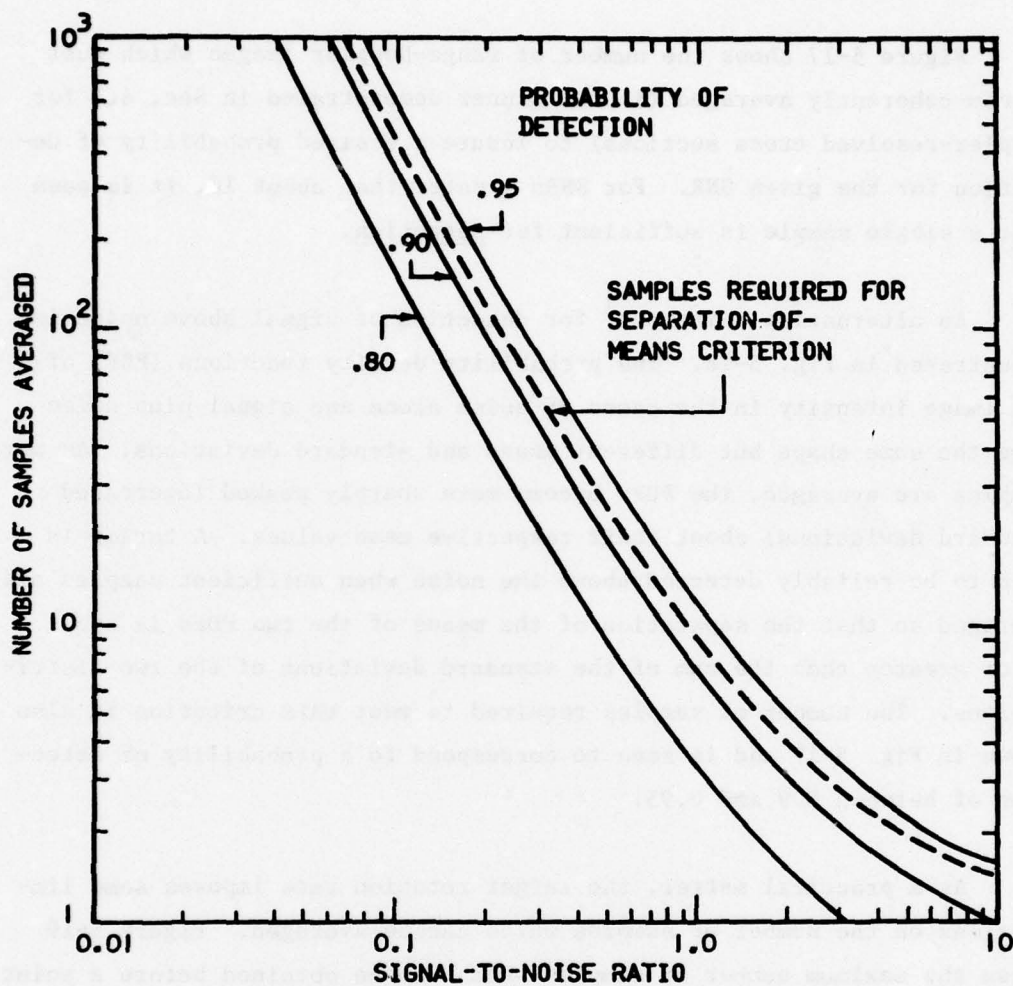


Figure 5-17. Number of Range-Doppler Images to Be Averaged vs. Probability of Detection and Signal-to-Noise Ratio

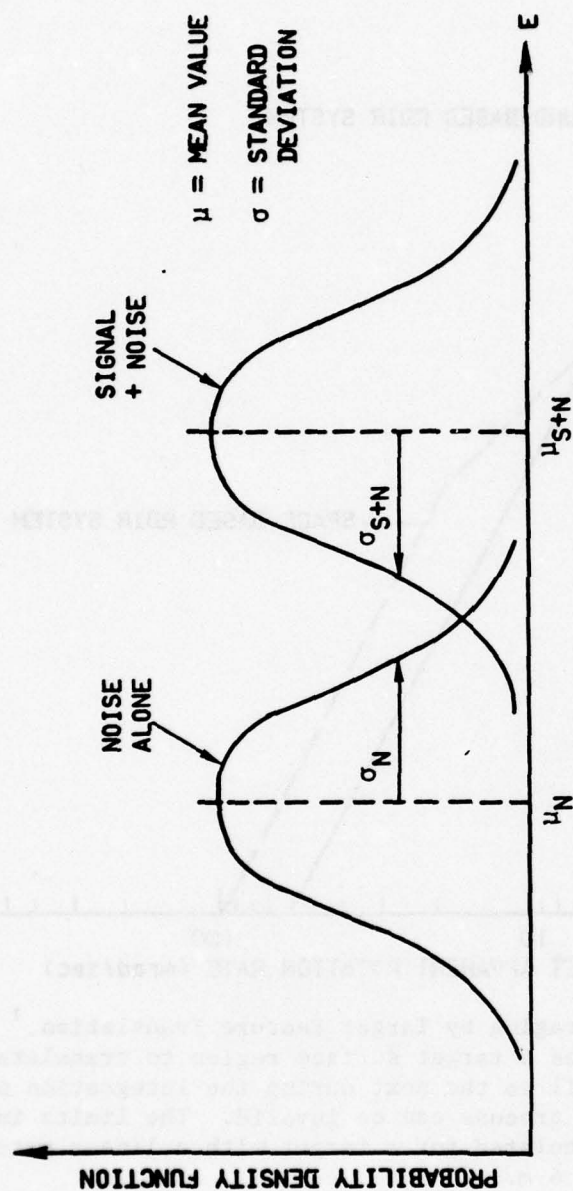


Figure 5-18. "Separation of Means" Criterion for Detection of Signal Above Noise. The criterion of detection of signal above noise (see text) is that  $\mu_{S+N} - \mu_N \geq \sigma_{S+N} + \sigma_N$ .

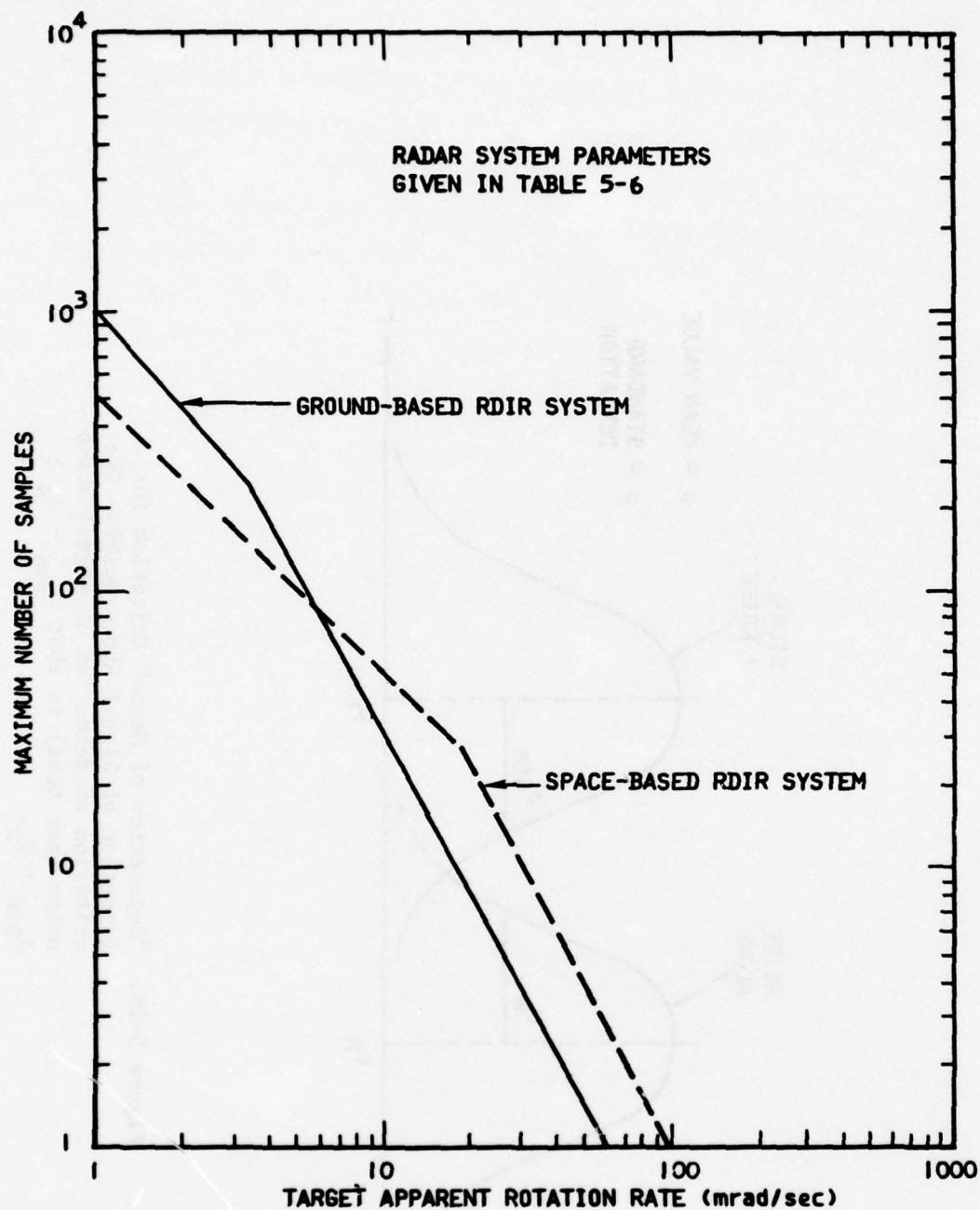


Figure 5-19. Limits on Averaging by Target Feature Translation.<sup>1</sup> If target rotation causes a target surface region to translate from one resolution cell to the next during the integration period, the averaging process can be invalid. The limits indicated above are calculated for a target with a linear extent of approximately 6 m.

<sup>1</sup>J. W. Wilson, op. cit.

After sufficient range-Doppler images have been averaged to insure a high probability of detecting the target shape, the discernment of the relative intensities of different parts of the target may be addressed. Contrast ratio as used here is defined as the ratio of that part of the intensity of two resolution cells due to target signal alone (i.e., after the noise has been removed). Figure 5-20 shows the probability of concluding that one target image element is brighter (or dimmer) than another vs. the SNR of the dimmer element. The assumption used in calculating the data for the figure was that sufficient image samples have been averaged to make the probability of detecting the dimmer element 0.9 (see Fig. 5-17). Consequently, as the SNR of the dimmer element decreases, a sharp increase occurs in the number of image samples averaged. This increased averaging is large enough to allow smaller intensity ratios to be discerned.

To illustrate the effect of image-enhancement by non-coherent averaging, Fig. 5-21 shows a sequence of images corresponding to the geometry and dynamics of Fig. 5-13A with a maximum SNR of 100. For reference, Fig. 5-21A shows a noise- and speckle-free numerical-scale line-printer image of the satellite under the same conditions. In decreasing order the 11-level numerical scale uses the characters ".", "9", . . . , "0", and "\*". The separation between the levels in Fig. 5-21 is 3 dB. The central parts of the two solar paddles happen to appear in adjacent (instead of the same) levels of intensity because of the manner in which the program decomposed the solar paddles into subareas and assigned the boundary between printer levels.

Since the main parts of the solar paddles are 15 and 18 dB dimmer (5 or 6 levels below maximum in Fig. 5-21A) than the brightest image element, the SNR of this region of the target is only 1.5 to 3. Figure 5-17 shows that about 5 samples should be averaged to allow reliable detection of the solar paddles. Indeed, the improvement between Figs. 5-21B and 5-21C is dramatic. Averaging still more image samples further refines

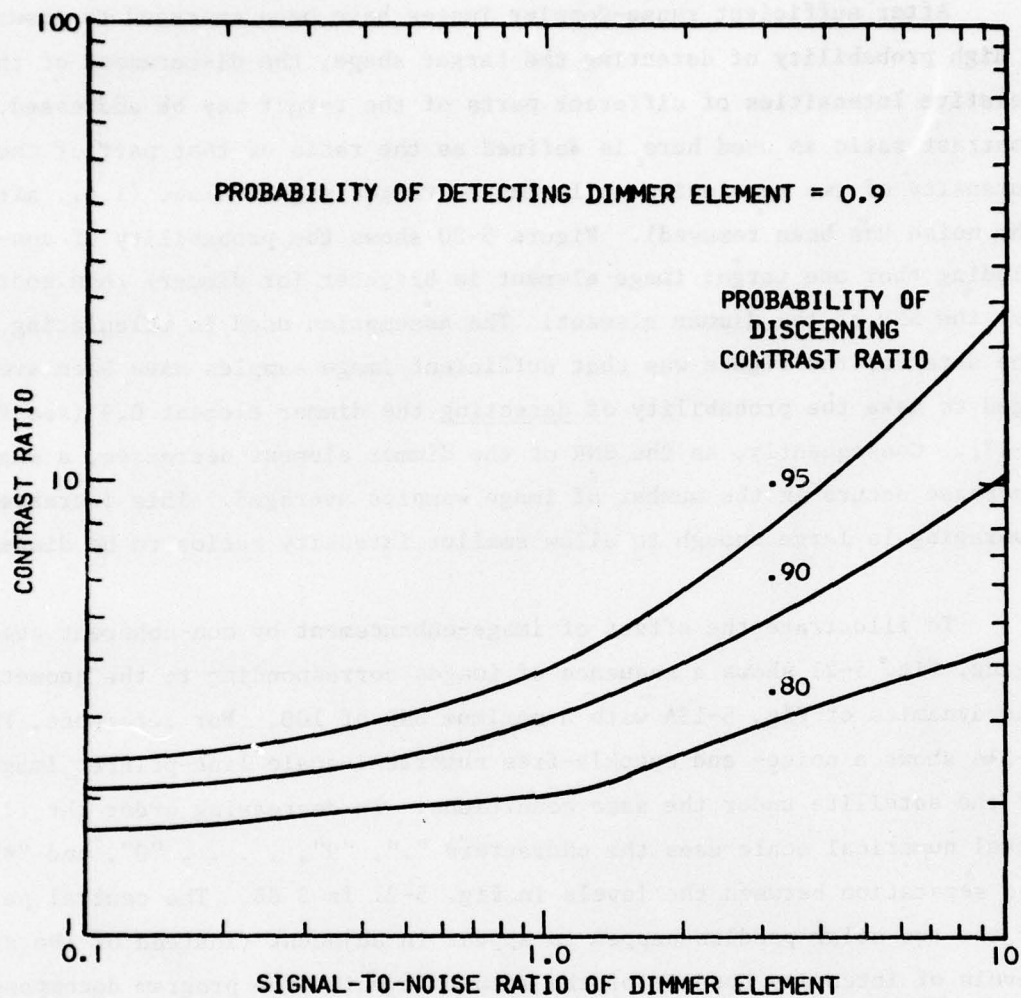
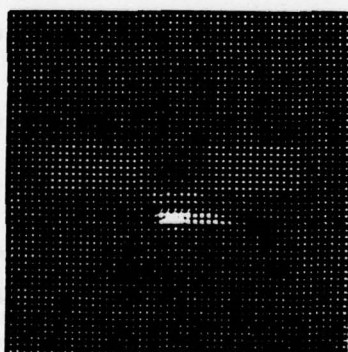


Figure 5-20. Contrast Ratio of Two Image Elements vs. Probability of Discerning Contrast and Signal-to-Noise Ratio of Dimmer Element

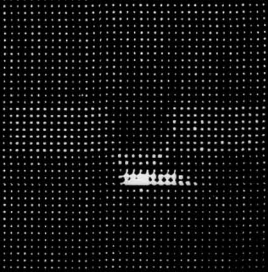
(B)

(D)

10 Samples



(E)



(F)

100 Samples

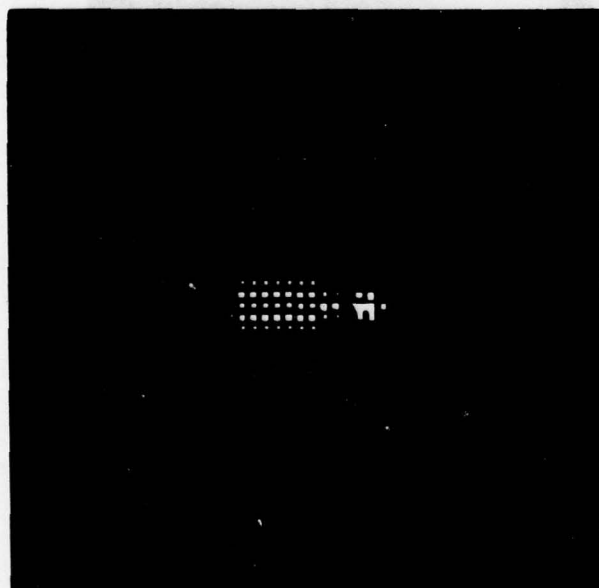
105

the paddle outline. About 100 averaged samples reveal a sharp edge on the paddles. (The edges are 27 dB dimmer than the brightest point, causing their SNR to be 0.2; 100 samples affords a probability of detection of 0.9.)

Since the contrast ratio between the solar paddles and the brightest area of the target is so large (30 to 60), the probability of discerning this difference is virtually 1. With some knowledge of the bidirectional reflectance of the satellite materials, bounds could be placed on the orientation of the paddles relative to the body of the satellite.

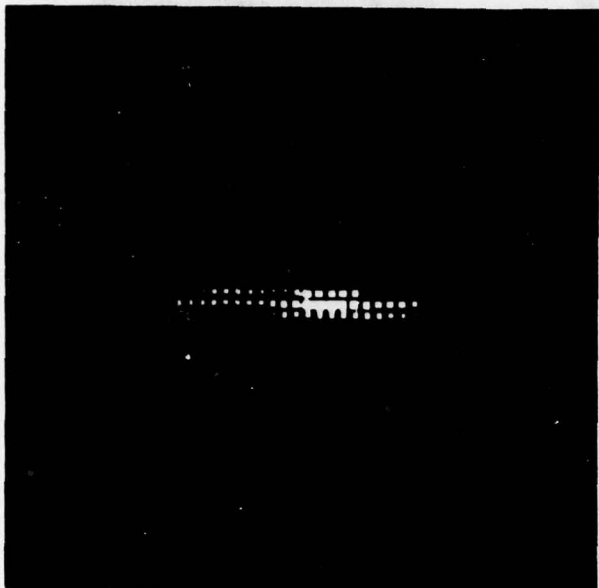
Scenario 2a is the satellite-satellite encounter (Fig. 5-2). Figure 5-22 shows two range-Doppler images corresponding to the target and radar satellites co-rotating in the same plane. The minimum range is 500 km. Because the Doppler resolution of the space-borne radar is a factor of 5 less than that of the ground-based system and the apparent satellite rotation rate is also reduced by a factor of 2 or more from Scenario 1, the entire target fits into about three cross-range resolution cells. The range resolution, however, is the same as for Fig. 5-13. Consequently, the target has been collapsed into essentially one dimension.

With a specified radar system, the cross-range resolution can be improved only if the apparent target rotation rate increases. This is the case when target and radar satellites are counter-rotating (cf. Table 5-3). Range-Doppler images for this case are shown in Fig. 5-23. Comparison of Figs. 5-13A-C with Figs. 5-23A-C shows virtually the same images at corresponding aspect angles. It is important to realize, however, that this similarity is due to the coincidental match in cross-range resolution. In general, the satellite-satellite encounter would be expected to yield range-Doppler images somewhere between those of Figs. 5-22 and 5-23.



(A)

$R = 500 \text{ km}$   
 $\theta = 180^\circ$   
 $\Delta X = 2 \text{ m}$



(B)

$R = 1000 \text{ km}$   
 $\theta = 123.4^\circ$   
 $\phi = -90^\circ$   
 $\Delta X = 3.7 \text{ m}$

Figure 5-22. Noise- and Speckle-Free Range-Doppler Images of the Meteor Satellite at Two Ranges from a Satellite-Borne Radar. The dynamical parameters were determined by Scenario 2a when target and observer are co-rotating.  $\Delta X$  is the cross-range (Doppler) resolution.

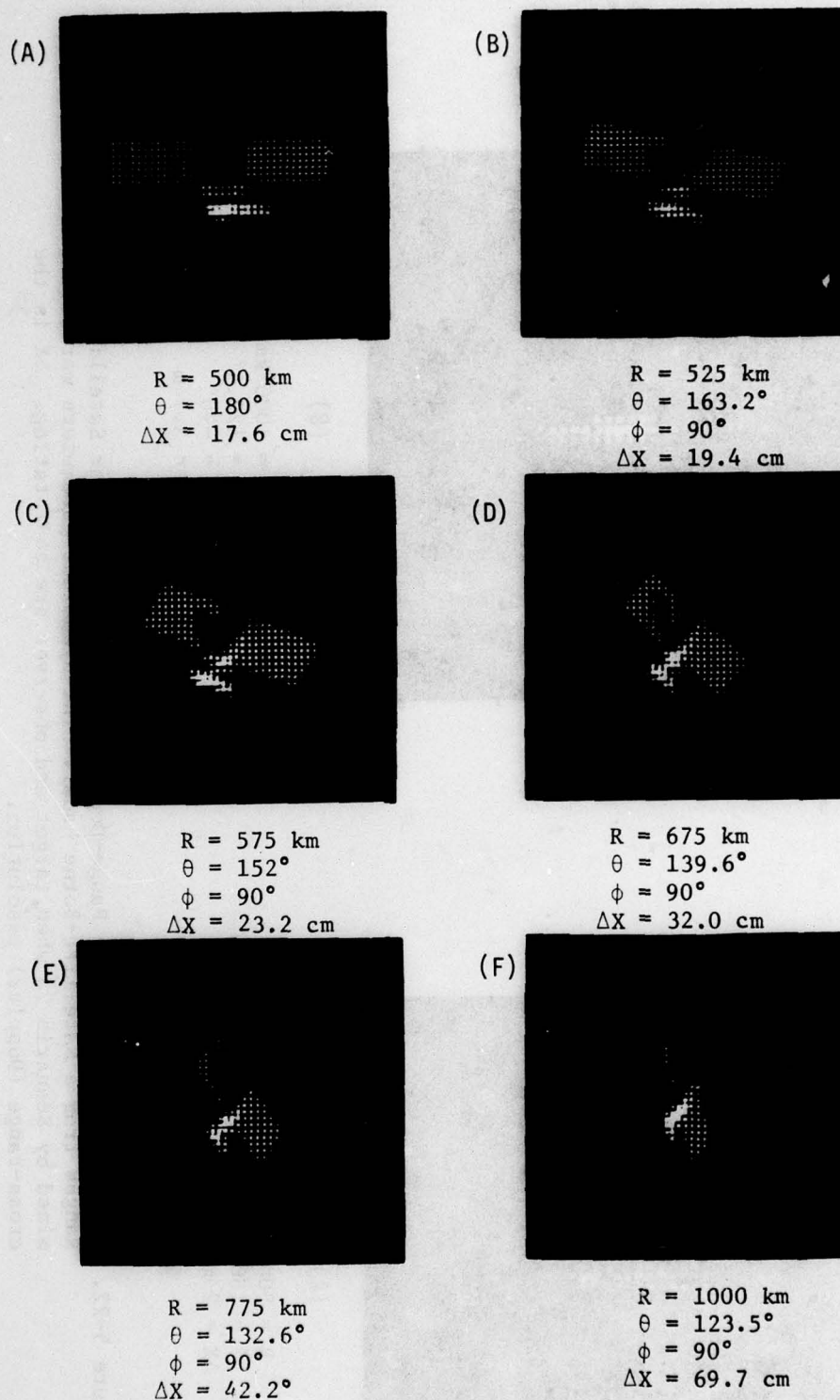


Figure 5-23. Noise- and Speckle-Free Range-Doppler Images of the Meteor Satellite at 6 Ranges from a Satellite-Borne Radar. The dynamical parameters were determined by Scenario 2a when target and observer are counter-rotating.  $\Delta X$  is the cross-range (Doppler) resolution.

It should also be noted that while higher apparent rotation rates are desirable from an improved cross-range resolution standpoint, the higher rates limit the number of image samples which can be averaged, as indicated in Fig. 5-19. A rotation rate of 30 mrad/sec (corresponding to Fig. 5-23A) limits sample averaging to 10 samples. This in turn restricts the allowable SNR to 1 or greater. Thus, not as much detailed shape information can be deduced from the space-borne system.

## APPENDIX A

### MATHEMATICAL FORMULATION OF SPECKLE SIMULATION

This appendix presents the basic mathematical expressions used in the modeling of speckle and blurring effects as described in Sec. 2.1. In the interests of brevity, the various intermediate steps have not been detailed.

In terms of the coordinate systems shown in Fig. 2-1, the electric field in the target plane is treated as due to a collection of  $n$  point scatterers located at  $(x_i, y_i)$  for  $n$  large:

$$E_{\text{target}}(x, y) = \sum_{i=1}^n a_i(x_i, y_i) \delta(x - x_i) \delta(y - y_i) e^{j(\theta_i + \omega_i t)} \quad (\text{A-1})$$

where  $a_i$  = a Rayleigh-distributed random variable with  $\overline{a_i^2} = \sigma_i$   
 $\sigma_i$  = the cross section of the  $i$ th scatterer  
 $\theta_i$  = a uniformly distributed random variable over  $(0, 2\pi)$   
 $\omega_i$  = the Doppler shift introduced by the target rotation

The circular aperture is located a distance  $R$  away from the target plane and has the (ideal) pupil function:

$$P(x_1, y_1) = \begin{cases} 1, & x_1^2 + y_1^2 \leq D^2/4 \\ 0, & \text{elsewhere} \end{cases} \quad (\text{A-2})$$

where  $D$  is the aperture diameter.

The response function of the optical system is given by the Fourier transform of the pupil function in spatial frequencies:<sup>1</sup>

<sup>1</sup>J. W. Goodman, Introduction to Fourier Optics, McGraw Hill Book Company, 1968.

$$h(x, y) = c \iint_{-\infty}^{\infty} P(\lambda f x_1, \lambda f y_1) \exp [-2\pi j (x x_1 + y y_1)] dx_1 dy_1 \quad (A-3)$$

where  $c$  = a complex constant

$f$  = the optical system focal length

$\lambda$  = the wavelength of interest

Combining Eqs. A-2 and A-3,

$$h(x, y) = c' \frac{J_1\left(\frac{\pi D r}{\lambda f}\right)}{\left(\frac{\pi D r}{\lambda f}\right)} \quad (A-4)$$

where  $r = \sqrt{x^2 + y^2}$ . Finally, the system response function can be used to calculate the electric field in the image plane by the convolution (valid in the far-field region)

$$E(x_2, y_2) = \iint h(x_2 - x, y_2 - y) E'(x, y) dx dy \quad (A-5)$$

where  $E'(x, y) = \frac{\lambda^2 f^2}{2M^2} E\left(\frac{x}{M}, \frac{y}{M}\right)$

$M$  = system magnification =  $f/R$

$E$  is given in Eq. A-1

To within an overall numerical constant and for unit magnification, the result is

$$E(x_2, y_2) = C'' \sum_{i=1}^n a_i(x_i, y_i) \exp [j(\theta_i + \omega_i t)] \frac{J_1\left(\frac{\pi D r}{\lambda R}\right)}{\left(\frac{\pi D r}{\lambda R}\right)} \quad (A-6)$$

where  $r = \sqrt{(x_2 - x_i)^2 + (y_2 - y_i)^2}$ .

The magnitude squared of the electric field in Eq. A-6 gives the familiar speckle pattern of radiation reflected from a rough surface with the added feature of aperture blurring.

From the argument of the Bessel function in Eq. A-6, the resolution of the system is  $1.22\lambda R/D$ . The effect of aperture blurring without speckle effects may be obtained by rewriting Eq. A-5 as

$$|E(x_2, y_2)|^2 = \iint |h(x_2 - x, y_2 - y)|^2 |E'(x, y)|^2 dx dy \quad (A-7)$$

where  $h$  is given by Eq. A-4, and

$$|E'(x, y)|^2 \propto |E_{\text{Target}}|^2$$

## APPENDIX B

### EFFECT OF NOISE ON RECEIVED SIGNAL

A block diagram of the laser receiver system is shown in Fig. B-1. The electric field,  $E$ , entering the system is a return signal from a diffusely reflecting surface (target). It is known that this field has a Rayleigh-distributed amplitude (with mean square value proportional to the target cross section) and uniformly distributed phase. That is,

$$E = Ae^{j\phi} \quad (B-1)$$

where the probability density functions of  $A$  and  $\phi$  are given by,

$$P_r(A) = \frac{2A}{\overline{A^2}} \exp(-A^2/\overline{A^2}) \quad 0 \leq A < \infty \quad (B-2)$$

$$P_r(\phi) = \begin{cases} \frac{1}{2\pi} & 0 \leq \phi < 2\pi \\ 0 & \text{elsewhere} \end{cases} \quad (B-3)$$

$$\overline{A^2} = \text{mean square value of } A \propto \sigma_{\text{target}} = \text{target cross section} \quad (B-4)$$

For the heterodyne receiver system, the (complex) current,  $i_p$ , produced by the photodetector and due to the received signal can be written

$$i_p = |i_p| e^{j\phi_p} \quad (B-5)$$

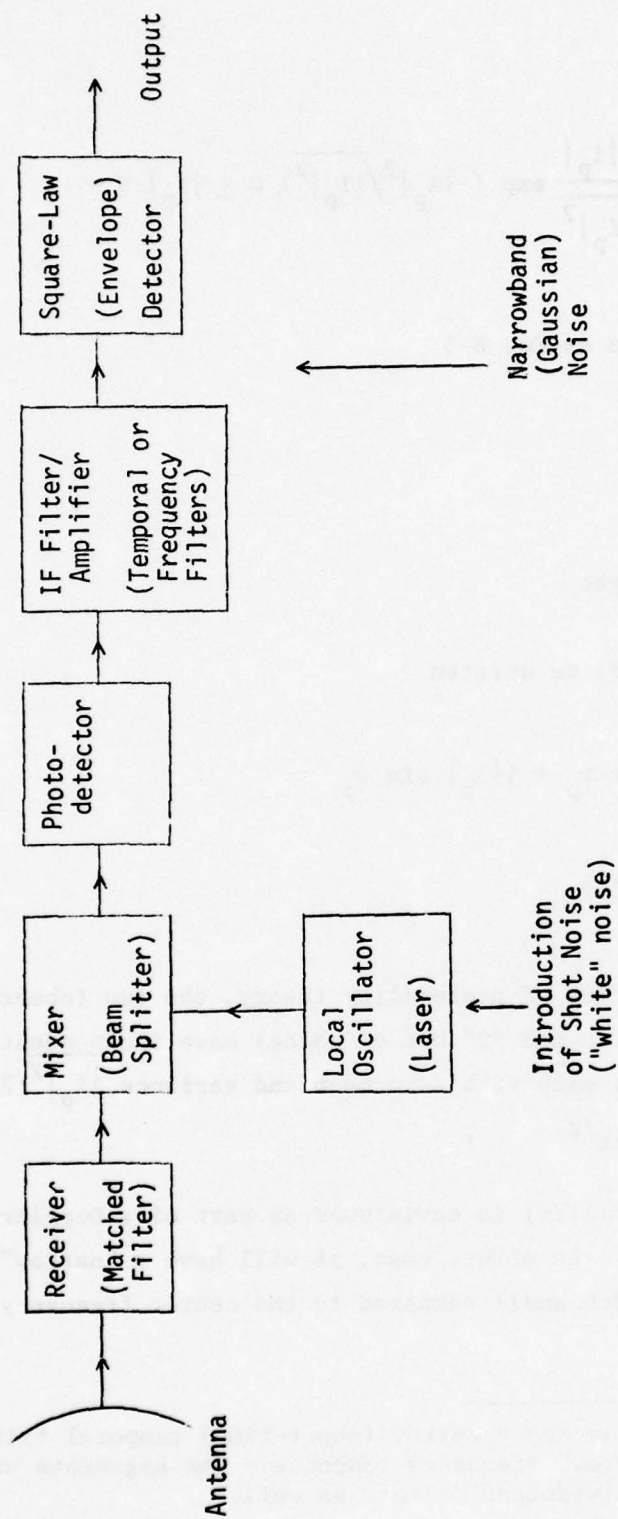


Figure B-1. Heterodyne Laser Receiver (Through IF Detector Stage)

in which case

$$P_r(|i_p|) = \frac{2|i_p|}{|i_p|^2} \exp(-|i_p|^2/\overline{|i_p|^2}), 0 \leq |i_p| < \infty \quad (B-6)$$

$$P_r(\phi_p) = \text{same as Eq. B-3} \quad (B-7)$$

and

$$\overline{|i_p|^2} \propto \sigma_{\text{target}} \quad (B-8)$$

Note that Eq. B-5 may also be written

$$\begin{aligned} i_p &= |i_p| \cos \phi_p + j|i_p| \sin \phi_p \\ &\equiv i_{p1} + ji_{p2} \end{aligned} \quad (B-9)$$

By a standard transformation of probability theory, the two (observable) currents  $i_{p1}$  and  $i_{p2}$  (which are 90° out of phase) have independent Gaussian probability distributions each with zero mean and variance  $|i_p|^2/2$ , which is proportional to  $\sigma_{\text{target}}/2$ .

The IF amplifier (filter) is envisioned as part of a Doppler or range-resolving receiver. In either case, it will have a "narrow" frequency passband<sup>1</sup> (bandwidth small compared to the center frequency of the

<sup>1</sup>The range-resolving system has a narrow (short-time) temporal filter which in turn has a "narrow" frequency response. The arguments which follow can be applied to wideband filters as well.

passband). The effect of this filter on the current given in Eq. B-9 is found by Fourier decomposing  $i_{p1}$  and  $i_{p2}$  and using the result<sup>1</sup> that the Fourier coefficients are themselves independent Gaussian-distributed random variables. The only effect of the filter is to restrict the range of the frequency components of  $i_p$ ; the statistics of  $i_{p1}$  and  $i_{p2}$  are unchanged.

The square-law detector produces an output current,  $i_D$ , proportional to  $|i_p|^2$ . Since  $|i_p|^2$  is Rayleigh distributed,<sup>2</sup>  $i_D$  is exponentially distributed:

$$i_D \propto |i_p|^2 \quad (\text{B-10})$$

where

$$P_r(i_D) = \frac{\exp(-i_D/\bar{i}_D)}{\bar{i}_D} \quad (\text{B-11})$$

and

$$\bar{i}_D \propto \overline{|i_p|^2} \propto \sigma_{\text{target}}^2 \quad (\text{B-12})$$

By renormalizing  $i_D$ , the output of the square-law detector may be described by the quantity  $I$  (units  $\text{W/m}^2$ ), where

$$P_r(I) = \frac{\exp(-I/\sigma_{\text{target}}^2)}{\sigma_{\text{target}}^2} \quad (\text{B-13})$$

<sup>1</sup>Wilbur Davenport and William Root, An Introduction to the Theory of Random Signals and Noise, McGraw-Hill Book Co., 1958, Sec. 6-3.

<sup>2</sup>M. C. Teich, "Coherent Detection in the Infrared," in Semiconductors and Semimetals, Vol. 5, Infrared Detectors, Academic Press, 1970 p. 398.

Now the effect of noise will be added to the above ideal system response. For the heterodyne receiver system, it is assumed that the local oscillator power level is made large enough so that only the shot noise of the local oscillator need be considered.<sup>1</sup> The shot noise (as a function of time) can be described as a Gaussian random process<sup>2,3</sup> (the limiting form of a Poisson distribution). Its frequency spectrum is "white" (i.e., uniformly distributed in frequency).

The effect of the IF amplifier (narrow-frequency filter; no DC component) on the shot noise is to produce a Gaussian-distributed quantity with zero mean.<sup>4</sup> The Fourier coefficients of the filtered shot noise are also Gaussian-distributed random variables with zero mean. Unfortunately, since the shot noise is a non-periodic phenomenon, those coefficients are correlated random variables. However, it has been shown that as the time interval over which the Fourier transform is valid approaches infinity, the correlation between the coefficients approaches zero.<sup>5</sup>

Manipulation of the Fourier expansion of the filtered shot noise shows that it can be expressed as a sum of two current, 90° out of phase, each of which has a Gaussian distribution with zero mean.<sup>6,7</sup> That is, the shot noise entering the square-law detector has the same form as Eq. B-9. Finally, since shot noise is an additive effect,<sup>8</sup> the probability distribution of the output current of the square-law detector has the same form as Eq. B-11 with mean value ( $\bar{i}_D$ ) increased by the mean square value of the filtered shot noise (see Eq. B-12). Again, renormalizing the output current Eq. B-13 in the presence of noise becomes

<sup>1</sup> William Pratt, Laser Communications Systems, Wiley & Sons, Inc., 1969, p. 189.

<sup>2</sup> Davenport and Root, op. cit., pp. 126, 127.

<sup>3</sup> Athanasios Papoulis, Probability, Random Variables, and Stochastic Processes, McGraw-Hill Book Co., 1965, Sec. 16-5.

<sup>4</sup> Pratt, op. cit., p. 252.

<sup>5</sup> Davenport and Root, op. cit., Sec. 6-4.

<sup>6</sup> Ibid, Sec. 8-5.

<sup>7</sup> A. Bruce Carlson, Communications Systems, McGraw-Hill Book Co., Section 4-7.

<sup>8</sup> John Hancock and Paul Wintz, Signal Detection Theory, McGraw-Hill Book Co., 1966, p. 6.

$$P_r(I) = \frac{\exp [-I/(\sigma_{\text{target}} + \sigma_n)]}{(\sigma_{\text{target}} + \sigma_n)} \quad (\text{B-14})$$

where  $I$  is proportional to the total output current (target + noise signals) of the square-law detector, and  $\sigma_n$  will be called the "noise equivalent cross section."

It remains to give some "physical" interpretation to  $\sigma_n$ . For a radar system, the conventional definition of the output signal-to-noise ratio (measured at the output of the envelope detector) is<sup>1</sup>

$$\frac{S}{N} = \frac{|i_p|^2}{|i_s|^2} = \frac{\sigma_{\text{target}}}{\sigma_n} \quad (\text{B-15})$$

An alternative expression for  $S/N$  in terms of the energy,  $E_r$ , received by the antenna, the power,  $P_r$ , received from a pulse of length  $\tau$ , the detector efficiency  $\eta$ , and the carrier frequency  $f$  is<sup>2</sup>

$$\frac{S}{N} = \frac{1}{2} \frac{\eta E_r}{hf} = \frac{\eta P_r \tau}{2hf} \quad (\text{B-16})$$

Combining Eqs. B-15, B-16 and the radar equation,

$$P_r = \frac{\pi P_t D^4 \sigma_{\text{target}} L}{64(\lambda R^2)^2}$$

<sup>1</sup>Merrill Skolnik, Introduction to Radar Systems, McGraw-Hill Book Co., 1962, pp. 29-33

<sup>2</sup>Pratt, op. cit., p. 189.

where  $P_t$  = transmitted power  
 $R$  = target-radar range  
 $D$  = receiver/transmitter aperture diameter  
 $L$  = system and propagation loss factor

yields

$$\sigma_n = \frac{(64\lambda hc)R^4}{\pi\eta D^4 \tau P_t L} \quad (B-18)$$

Equation B-15 interprets  $\sigma_n$  as that target cross section producing an SNR value of 1; Eq. B-18 relates  $\sigma_n$  to the parameters of the radar system viewing a target at distance  $R$ .

## APPENDIX C ATMOSPHERICS

The refractive index spectrum hypothesized by Tatarski<sup>1</sup> has the following form:

$$\Phi_n(\kappa) = 0.033 C_n^2 \kappa^{11/3} \exp(-\kappa^2 / \kappa_m^2) \quad (C-1)$$

where  $C_n^2$  = index-of-refraction structure function

$\kappa$  = spatial frequency

$\kappa_m = 5.92/\ell_0$ , in which  $\ell_0$  = inner scale of turbulence

In the limit as  $\kappa$  approaches 0, this spectrum becomes indeterminate. Strohbehn<sup>2</sup> added an additional term that causes the spectrum to saturate for values of  $\kappa < 1/L_0$ , where  $L_0$  is the outer scale of turbulence. This modified spectrum has the form

$$\Phi_n^1(\kappa) = 0.033 C_n^2 [\kappa^2 + 4\pi^2 L_0^{-2}]^{-11/6} \exp(-\kappa^2 / \kappa_m^2) \quad (C-2)$$

As demonstrated by Taylor,<sup>3</sup> the variance of the index of refraction variations is obtained by the following equation:

$$\sigma_n^2 = \pi^2 k^2 d \int_0^\infty \Phi_n(\kappa) \kappa \, d\kappa \quad (C-3)$$

where  $d$  = width of the phase screen.

This integral is tabulated, from which we obtain for the condition  $L_0 \gg \ell_0$ ,

$$\sigma_n^2 = 0.0087 k^2 d C_n^2 L_0^{5/3} \quad (C-4)$$

<sup>1</sup>V. I. Tatarski, The Effects of the Turbulent Atmosphere on Wave Propagation, Report TT-68-50464, U.S. National Technical Information Service, Springfield, Virginia, p. 76.

<sup>2</sup>J. W. Strohbehn, *Proc. IEEE*, 56, p. 1301 (1968).

<sup>3</sup>L. S. Taylor et al., *JOSA*, 65, p. 78 (1975).

## APPENDIX D

### RANGE-DOPPLER IMAGING RADAR SYSTEM

The basic theory of the range-Doppler imaging radar (RDIR) is expressed in the language of ambiguity functions, matched filter receivers, and pulse compression systems. Numerous references are available of which a few are quoted.<sup>1,2,3</sup> The material below was extracted from two recent reports.<sup>4,5</sup>

In terms of the received (input) signal,  $x(t)$ , entering the radar antenna and the receiver system response function,  $h(t)$ , the output signal is the usual convolution

$$y(\tau) = \int_{-\infty}^{\infty} x(t')h(\tau - t') dt' \quad (D-1)$$

In the case of a matched filter receiver (for unity gain and ignoring any time delays in filter response required by causality),  $h(t) = x(-t)$ . Finally, when the input signal has been Doppler shifted in frequency by  $\nu$ , the output signal becomes

$$y(\tau, \nu) = \int_{-\infty}^{\infty} x(t')x(t' - \tau)e^{-j2\pi\nu t'} dt' \quad (D-2)$$

---

<sup>1</sup>A. W. Rihaczek, Principles of High-Resolution Radar, McGraw-Hill Book Co., 1969.

<sup>2</sup>C. E. Cook and M. Bernfeld, Radar Signals An Introduction to Theory and Applications, Academic Press, 1967.

<sup>3</sup>M. I. Skolnik, op. cit.

<sup>4</sup>J. W. Wilson, op. cit.

<sup>5</sup>G. F. Gorman and G. F. Gurski, Space Applications Study Support: Laser and Millimeter Range-Doppler Imaging of RVs, General Research Corp., Report IP-02-W, May 1976.

In Eq. D-2,  $|y(\tau, \nu)|$  is called the waveform ambiguity function<sup>1</sup> (WAF) and is usually symbolized by  $\chi(\tau, \nu)$ .  $\tau$  is called the delay coordinate and is related to the system range resolution.

The properties of  $\chi$  are discussed in the references. The utility of the ambiguity function lies in its succinct description of system Doppler- and range-resolution capabilities for a specified transmitted waveform. The RDIR receiver can be envisioned as a two-dimensional array of filters, with the filters spaced evenly in both delay and Doppler. The waveform would be chosen such that the WAF has a high value in a small area around the origin and a very low value in a considerably larger area surrounding the central lobe. The result would be that each filter would respond only to those targets which lie in the corresponding region in delay-Doppler. The ensemble of filter responses could then be considered an image of the target distribution in the general sense.

Meaningful two-dimensional range-Doppler (R/D) images of rotating bodies are made possible by the fact that for a given rigid body with specified body dynamics, the coordinate transformation from the range and cross-range<sup>2</sup> directions into delay-Doppler space is linear and spatially invariant. That is, the range coordinate of a given point on the target is linearly related to the delay as measured by the system. Likewise, the cross-range coordinate is linearly related to the measured Doppler shift if the body is rigid. Quantitatively, the delay  $\tau$  associated with a given point on the target is related to the relative range of the point  $\Delta z$  by

$$\tau = \frac{2}{c}\Delta z \quad (D-3)$$

<sup>1</sup>Other definitions of the ambiguity function are  $|y(\tau, \nu)|^2$ , or the expressions obtained by changing the sign of  $\tau$ .

<sup>2</sup>The term "cross-range" direction is used to denote the direction perpendicular to both the observation direction and instantaneous spin axis of the target.

Since the origin of the time (range) coordinate is irrelevant, it is conceptually convenient to choose it centered in the target space; hence the notation " $\Delta z$ " rather than " $z$ ." In a similar manner, the relative Doppler shift  $\nu$  of the signal received from a point on the target can be related to the cross-range location of the point. The Doppler shift is given by:

$$\nu = \frac{V}{c} \nu_0 \quad (D-4)$$

where  $V$  is the velocity component along the line of sight. On a rigid body rotating at angular frequency  $\omega_0$ , Eq. D-4 becomes

$$\nu = 2\omega' \Delta x \nu_0 / c = (2\omega_0 \sin \phi / \lambda_0) \Delta x \quad (D-5)$$

where  $\Delta x$  is the distance of the point from the instantaneous spin axis of the body in the cross-range direction,  $\omega'$  is the magnitude of the projection of the spin vector onto the plane perpendicular to the observation vector line of sight (VLOS), and  $\phi$  is the angle between the spin vector and VLOS.

Equation D-5 implicitly contains the assumption that reflection from a target moving at constant range rate serves merely to shift the spectrum of the signal by an amount  $\nu$ . If treated rigorously, however, the effect is somewhat more involved: the Doppler effect is only an approximation that is useful in many cases.

For the present, it will be assumed that the system is appropriately modified (in particular, that the matched filter is properly chosen) such that the effect of target rotation is the only relevant target motion, and that the effect of that motion can be considered to be the simple Doppler shift as indicated in Eq. D-5.

The following discussion refers to the coordinate system shown in Fig. D-1. The  $z$ -axis is identical to the range direction, the  $y$ -axis

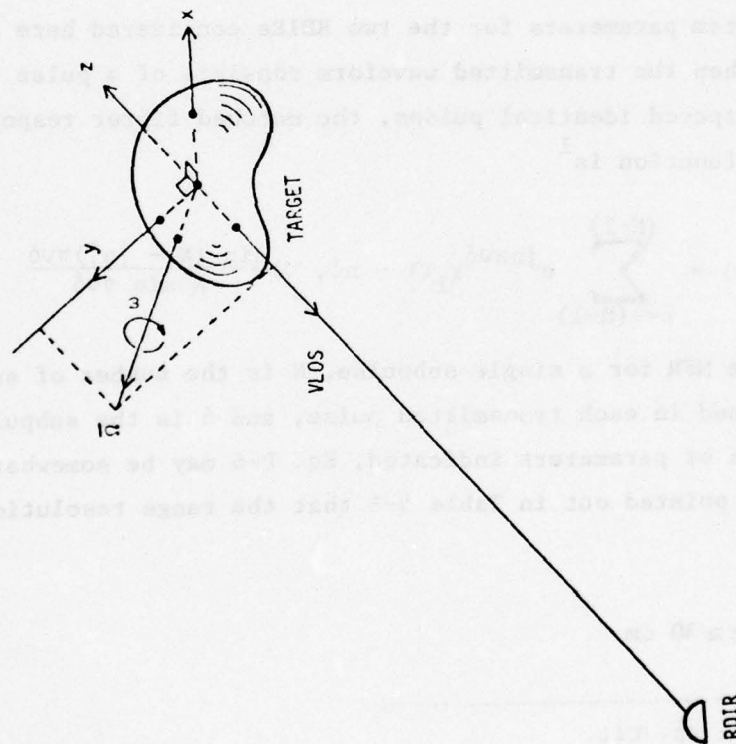


Figure D-1. Coordinate System Definition.  
 $\bar{\Omega}$  is the instantaneous spin axis.

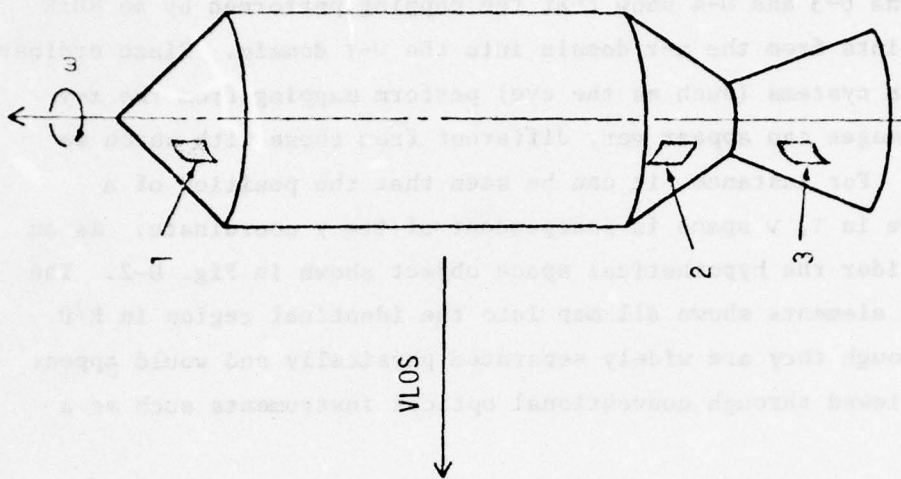


Figure D-2. Transformation-Induced Range-Doppler Ambiguities. All three indicated segments of the target map into the same range-Doppler cell.

is in the plane formed by the z-axis and the spin vector and is perpendicular to the VLOS. The x-axis, in the cross-range direction, is the third of the mutually perpendicular set.

Equations D-3 and D-4 show that the mapping performed by an RDIR transforms points from the x-z domain into the  $\nu$ - $\tau$  domain. Since ordinary imaging optics systems (such as the eye) perform mapping from the x-y domain, the images can appear very different from those with which we are familiar. For instance, it can be seen that the position of a target feature in  $\tau$ ,  $\nu$  space is independent of its y coordinate. As an example, consider the hypothetical space object shown in Fig. D-2. The three surface elements shown all map into the identical region in R/D space even though they are widely separated physically and would appear to be so if viewed through conventional optical instruments such as a telescope.

The system parameters for the two RDIRs considered here are given in Table 5-6. When the transmitted waveform consists of a pulse train composed of N equally spaced identical pulses, the matched filter response (MFR) or ambiguity function is<sup>1</sup>

$$\chi_N(\tau, \nu) = \sum_{n=-(N-1)}^{(N-1)} e^{jn\pi\nu\delta} \chi_1(\tau - n\delta, \nu) \frac{\sin(N - |n|)\pi\nu\delta}{N \sin \pi\nu\delta} \quad (D-6)$$

where  $\chi$  is the MFR for a single subpulse, N is the number of subpulses or chirps contained in each transmitted pulse, and  $\delta$  is the subpulse duration. For the choice of parameters indicated, Eq. D-6 may be somewhat simplified. First, it was pointed out in Table 5-6 that the range resolution for the waveform is

$$\Delta z \approx 30 \text{ cm} \quad (D-7)$$

---

<sup>1</sup>M. I. Skolnik, op. cit.

The ambiguities in the pulse train occur at increments in delay of

$$\Delta\tau = \delta \quad (D-8)$$

as evidenced in the argument of  $\chi_1$  in Eq. D-6. This corresponds to range ambiguities spaced apart by

$$\Delta z_{\text{amb}} = \frac{c\delta}{2} \rightarrow 1000 \text{ m} \quad (D-9)$$

Since it is very unlikely any targets of SOI interest will occupy a range increment approaching this distance, we may confine our attention to the central range lobe of the response for an MFR setting centered near the target.

In an analogous manner, the Doppler resolution is approximated by

$$\Delta\nu = \frac{1}{T_0} = \frac{1}{N\delta} \quad (D-10)$$

while the ambiguities in Doppler (at constant range) occur when

$$(N - |n|)\pi\nu\delta = K\pi \quad |K| = 0, 1, 2, \dots \quad (D-11)$$

Hence,

$$\Delta\nu_{\text{amb}} = \frac{1}{\delta}$$

Therefore, the number of resolution elements free of ambiguous response for a point target is given by

$$N_{\text{clear}} = \frac{\Delta\nu_{\text{amb}}}{\Delta\nu} = N \quad (D-12)$$

For large  $N$  ( $\sim 1000$  or greater) and in the SOI scenario, it is extremely unlikely that anticipated targets will be resolved to a degree approaching that indicated by Eq. D-12. Hence the central Doppler lobe can be considered the sole significant response for appropriately centered filter settings.

The net result is that to a very good approximation, Eq. D-6 can be replaced by

$$\chi_N(\tau, \nu) = \chi_1(\tau, \nu) \frac{\sin N\pi\nu\delta}{N \sin \pi\nu\delta} \quad (D-13)$$

The single pulse MFR can be shown<sup>1</sup> to be

$$\chi_1(\tau, \nu) = e^{j\pi\nu\tau} \frac{(\delta - |\tau|)}{\delta} \frac{\sin \pi(\alpha\tau + \nu)(\delta - |\tau|)}{\pi(\alpha\tau + \nu)(\delta - |\tau|)} \quad (D-14)$$

where  $\alpha = B/\delta$ . The factors of the argument of the sine function when expanded are

$$(\alpha\tau + \nu)(\delta - |\tau|) = \alpha\tau\delta - \alpha\tau|\tau| + \nu\delta - \nu|\tau| \quad (D-15)$$

In the vicinity of the central response lobe, i.e., where

$$\nu \ll 1/\delta \quad \text{and} \quad \tau \lesssim 1/B \quad (D-16)$$

all the terms in Eq. D-15 except the first are very much less than unity; hence,

$$|\chi_1(\tau, \nu)| \approx \frac{\sin \pi\alpha\delta\tau}{\pi\alpha\delta\tau} \quad (D-17)$$

and the WAF for the pulse train is given by

$$|\chi_N(\tau, \nu)|^2 = \left( \frac{\sin \pi B\tau}{\pi B\tau} \right)^2 \left( \frac{\sin \pi\nu T_0}{\pi\nu T_0} \right)^2 \quad (D-18)$$

---

<sup>1</sup>Skolnik, op. cit.

The computer program (RADIMS) which produces the simulated range-Doppler images uses the same target decomposition algorithms described in Sec. 3. Once the target has been decomposed into subareas and the cross section of each subarea computed using the TARGSIM code, RADIMS converts this data onto an array of matched filters with delay and Doppler settings centered at  $\tau_i$  and  $\nu_j$  respectively where  $\tau_i = \tau_{i-1} + \Delta\tau$  and  $\nu_j = \nu_{j-1} + \Delta\nu$ . The filter spacings ( $\Delta\tau$  and  $\Delta\nu$ ) are related to the range and Doppler resolution ( $\Delta R$  and  $\Delta f$ ) in the following manner:

$$\Delta\tau = (2/c) \Delta R$$

$$\Delta\nu = \Delta f$$

The output of a single matched filter with delay and Doppler settings centered at  $\tau_i$  and  $\nu_j$  respectively would correspond to a cross-section value given by

$$\sigma_{ij} = \sum_{\text{all } k} \Delta\sigma_k |\chi(\tau_k - \tau_i, \nu_k - \nu_j)|^2 \quad (\text{D-19})$$

The array of  $\sigma_{ij}$  for all  $i$  and  $j$  corresponds to an R/D image of the target.

The location of a given subarea in  $\tau, \nu$  coordinates can be calculated from the stored subarea data and a knowledge of the line of sight and instantaneous spin vectors of the target.

In particular, the delay ( $\tau_k$ ) and Doppler ( $\nu_k$ ) associated with subarea  $k$  relative to the target coordinate system origin can be found using

$$\tau_k = (2/c) \hat{\nu} \cdot \vec{R}_k \quad (\text{D-20})$$

$$v_k = \frac{2\omega_0}{\lambda} \frac{\vec{R}_k \cdot (\hat{\Omega} \cdot \hat{v})}{\left[1 - (\hat{\Omega} \cdot \hat{v})^2\right]^{1/2}} \quad (D-21)$$

where  $\vec{R}_k$  is the location vector for subarea k in the target coordinate system,  $\omega_0$  is the true, instantaneous target rotation rate, and  $\hat{\Omega}$ ,  $\hat{v}$  are unit vectors in the direction of the spin axis and sensor site respectively.

The sequence of operations performed by the program to produce an RDIR image is as follows:

1. The incremental cross section of each individual subarea is calculated using Eq. 3-2 with externally supplied BDR data. This value is stored in packed format in one of the subarea data arrays.
2. A pass is made over all subareas to determine the maximum and minimum coordinates of the subareas in both delay and Doppler. (This information is used to center the target in the image array.)
3. A second pass is made over the subarea data to distribute the stored value of cross section over the appropriately centered two-dimensional array of filters in  $\tau$ ,  $v$  space.

For each subarea  $\tau_k$  and  $v_k$  are calculated, and the value of the waveform ambiguity function (WAF), for all filters close enough to  $\tau_k$ ,  $v_k$  to respond significantly, is calculated. The filter responses are each incremented by an amount equal to the product of the subarea cross section and the particular value of the WAF.

## APPENDIX E

### BI-WAVELENGTH RANGE-DOPPLER IMAGING SYSTEM ANALYSIS

#### E.1 INTRODUCTION

The objective of this analysis is to investigate the feasibility of performing range-Doppler imaging using different lasers in the measurement of range and Doppler (e.g., CW gas laser for Doppler, pulsed solid-state laser for range). The analysis was made to determine the existence and extent of any fundamental problem areas which would prohibit, or seriously limit the use of this technique.

Analysis was made of the theoretical aspects of the problem which were then applied to a pulsed YAG laser and a CW CO<sub>2</sub> laser system. The analysis is developed in the following pages and includes results from a computer simulation of such a system.

After examining the analysis of the theoretical aspects of the problem and considering the capabilities of available laser technology, it was determined that the performance of the two laser (bi-wavelength) system was basically inferior to that of a single, large time-bandwidth laser system. The fundamental problem encountered with the bi-wavelength system concept is that the ambiguity functions of the individual laser sources add (rather than multiply). This means that the flaws of both sources are retained with little enhancement where they overlap. Specifically, a typical YAG laser meets all of the requirements for resolution in the range dimension. However, the effect of the phase uncertainties in typical YAG lasers indicates that the capability of the coherently processed YAG laser system to measure the target profile in the Doppler dimension is lost. The insertion of the CW laser is intended to retain this resolution. However, since the ambiguity functions of the individual sources add, any benefit obtained from an increase in the Doppler resolution provided by the CW laser is counterbalanced by a loss in range resolution caused by the addition of the side lobes of the CW laser's response to the overall ambiguity function.

The conclusion reached from this analysis is that the bi-wavelength technique using two different lasers is not competitive with other single-laser range-Doppler systems under development; and therefore, hardware development does not appear warranted.

## E.2 STATEMENT OF THE PROBLEM

Laser radars have been developed that utilized continuous (CW) and pulsed laser sources. The systems detecting Doppler information utilize the CW laser while the range information is obtained using pulsed laser sources. Utilizing specially designed large time-bandwidth product waveforms, it is possible to simultaneously obtain both the range and Doppler information at the output of the detector.<sup>1</sup> This output may be used to generate a two-dimensional "image" of the target, the two dimensions of the synthetic image being Doppler (as induced by the rotation of the target) and range (i.e., the time delay of the wavefront emanating from a given scattering center of the target).

The traditional method for generating the wide time-bandwidth signals is to frequency modulate the output of a CW laser source with a wide bandwidth signal and perform a matched filter detection of the received signal. This technology has been developed for microwave radars over the past three decades.<sup>2</sup> The performance of the first generation laser synthetic imaging systems is comparable to the performance of the microwave systems since similar devices (along with their similar limitations) are used in both systems.

The short wavelength of the laser outputs and the complex interaction of the lasing medium and the laser cavity give rise to an additional unique set of output waveforms. A typical, and useful, example of one of these waveforms is the output of a mode-locked laser which consists of an infinitely long set of pulses of short duration. Since this set of pulses has

---

<sup>1</sup>J. Wilson, op. cit.

<sup>2</sup>M. I. Skolnik, op. cit.

a phase coherence that can exist between a large number of these pulses, this waveform satisfies all of the requirements for the creation of R-R images. Laboratory systems have been developed which utilize the mode-locked YAG laser along with a modified matched filter to generate simple R-R images.<sup>1</sup>

Unfortunately, the performance of the mode-locked systems is degraded by the existence of random phase fluctuations within the pulse train that limit the resolution of the system in the frequency dimension. In this report, we consider the possibility of adding a second stabilized laser wavefront to the transmitted mode-locked pulse train to provide the required phase reference during the detection process. This constraint implicitly limits our analysis to the coherent class of receiver, of which the matched filter is the most useful.<sup>2</sup> Techniques that generate the R-R image utilizing incoherent (phase insensitive) post-detection techniques are also an option, but are eliminated from consideration in this report.

### E.3 SYSTEM CONCEPT

Matched Filter Implementation. The block diagram of the system concept is shown in Fig. E-1a. The matched filter required for the phase sensitive detection of the received beam is uniquely defined in the mathematical sense.<sup>3</sup> However, the implementation of these mathematical operations by physical devices can be performed in a number of ways. The classification of these devices have two major categories; the active devices such as a correlator, and the passive devices which are fabricated from passive components such as in the design of a filter that has an impulse response matched to the frequency spectrum of the transmitted

---

<sup>1</sup>W. Glenn, Personal Communications.

<sup>2</sup>M Schwartz, Information Transmission, Modulation, and Noise, McGraw-Hill (1959).

<sup>3</sup>P. M. Woodward, Probability and Information Theory, with Application to Radar, Pergamon Press (1953).

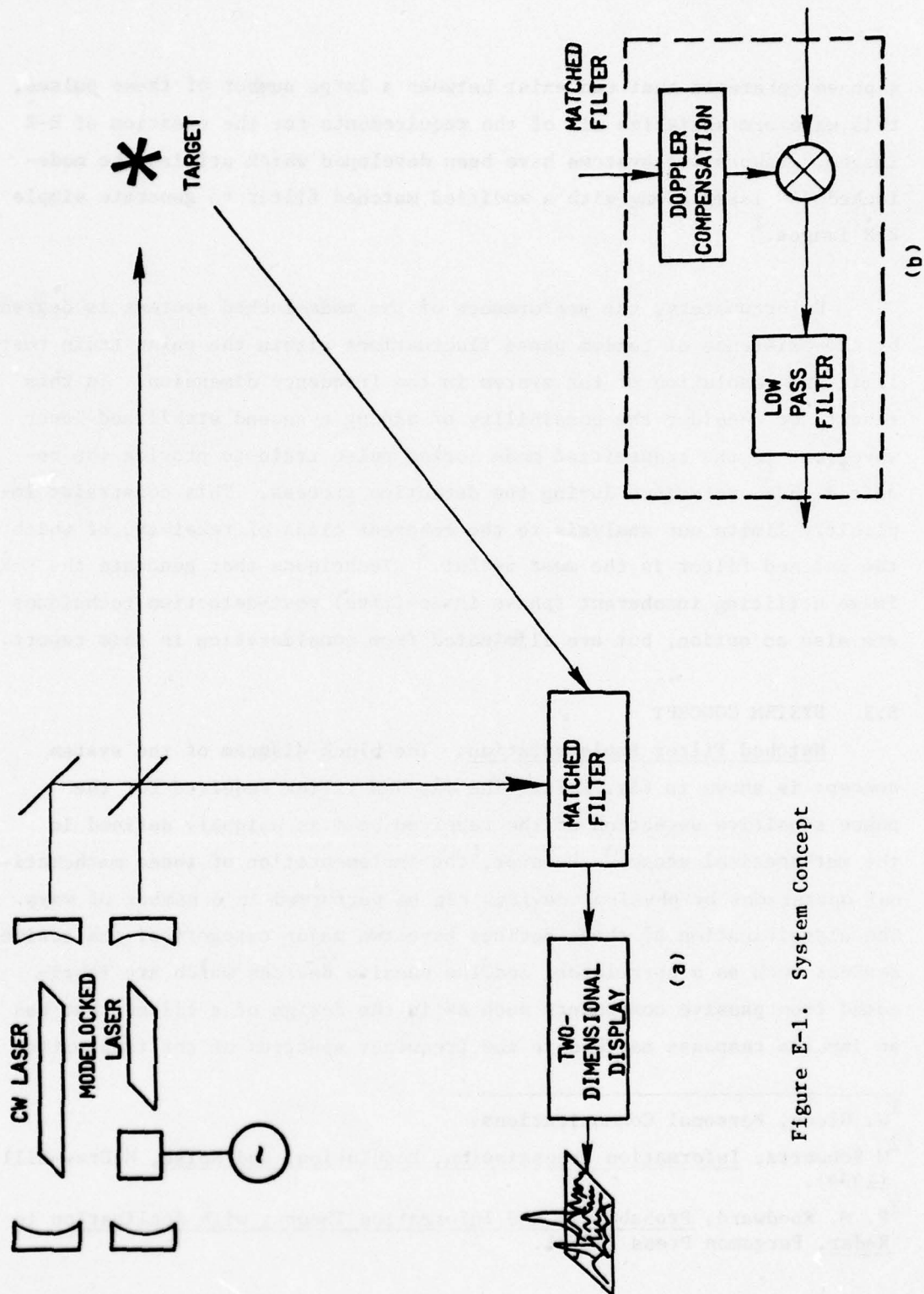


Figure E-1. System Concept

waveform. While all of these detectors give the same theoretically perfect reception of the detected signal, the uniqueness of the waveform associated with the output of the mode-locked laser places severe requirements on the design of the passive type of matched filter. Thus, only the active matched filter will be considered in the subsequent discussion.

We can conceptually define an active matched filter that has the potential of coherently detecting the received signal (i.e., maintain phase references between all of the components of the received signal) under the condition that the CW and pulsed lasers are operating at widely different wavelengths. This allows consideration of a system concept utilizing a mode-locked YAG laser at  $1.06\text{ }\mu\text{m}$  and CW laser at  $10.6\text{ }\mu\text{m}$ , for example. The system concept is still valid (with minor modifications) for the case where the CW and mode-locked lasers are operating at the same wavelength.

The operations that are required by the correlator type of matched filter are indicated in Fig. E-1b. The two inputs to the device are: (1) the optical wavefronts emanating from the target being interrogated and (2) a reference waveform that is obtained from the laser sources. The multiplication operation is performed by the optical detector during its conversion of the received optical wavefront into an electrical signal, with all of the subsequent operations performed by wideband electronic devices. When the system utilizes different wavelengths for the CW and the pulsed lasers, it is conceptually possible to use the same physical detector for the different color wavefronts (with the beat frequency between the two wavefronts occurring at a frequency far above the response of the detector--typically on the order of  $10^{13}\text{ Hz}$ ). Alternatively, a dichroic beam splitter can be introduced, with the introduction of two physically separated detectors responding to the two waveforms. In this case, it is still conceptually possible to maintain the phase reference between the two components of the received wavefront as measured

at the output of the active matched filter, thus satisfying all of the phase coherent requirements of the phase sensitive detector.

#### E.4 PERFORMANCE EVALUATION

An effective method for the comparison of the performance of competitive R-R systems is to utilize the concept of the ambiguity function. The ambiguity function is the blur function that is convolved with the pristine distributed cross section of the target to obtain the system output. Thus, in the case of a "perfect" R-R system, the ambiguity function would be a delta function. Any widening of the ambiguity function will give rise to a system degradation in the range and/or rotational Doppler dimension. The ambiguity function is also useful for the determination of detrimental effect of range and/or Doppler ambiguities resulting from the repeating nature of the mode-locked laser output.

The ambiguity function can be defined as an integral over time or frequency space, as indicated by the following equations:<sup>1</sup>

$$\chi(\tau, \nu) = \int_{-\infty}^{\infty} \mu(t) \mu^*(t - \tau) e^{j2\pi\nu t} dt \quad (E-1)$$

$$= \int_{-\infty}^{\infty} M^*(f) M(f - \nu) e^{j2\pi f \tau} df \quad (E-2)$$

where  $\mu(t)$  and  $M(f)$  are the temporal and frequency domain definition of the transmitted waveform.

Note that for the special cases where the values of  $\nu$  and  $\tau$  are set to zero, the ambiguity function as defined in Eq. E-1 gives the autocorrelation and the Fourier transform of the spectrum of the waveform, respectively. These degenerate relationships give us the form of the

---

<sup>1</sup>A. W. Rihaczek, op. cit.

ambiguity function along the frequency and time delay axes. Another feature indicated by the form of these equations is the duality of the variables  $\nu$  and  $\tau$ .

Characterization of the Laser Sources. The ambiguity function for the bi-wavelength system is easily defined in the frequency domain. A laser operating in a single transverse mode ( $TEM_{00}$ ) can simultaneously oscillate in a number of longitudinal modes if the spectral width of the active lasing medium is sufficiently wide. The introduction of the mode-locking device has the effect of "locking" all of these modes to a single phase reference. It is the coherent addition of all of these modes in phase at a given instant of time that gives rise to the high power short duration pulses from the laser. The form of the output signal is

$$E_M = \sum_{n=-N/2}^{N/2} a_n \exp \{ j2\pi[(f + n\Delta f)t + \tilde{\phi}_n] \} \quad (E-3)$$

where  $a_n$  = field magnitude of  $n$ th longitudinal mode

$\Delta f$  = difference frequency between longitudinal modes

$$= c/2L$$

$c$  = speed of light

$L$  = length of laser cavity

$f$  = frequency of central longitudinal mode

$$= c/\lambda_M$$

$\lambda_C, \lambda_M$  = wavelength of CW, mode-locked lasers, respectively

$\tilde{\phi}_n$  = phase uncertainty of  $n$ th mode

The addition of the CW laser source to the output of the transmitter simply adds an additional term to the form of the output. The transmitted waveform is

$$E_T = E_M + b \exp [j2\pi(f_c t + \theta)] \quad (E-4)$$

where  $\theta$  is the phase of the CW tone measured with respect to the mode-locked waveform at time  $t = 0$ . This waveform is assumed to have no phase error associated with it.

In practice, the phase error associated with one of the longitudinal modes will have some correlation with the phase errors of the other longitudinal modes. Also, the form of these random errors is strongly related to the temporal delay between the reference and the signal inputs to the active matched filter (see Fig. E-1). Thus, for the case when there is zero time delay between the two waveforms, one has complete correlation and the characterization of the random variable is unimportant. However, when we consider the parameter definition for SOI applications, the time delays can exceed a millisecond which will cause the phase error  $\tilde{\phi}$  to be the most important parameter in the determination of system performance.

In the following analysis, we assume that the variable  $\tilde{\phi}$  represents the uncorrelated phase errors of the system. One must approach with caution the numerical definition of the phase uncertainty errors associated with the laboratory measurements (where the time delay is nanosec or less) as compared to field operation of mode-locked lasers (where delays of msec can be encountered).

#### E.5 ANALYSIS

The analysis of this section answers the following topical questions:

- How do the phase instabilities that result in the operation of the mode-locked laser affect the imaging capability of the R-R system?
- What is the effect of the introduction of a CW tone upon the transmitted waveform, and how does it modify the imaging capability of the R-R system?

- What are the frequency response requirements of the optical detector of the receiver?
- Is the phase coherence of the received signal maintained during the detection process if the difference frequency between the CW and mode-locked lasers exceed the frequency response of the optical detector?
- How does the resolution of the system change as increasing amounts of the CW carrier are introduced into the transmitter waveform?
- What is the importance and the requirements for the compensation of the longitudinal Doppler during the processing of the received signal?

Deriving the form of the correlator output as a function of the input signals permits the evaluation of the importance of the carrier frequency (laser wavelength) on the output signal. Two cases will be considered: (1) where the difference frequency between the two lasers exceeds the frequency band pass of the correlator, as in the case of a mode-locked YAG laser operating with a CW CO<sub>2</sub> laser; (2) the case where the two lasers have a common carrier frequency as in the case of a mode-locked and CW laser both operating at 10.6  $\mu$ m. It will be demonstrated that as long as a phase coherent local laser oscillator is available at the receiver, the phase sensitive requirements as required by the coherent detection are satisfied.

The form of the transmitted signal waveform is

$$E = E_T \cdot [U(T_2) - U(T_1)] \quad (E-5)$$

where  $T_1$ ,  $T_2$  represent the duration of the waveform.  $U(T)$  is the unit step impulse.

Ignoring the propagation losses and propagation phase terms, the waveform that will be detected at the receiver after it has been scattered from a target that is characterized by a set of scattering centers, is

$$E' = \sum_{i=0}^I \sqrt{\sigma_i(u, v)} \sum_{n=-N/2}^{N/2} \left( a_n \exp \left\{ j2\pi \left[ (f_M + n\Delta f)t + \frac{\tilde{\phi}_n}{2\pi} + 2 \left( \frac{u_i \Omega t + z_i}{2M} \right) \right] \right\} \right. \\ \left. + \frac{b}{N+1} \exp \left\{ j2\pi \left[ f_C t + 2 \left( \frac{u_i \Omega t + z_i}{\lambda_C} \right) + \frac{\theta}{2\pi} \right] \right\} \right) \left[ U \left( T_2 - \frac{z_i}{c} \right) - U \left( T_1 - \frac{z_i}{c} \right) \right] \quad (E-6)$$

where  $\sigma_i$  is the cross section of the  $i$ th scattering center located at the position  $u_i, v_i, z_i$ .

The correlator multiplies the received and local reference signals and the subsequent low pass filtering of the signal suppresses all of the frequencies that are higher than the electronics bandpass frequency. Multiplying Eq. E-5 and E-6, dropping all frequency terms on the order or larger than  $f_M + n\Delta f - f_C$ , and assuming  $|f_M \pm n\Delta f - f_C| \gg 0$ , one obtains the results of E-7.

$$E_0 = E'E^* \Big|_{\text{filter}}^{\text{low pass}} = \sum_{i=0}^I \sum_n \sum_m \left( \sqrt{\sigma_i} a_n a_m^* \cos \left\{ 2\pi \left[ (n-m)\Delta f + \frac{2u_i \Omega}{\lambda_M} t + \tilde{\phi}_n - \tilde{\phi}_m + \frac{4\pi z_i}{\lambda_M} \right] \right\} + \sqrt{\sigma_i} |b|^2 \cos \left[ 2\pi \left( \frac{2u_i \Omega t + z_i}{\lambda_C} \right) \right] \right) \left[ U \left( T_2 - \frac{z_i}{c} \right) - U \left( T_1 - \frac{z_i}{c} \right) \right] \quad (E-7)$$

For the case when  $f_M = f_C$ , the  $a_0$  mode is assumed the CW reference and  $\tilde{\phi}_0 = 0$ .

$$E_0 = \sum_{i=0} \sum_n \sum_m \sqrt{\sigma_i} a_n a_m^* \cos \left\{ 2\pi \left[ (n - m)\Delta f + \frac{2u_i \Omega}{\lambda_M} \right] t + \tilde{\phi}_n - \tilde{\phi}_m \right. \\ \left. + \frac{4\pi z_i}{\lambda_M} \right\} \left[ U\left(T_2 - \frac{z_i}{c}\right) - U\left(T_1 - \frac{z_i}{c}\right) \right] \quad (E-8)$$

where  $a_0 \gg a_n$ , all  $n \neq 0$   
 $\tilde{\phi}_0 \equiv 0$

The parameters  $u_i$  and  $z_i$  are mapped by the matched filter detection into the  $\dot{R}$  and  $R$  axes of the range-Doppler image, respectively. Note that the phase uncertainties introduced by the random variables  $\tilde{\phi}_n$  and  $\tilde{\phi}_m$  will degrade our estimation of the parameter  $u_i$  obtained from the first term, but do not influence the accuracy of the measurement of the parameter  $z_i$  as defined in the step impulse or the estimate of  $u_i$  as obtained in the second term of Eq. E-7. Our later discussions will present techniques where the degradation introduced by the random phases can be at least partially eliminated through the judicious choice of the parameters  $a_n$  and  $b$  in the design of the transmitted and locally generated waveforms.

The heterodyne detection process maintains the phase of both the mode-locked and CW waveforms at the baseband frequencies (to within an unknown, but constant, phase term). Thus, the fabrication of a waveform by the addition of the outputs of two lasers is of itself not a fundamental limitation to the operation of a  $R$ - $\dot{R}$  imaging system.

Examination of Eq. E-7 does indicate the source of some possible distortion of the received image if the difference wavelengths of the two lasers differ significantly (say, by a quarter octave or more). Note that the Doppler dimension of the image as determined from the parameters  $u_i$  are a function of the laser carrier wavelength,  $\lambda_C$  or  $\lambda_M$ . Thus, if the wavelengths

of the two lasers differ significantly, the scale of the frequency dimension of the composite signal will not be constant for the various spectral components. This is not a fundamental limitation to the system concept, since techniques that use a change in scale that are related to the "stretch" techniques used in microwave systems or related scale modification techniques may have application. Finally, if the uncertainty introduced by the random phase errors  $\widehat{\phi}_n$  and  $\widehat{\phi}_m$  are very large, the first term of Eq. E-7 will be considered only as a noise term in the frequency dimension with the result that the frequency resolution of the bi-wavelength system will be determined uniquely by the CW laser wavefront.

A second order Doppler distortion limits some large time bandwidth product systems.<sup>1</sup> The magnitude of this effect is presently unknown and future analysis is needed to determine the sensitivity of the system to this effect.

#### E.6 AMBIGUITY FUNCTION

The frequency domain definition of the ambiguity function (Eq. E-2) will be used in the following analysis. To simplify the notation, we define the signal only in a functional sense. The parameters  $M_C$  and  $M_M$  denote the spectrum of a continuous cosine wave and mode-locked laser waveform over the time duration,  $T_2 - T_1$ , respectively. For the case when significant phase errors are included as in the mode-locked laser, the parameter  $M_M$  also includes the spreading of the spectrum by the random phase  $\widehat{\phi}_n$ . The frequency characterization of the composite transmitted signal is defined by the following equation.

$$M(f) = \sum_{n=-N/2}^{N/2} \left[ a_n M_M(f_M + n\Delta f) + \frac{b}{N+1} M_C(f_C) \right] \quad (E-9)$$

where  $M_M$  is the frequency profile of a given longitudinal cavity mode. The

---

<sup>1</sup>Rihaczek, op. cit., p. 61.

coefficients  $a_n$  are determined by the amplitude of the  $n$ th longitudinal mode, with the value of  $a_0$  assumed to be at the maximum of the gain curve.<sup>1</sup>

Substituting Eq. E-9 into Eq. E-2, the ambiguity function for the bi-wavelength system is

$$X(\tau, \nu) = \frac{1}{N} \sum_{n=-N/2}^{N/2} \sum_{m=-N/2}^{N/2} \int_{-\infty}^{\infty} \left[ M_M^*(f_M + n\Delta f) + \frac{b}{N+1} M_C^*(f_C) \right] \cdot \left[ M_M(f_M + m\Delta f - \nu) + \frac{b}{N+1} M_C(f_C - \nu) \right] e^{j2\pi f\tau} df \quad (E-10)$$

where  $N$ , the normalization constant, is  $b + \sum_{n=-N/2}^{N/2} a_n$

Using the arguments associated with Eq. E-7 under the condition that the CW laser frequency is much different than the frequency of all modes of the mode-locked laser, we may write the ambiguity function in the following form

$$X(\tau, \nu) = \frac{1}{N} \left[ \sum_{n=-N/2}^{N/2} \sum_{m=-N/2}^{N/2} a_n^* a_m \int_{-\infty}^{\infty} M_M^*(f + n\Delta f) M_M(f + m\Delta f - \nu) e^{j2\pi f\tau} df + |b|^2 \int_{-\infty}^{\infty} M_C^*(f) M_C(f - \nu) e^{j2\pi f\tau} df \right] \quad (E-11)$$

With the introduction of a new variable of integration in place of  $f + n\Delta f$ , we obtain

<sup>1</sup>P. W. Smith, Mode-Locking of Lasers, Proc. IEEE, Vol. 58, pp. 1342-1357, September 1970.

$$\chi(\tau, \nu) = \frac{1}{N} \left\{ \sum_n \sum_m a_n^* a_m e^{j2\pi n \Delta f \tau} \int_{-\infty}^{\infty} M_M^*(f) M_M[f + (m - n)\Delta f - \nu] e^{j2\pi f \tau} df \right. \\ \left. + |b|^2 \int_{-\infty}^{\infty} M_C^*(f) M_C(f - \nu) e^{j2\pi f \tau} df \right\} \quad (E-12)$$

$$= \frac{1}{N} \left\{ \sum_n \sum_m a_n^* a_m e^{j2\pi n \Delta f \tau} \chi_M[\tau, (m - n)\Delta f + \nu] + |b|^2 \chi_C(\tau, \nu) \right\} \quad (E-13)$$

where the ambiguity functions  $\chi_M$  and  $\chi_C$  represent the ambiguity function associated with the mode-locked and CW laser outputs, respectively. In some cases there are advantages in being able to add the ambiguity functions as indicated by the above equation. If one of the ambiguity functions has characteristics that are lacking in the output of the other laser, it is conceptually possible to add the laser waveforms in the proper ratio to generate a systems performance that has the required properties. It will be shown, however, that for the bi-wavelength system, consideration of the constraints placed upon the design of the component ambiguity functions by the receiver and laser source hardware leads to a resultant ambiguity function with inferior range-Doppler resolving characteristics. Also, in practical systems there is an unknown phase term between the two ambiguity functions which forces us to add the two components on a root-sum-squares basis.

It is instructive to examine the characteristics of the double summation that represents the ambiguity function of the mode-locked laser operating by itself. Introducing the indexing parameter,  $p$ ,

$$\sum_{n=-N/2}^{N/2} \sum_{m=-N/2}^{N/2} = \sum_{p=-N}^0 \sum_{n=-N/2}^{N/2-|p|} \left| \begin{array}{c} m = n - p \end{array} \right| + \sum_{p=1}^N \sum_{m=-N/2}^{N/2-|p|} \left| \begin{array}{c} n = m + p \end{array} \right| \quad (\text{E-14})$$

The above expansion corresponds to the same collection of terms as used in forming the autocorrelation function of an  $N + 1$  element sequence. With the above equation, the ambiguity function takes the following form,

$$\begin{aligned} \chi(\tau, \nu) = \frac{1}{N} & \left[ \sum_{p=-N}^0 \chi_M(\tau, \nu - p\Delta f) \sum_{n=-N/2}^{N/2-|p|} a_n^* a_{n-p} e^{j2\pi m \Delta f \tau} \right. \\ & + \sum_{p=1}^N e^{j2\pi p \Delta f \tau} \chi_M(\tau, \nu - p\Delta f) \sum_{m=-N/2}^{N/2-|p|} a_{m+p}^* a_m e^{j2\pi m \Delta f \tau} \\ & \left. + |b|^2 \chi_C \right] \quad (\text{E-15}) \end{aligned}$$

The summations over  $n$  and  $m$  indicate that the number of individual ambiguity functions superimposed at  $f = p\Delta f$  decreases with increasing  $|p|$ , that is, with distance from the  $u = 0$  reference plane. At the origin,  $\Delta f = 0$ ,  $p = 0$ , and a total of  $N + 1$  functions superpose. The number decreases linearly to a single function at  $f = N\Delta f$  for  $p = N$ . Thus the gross structure of the combined ambiguity function follows the same law as the autocorrelation function of a train of  $N + 1$  signals.<sup>1</sup>

The values of the parameter  $a_n$  are determined by the gain curve of the active laser medium. To a good approximation, the gain curve can be

<sup>1</sup>Rihaczek, op. cit.

written in the following form,

$$a_n = e^{-\alpha n} \quad (\text{E-16})$$

where  $\alpha$  is related to the spectral width of the gain curve of the active laser medium. For the case where we wish to assume that the gain is uniform over all of the longitudinal modes, substitute the value of  $\alpha = 0$ . Using the identity

$$\sum_{n=-A}^B x^n = x^{1/2(B-A-1)} \frac{x^{\frac{A+B}{2}} - x^{-\frac{A+B}{2}}}{x^{1/2} - x^{-1/2}} \quad (\text{E-17})$$

and the substitution

$$x = e^{j2\pi\Delta f\tau + \alpha} \quad (\text{E-18})$$

The following more familiar form results:

$$\sum_{n=-N/2}^{N-|p|} a_n^* a_{n-p} e^{j2\pi n\Delta f\tau} = e^{j\pi|p|\Delta f\tau + \frac{\alpha}{2}} \frac{\sin [(N - |p|)(4\pi\Delta f\tau + 2j\alpha)]}{\sin (2\pi\Delta f\tau + j\alpha)} \quad (\text{E-19})$$

Substituting into Eq. E-15, one obtains the reduced form of the ambiguity function of the bi-wavelength system.

$$\chi(\tau, \nu) = \frac{1}{N} \sum_{p=-N}^N (1 + e^{j2\pi p\Delta f\tau}) \chi_M(\tau, \nu - p\Delta f) \frac{\sin (N - |p|)[4\pi\Delta f\tau + 2j\alpha(2n - p)]}{\sin [2\pi\Delta f\tau + j\alpha(2n - p)]} \quad (\text{E-20})$$

For the condition where the weighting of the longitudinal modes is uniform, the imaginary part of  $\sin$  argument,  $\alpha$ , is zero, and the function has a form that is similar to that of an ambiguity function that one obtains when analyzing repetitive chirp waveforms.

Ignoring the phase factors, the shape of a given individual peak of the ambiguity function for the mode-locked laser which is the  $p$ th removed from the central maximum of the "bed of nails" will have the following function form:

$$\chi_p \triangleq a_m^* a_n \chi_M(\tau, \nu - p\Delta f) \frac{\sin \{(N - |p|)[4\pi\Delta f\tau + 2j\alpha(2n - p)]\}}{\sin [2\pi\Delta f\tau + j\alpha(2n - p)]} \quad (E-21)$$

This equation states that the form of the ambiguity function consists of an amplitude factor, the profile of an individual peak of the ambiguity function which determines the resolution of the system in the temporal dimension, and a  $\sin(nx)/\sin x$  function that determines the resolution of the system in the frequency dimension. The central peak ( $p = 0$ ) of the ambiguity function is used in practice during the operation of the system. From the form of the above equation, we see that the resolution of the bi-wavelength system in the  $z_1$  (temporal) dimension for the case  $\tilde{\phi}_n = 0$  is  $L/2N$ , whereas the resolution of the central peak in the  $u_1$  (frequency) dimension is  $2(T_2 - T_1)C$ .

#### E.7 PARAMETER DEFINITION

One is now in a position to qualitatively discuss the ambiguity function of a mode-locked laser. The ambiguity function is a "bed of nails" which has a period in the frequency dimension of  $\Delta f = C/2L$ . Substituting a value of  $L = 0.5$  m, the frequency separation between the impulses of the ambiguity function is 300 MHz. Thus, the ambiguities that could result in the frequency dimension will be of no concern except for the cases of rapidly rotating objects of large extent.

The separation between pulses as measured in the time domain are determined by the round trip propagation time within the cavity of the laser. These values are equal to the inverse of the repetition rate presented above, or 3.3 nsec for the half meter cavity length. In terms of length, these lasers would have an ambiguity in range at the distance of  $\pm L/2$ , i.e., the system could not differentiate between two scattering centers that are separated by the distance of  $L$  as measured along the optical axis. If one attempts to increase this ambiguity distance by increasing the length of the laser cavity, one runs the risk of introducing ambiguities in the frequency domain since the value of  $\Delta f$  becomes proportionately smaller during the scaling.

Thus, although the gross structure of the combined ambiguity function has frequency offset ambiguities spaced at the repetition period of  $\Delta f$ , there is also a structure with range ambiguities spaced at  $1/\Delta f$ , the time delay between successive pulses. The first effect results from periodicity in the frequency domain, whereas the second represents periodicity in the time domain. To a limited extent, one can perform a design trade-off between the ambiguities in the two domains by the definition of the laser cavity length, or in the case of more sophisticated systems, one could conceivably use pulse selection options.

#### E.8 EVALUATION OF $\chi_M$ , $\chi_C$ , AND $\chi^2$

The previous discussion did not require a definition of the profile of a single spike of the ambiguity function since we considered it only in the functional form. When we apply the theory of matched filter detection to laser systems, the extremely high carrier frequencies at which the lasers operate cause carrier frequency instabilities of only parts per million to significantly degrade the performance of the system. These instabilities, characterized by the random variable  $\tilde{\phi}$ , present only the uncertainty as detected during the time interval,  $T_2 - T_1$ . However, in

applications where the locally generated reference waveform for the correlation matched filter detector is an interval of the transmitted waveform delayed by a time interval of the propagation time which typically exceeds the pulse waveform duration, (typically on the order of msec), there may exist frequency shifts that remain constant over the duration of the signal waveform. Since these errors cause a shift of the R-R image in the frequency dimension but do not induce any distortion or blurring of the image, this type of long term frequency drift of the receiver local oscillator waveform will not be considered. Microphonics of the cavity will cause an additional FM type of modulation which has been previously analyzed by Cook.<sup>1</sup>

The resolution of the mode-locked waveform in the  $z_1$  direction was previously stated to be  $L/2N$ . For cavity lengths that are on the order of a fraction of a meter, the value of  $N$  for the YAG laser may have a value of several tens. Assuming a value of  $N = 25$  and a cavity length of  $L = 0.5$  m, the potential resolution of the YAG laser is 1 cm. The accuracy of this measurement is not degraded by phase uncertainties in the carrier frequency as characterized by the parameter,  $\tilde{\phi}$ . The limiting resolution of both the mode-locked and the CW lasers in the frequency dimensions are determined by the duration of the signal waveform  $T_2 - T_1$ . Assuming a value of 1 msec, a resolution of 1 kHz is obtainable in theory. Passively stabilized  $\text{CO}_2$  lasers have been demonstrated that obtain this level of stabilization. However, the performance of the YAG mode-locked laser is severely limited in its frequency resolution by the random phase errors as characterized by the parameter  $\tilde{\phi}$ . Many orders of magnitude improvement in the performance of these systems is not expected, although some procedures such as the utilization of a cavity of the ring laser type does show potential of at least reducing the phase instabilities caused by mode jumping. No known measurements of the phase uncertainty are available for the stability of stabilized mode-locked lasers measured over time delays on the order of a msec. However, it is undoubtedly orders of magnitude removed from the 1 kHz resolution hypothesized for the CW laser source.

<sup>1</sup>C. E. Cook, "Transmitter Phase Modulation Errors and Pulse Compression Waveform Distortion," Microwave Journal, May 1973, p. 63.

In comparing these values, we see that one of the systems (YAG) has a resolution in the range dimension that far exceeds most system requirements (and the bandwidth capabilities of the receivers), whereas the CW system has extremely poor range resolution capabilities but acceptable frequency resolution. It is possible to devise systems where we trade off these extreme capabilities to obtain more reasonable system specification.

The central peak of the ambiguity function of the bi-wavelength system as defined in Eq. E-21 will be used to determine the performance of the system. By choosing this as our criterion, we have implicitly assumed that the ambiguities in the range and frequency dimensions will not be significant. For conditions where the target is surrounded by a void and where one has (at least theoretically) the option of designing a mode-locked laser that has an optimized repetition rate as determined by the cavity length or the performance of a pulse selection device, this assumption is justified.

In many systems applications, one requires the definition of the ambiguity function in terms of power. From Eq. E-15 and E-21, the central peak of the power ambiguity function is

$$\chi^2 = \frac{1}{N} |\chi_p|^2 + |b|^2 |\chi_c|^2 \quad (\text{E-22})$$

In all cases of practical interest, the phase difference between the mode-locked and CW signals,  $\theta$ , will be unknown. Thus the phase  $\theta$  will be a random variable uniformly distributed 0 to  $2\pi$  and the summation of Eq. E-22 must be performed on an ensemble averaged basis,

$$\chi^2 = \frac{1}{N} \left( |\chi_p|^2 + |b|^2 |\chi_c|^2 \right) \quad (\text{E-23})$$

The shape of the individual functions as well as the composite ambiguity function are indicated graphically in Fig. E-2. A three-dimensional view of  $\chi$  is presented in Fig. E-3. Approximate values of the key parameters as discussed in the previous section are provided for reference. The scale factors that determine the relative magnitude of the two ambiguity functions are determined by the parameters  $a_n$  and  $b$ . Note that as the two ambiguity functions are superimposed, one obtains a narrow peak at the location  $\tau = \nu = 0.0$ . This peak will have a resolution that is potentially well beyond competitive systems;  $1 \text{ kHz} \times 100 \text{ psec}$  for the values that were assumed in Fig. E-2. However, this peak is superimposed upon a cross that has significant volume. This noisy base to the ambiguity function will introduce flares in the range and frequency dimensions at the location of all of the bright scattering centers. For any remaining diffuse area (encountered in most laser illuminated targets) the noisy base will introduce a nominally constant diffuse background of generally uniform intensity over the entire frame. The extent to which this flaring and the diffuse background will limit the utility of the bi-wavelength system is critically dependent on the value of  $\phi$  and the scaling parameters  $a_n$  and  $b$ .

#### E.9 COMPUTER SIMULATIONS

The utility of the bi-wavelength range-Doppler system was evaluated by a computer simulation. A hypothetical ambiguity function as demonstrated in Fig. E-4 was defined. This ambiguity function corresponds to the case where the mode-locked laser lacked the phase stability required for the measurement of the Doppler. Using the fast Fourier transform (FFT) digital computer techniques, this hypothetical ambiguity function was convolved with a number of selected point and extended targets. Figures E-5 and E-6 are the pristine representation of a multiple point target, and the Meteor satellite, respectively. The blurred images that are obtained from the bi-wavelength system are shown in Figs. E-7 and E-8, respectively. As one would expect, there is a severe flaring of the images which result from the "cross" of the ambiguity function.

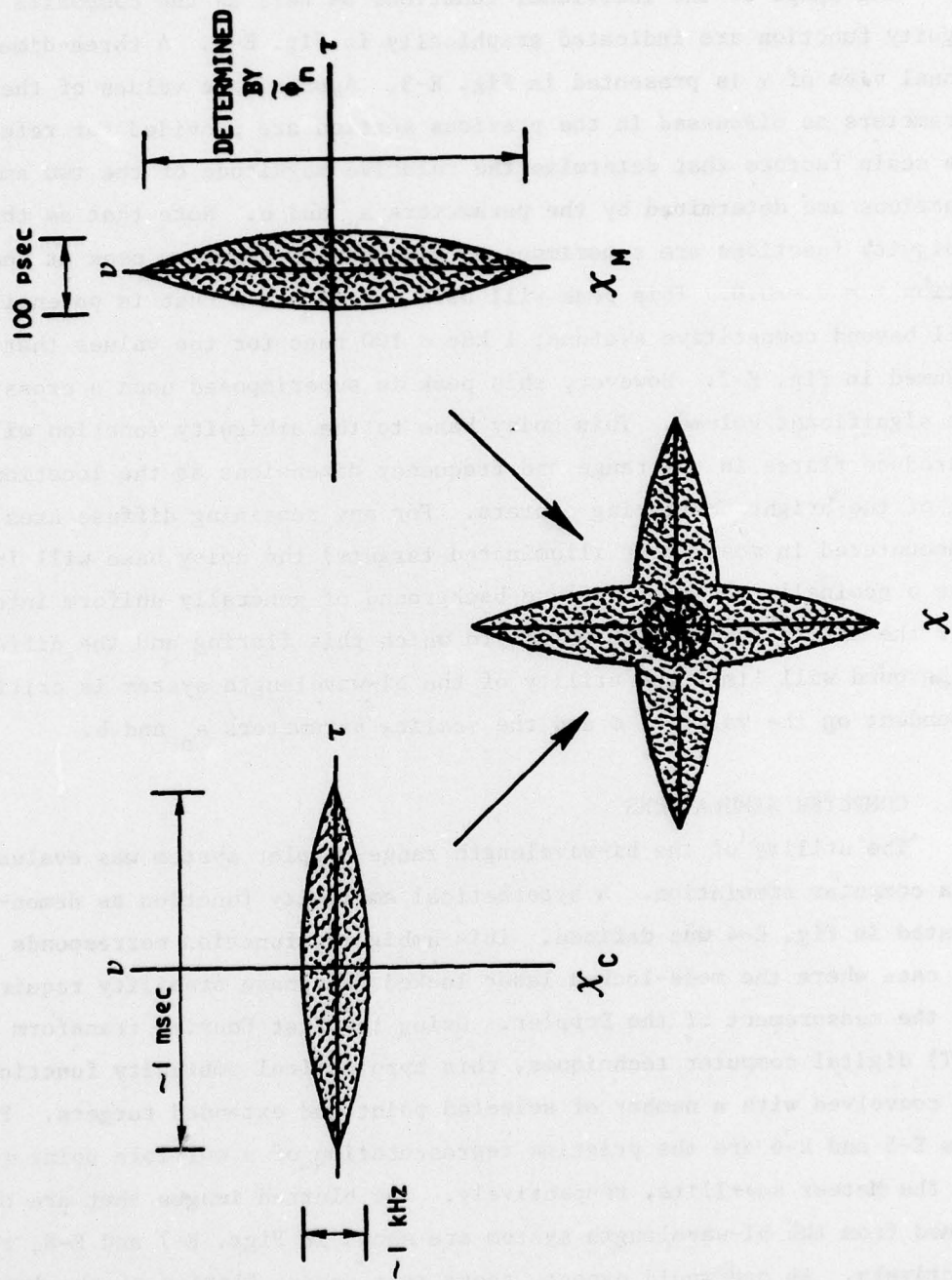


Figure E-2. Superposition of CW and Mode-Locked Laser Ambiguity Functions

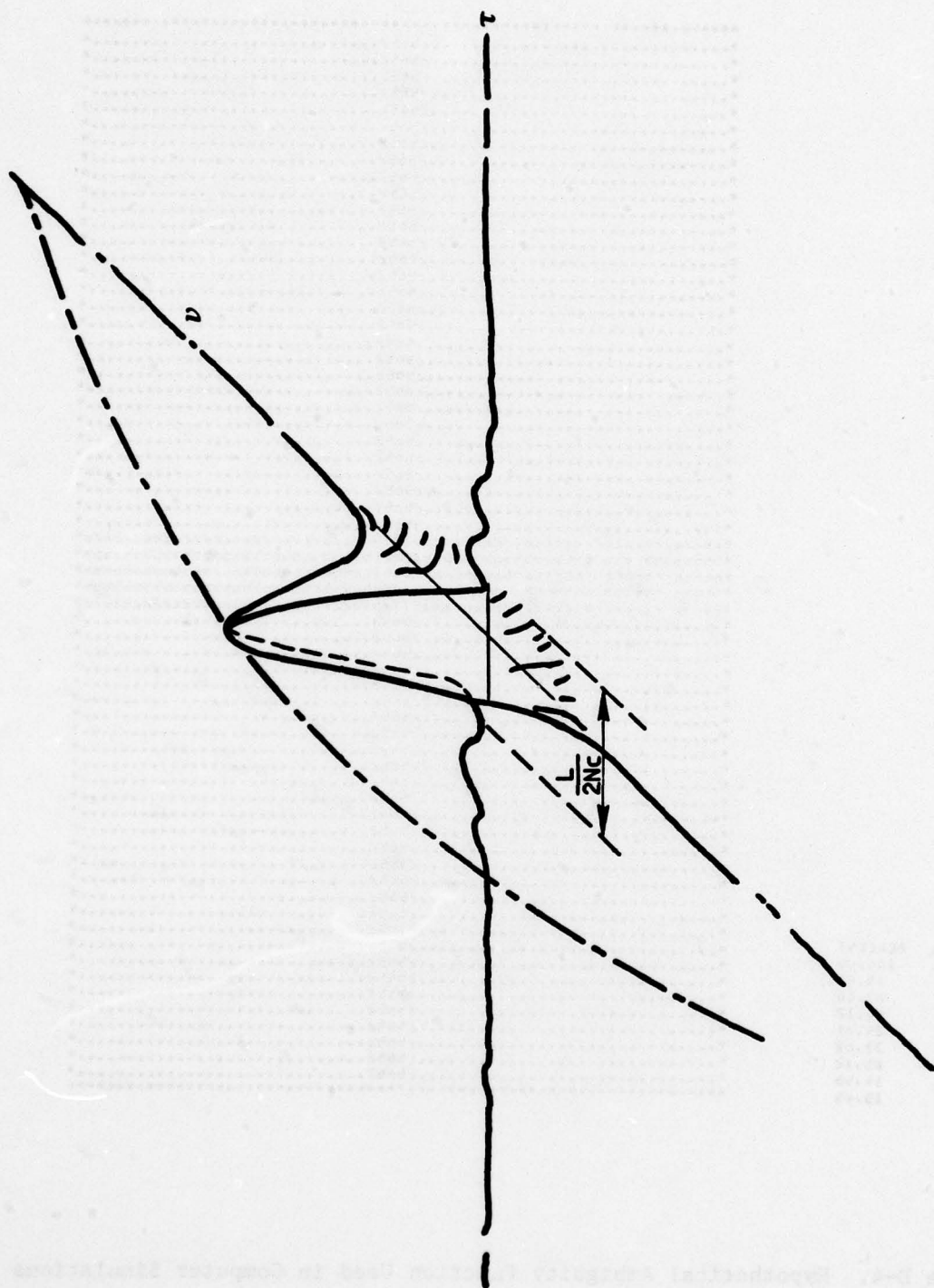


Figure E-3. Central Peak of Mode-Locked Laser Ambiguity Function

SYSTEM FIELD/INTENSITY PLOT

DB PER STEP = 1.00  
0 DB LEVEL = 1.000000

LEVEL	PERCENT
9	100.00
8	79.43
7	63.10
6	50.12
5	39.01
4	31.62
3	25.12
2	19.95
1	15.85

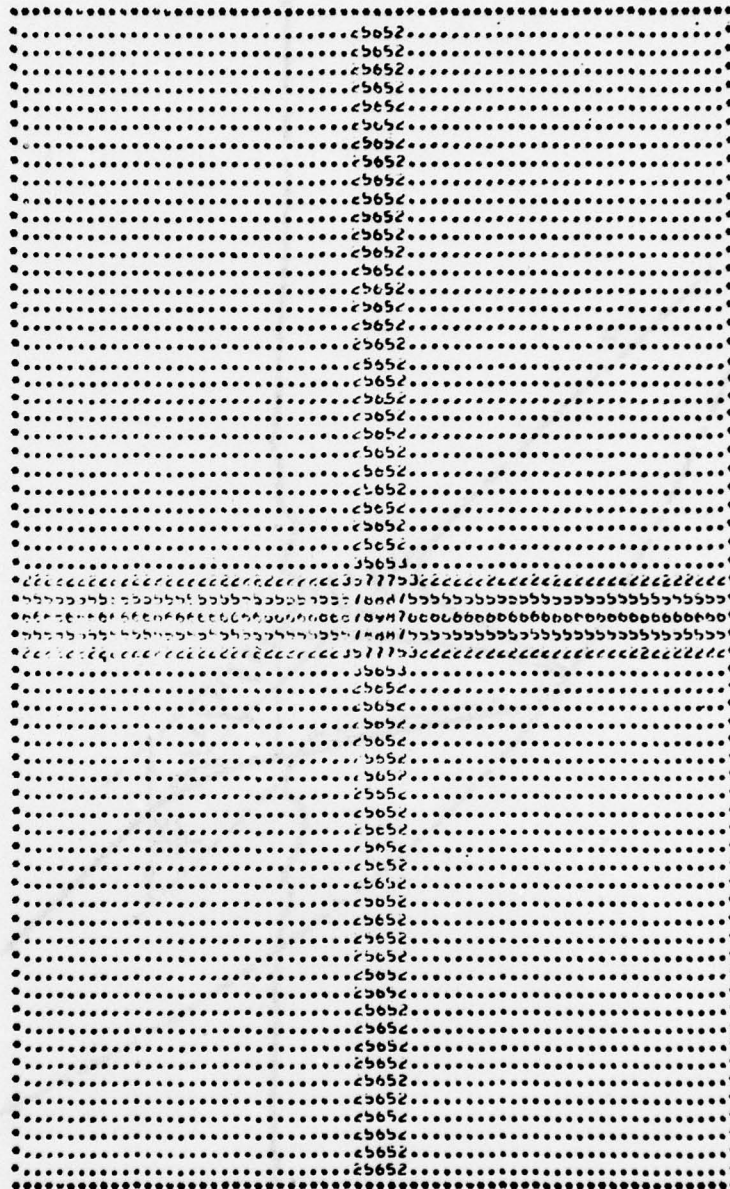


Figure E-4. Hypothetical Ambiguity Function Used in Computer Simulations

(only copy available)

SYSTEM FILE/INITIALS/FILE

DB PER STEP = 1.0  
 V DB LEVEL = 1.000E+00

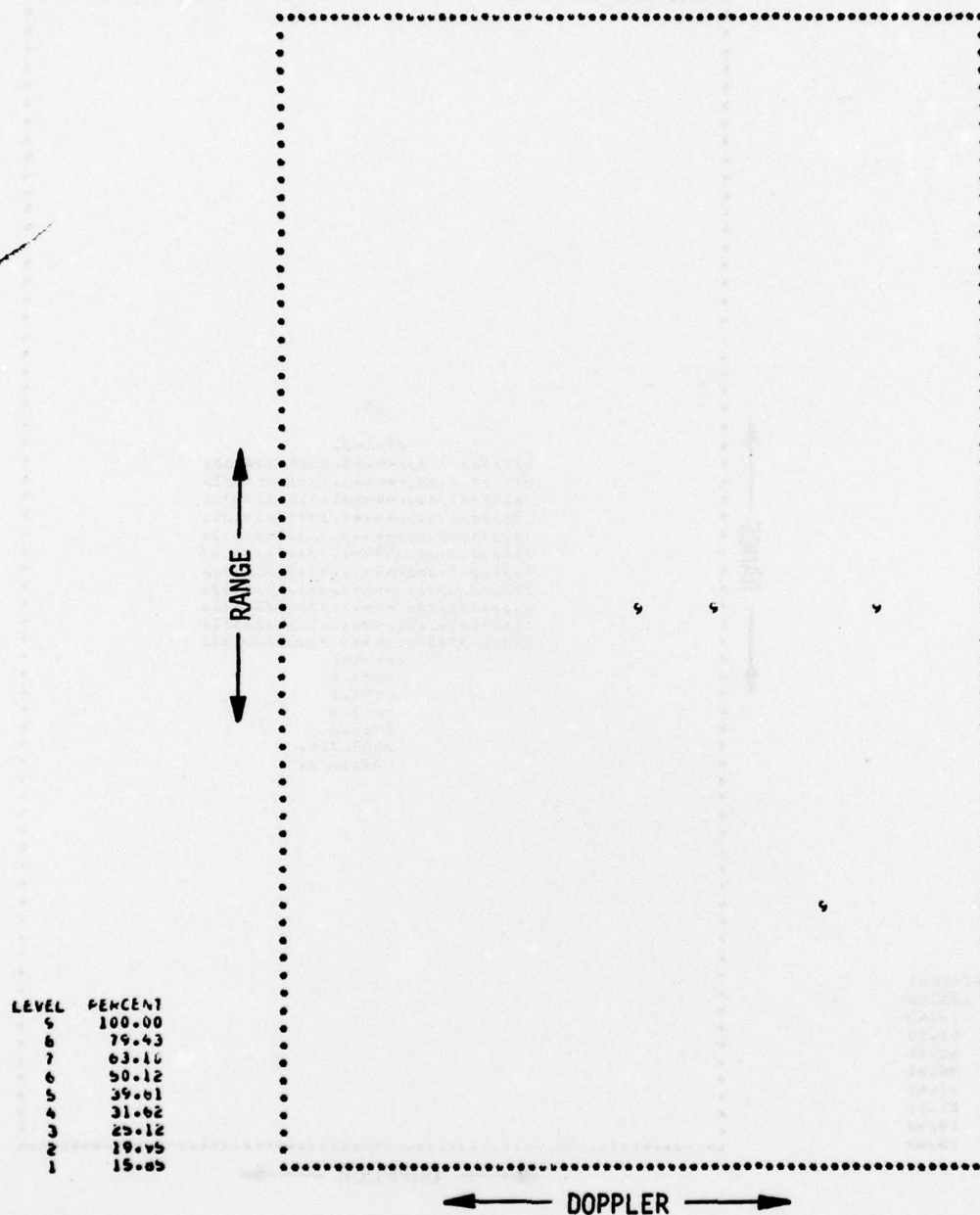


Figure E-5. Representation of a Four Point Target in Range-Doppler Space

(only copy available)

SYSTEM FIELD INTENSITY PLOT

DB PER STEP = 1.00  
0 DB LEVEL = 3.459E-01

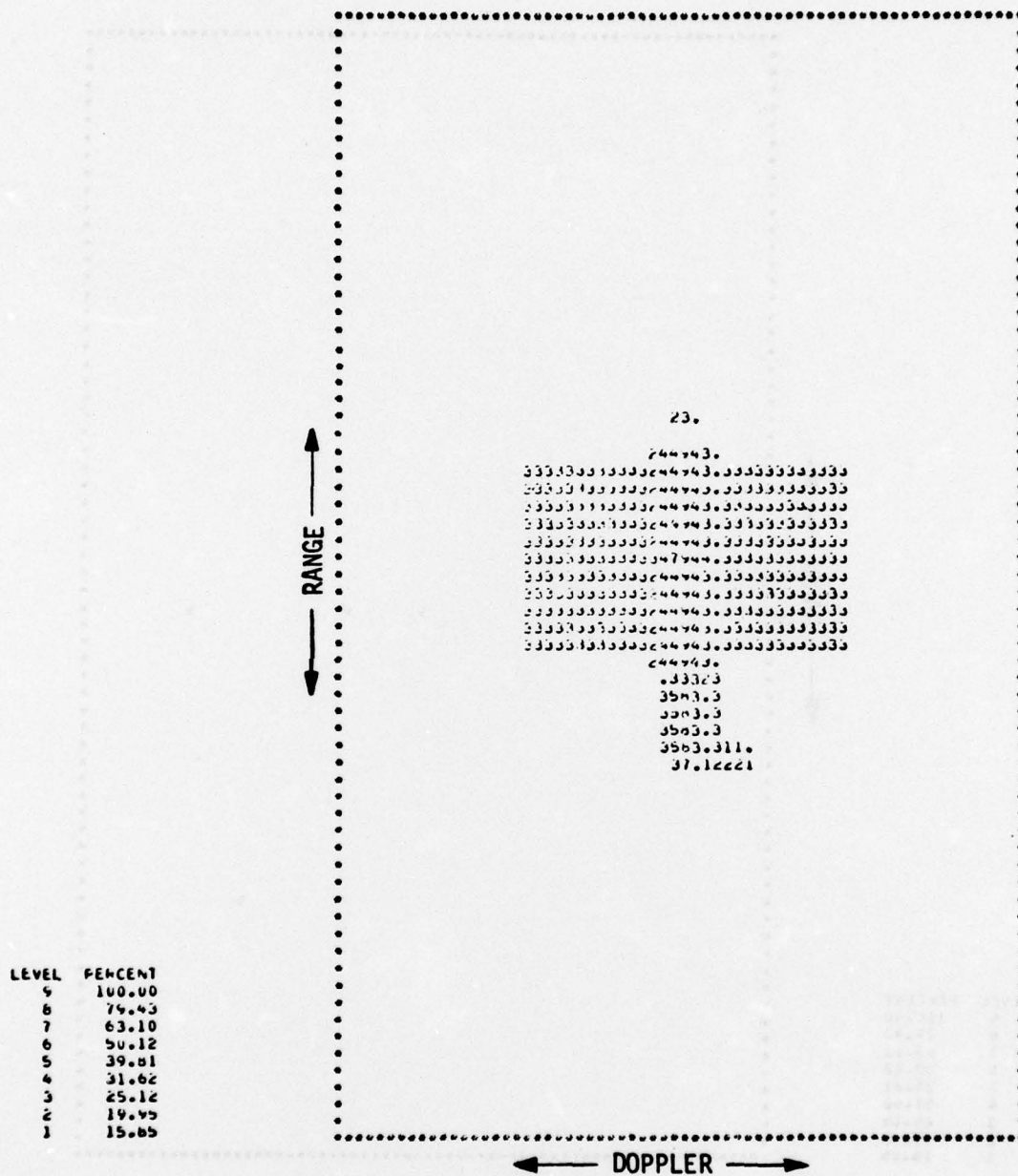


Figure E-6. Representation of the Meteor Satellite in Range-Doppler Space  
(only copy available)

SYSTEM FILE / INTERFERENCE FILE

D3 PEN STEP = 1.0  
0 DB LEVEL = 1.0/101-12

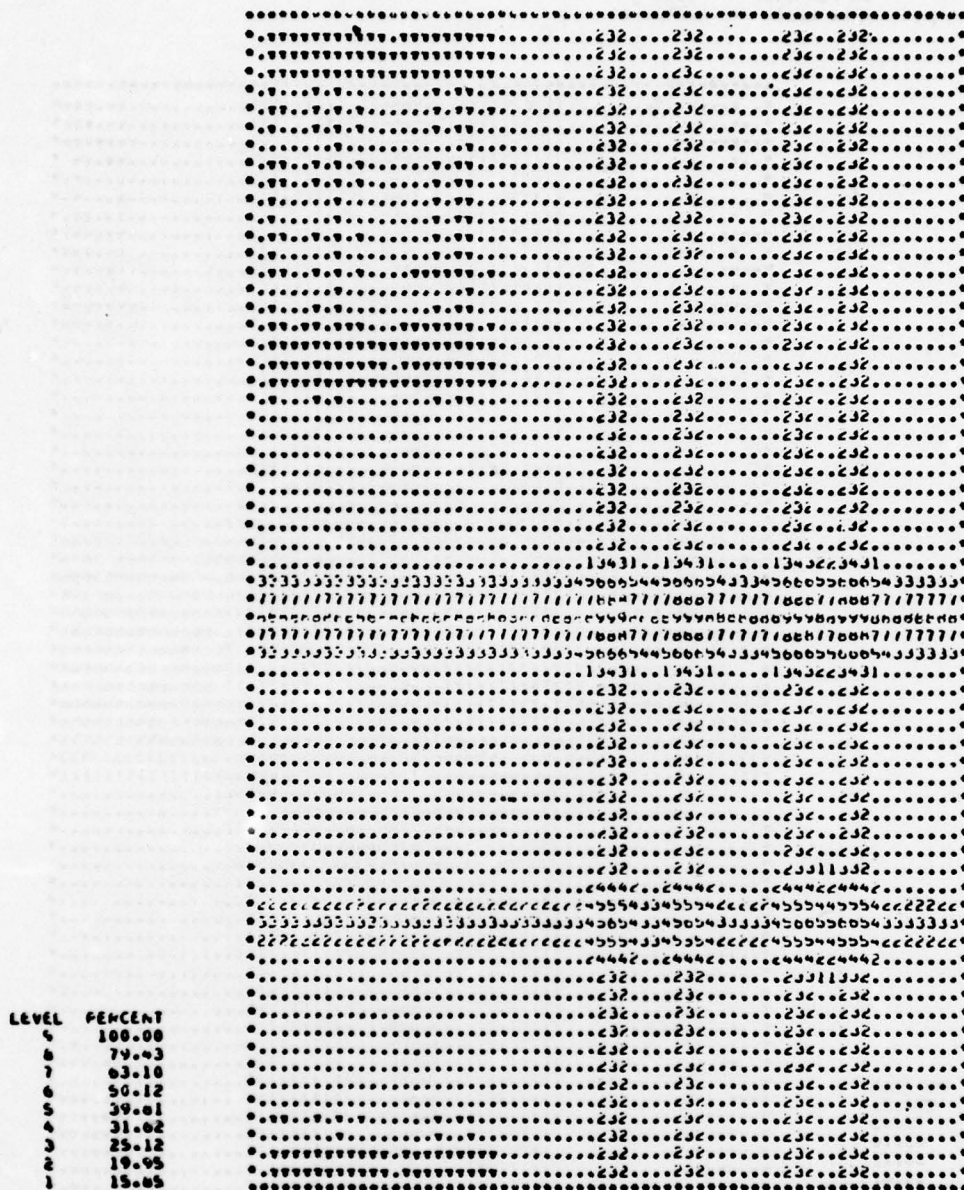


Figure E-7. Range-Doppler Image of Four Point Target

(only copy available)

SYSTEM FIELD/INTEGRITY TEST

On PER STEP = 1.00  
 0 DE LEVEL = 4.003E-02

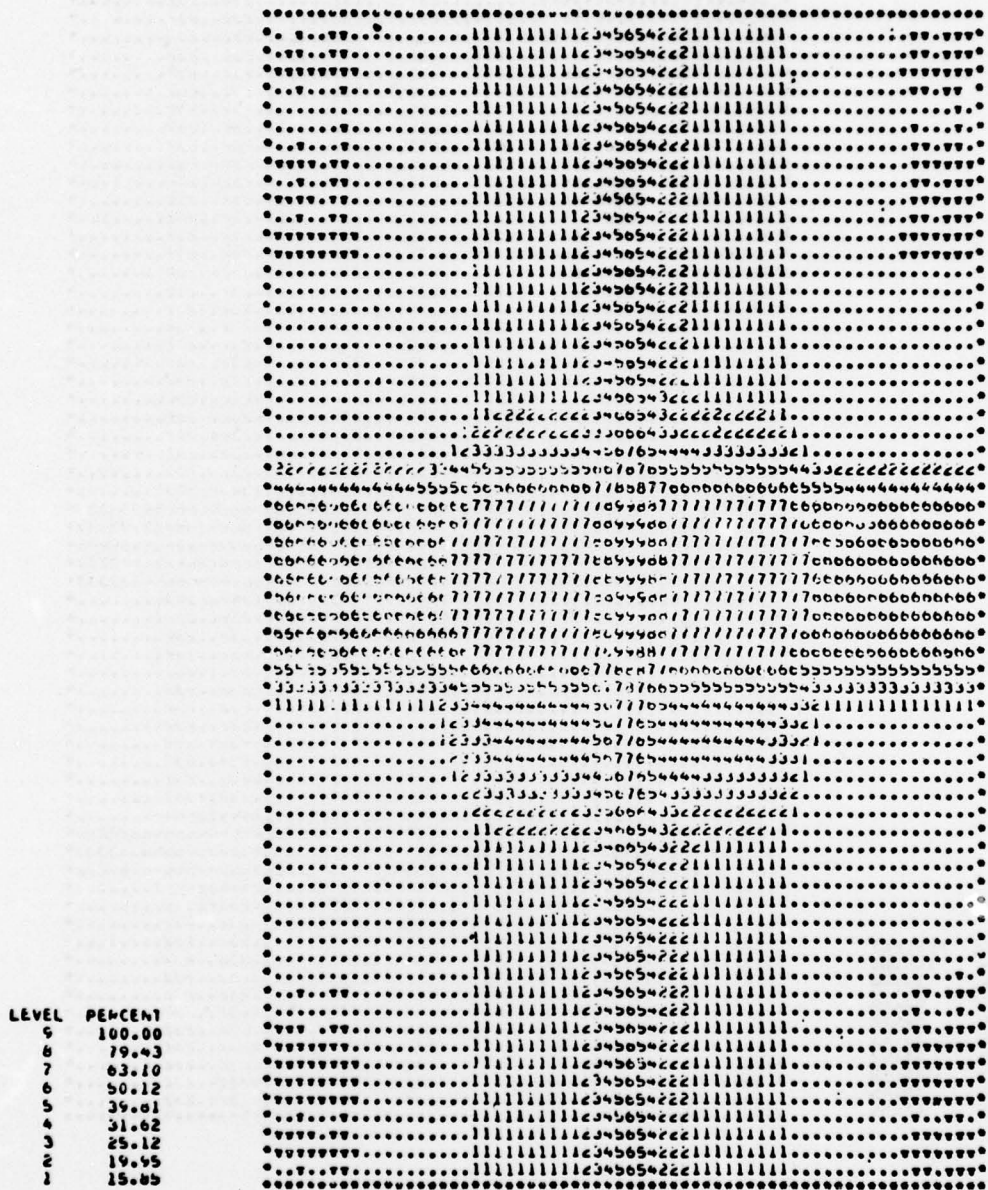


Figure E-8. Range-Doppler Image of Meteor Satellite

(only copy available)

Since the shape of the ambiguity function is a known function that can be obtained analytically or by a calibration of the receiver, it is theoretically possible to deconvolve the blur function from the distorted image and obtain the original undistorted image of the target using the Van Cittert technique. Such a procedure was attempted on the above images and the results indicated that the convergence of the algorithm was slow. When one includes the additional factors of uncertainty in the knowledge of the ambiguity function, speckle effects, and system noise, it is doubtful that post-detection processing of the blurred images can be used to advantage.

#### E.10 PERFORMANCE EVALUATION

The previous analysis and computer simulations will be used as the basis for the explicit evaluation of the topical questions that were stated in the introduction of Sec. E.5. These questions will be answered in the order presented in Sec. E.5.

The phase instabilities of the mode-locked laser as characterized by the random variable  $\tilde{\phi}$  have the effect of broadening the ambiguity function in the frequency dimension as indicated in Fig. E-2, with only a minimal influence on the resolution that is obtainable in the time dimension. This in turn creates the flares on the resultant  $R\text{-}\dot{R}$  image in the frequency dimension of the final image.

The introduction of the CW tone was analytically indicated in Eq. E-6 where we note that the additional CW tone will appear as another frequency line in the spectrum of the transmitted signal. Since this single sinusoid has only limited resolution in the time domain, its existence in the composite signal will introduce flares in the temporal dimension that are analogous to the previously discussed flares from the mode-locked laser in the frequency dimension. As expected, the CW tone gives rise to the flares in the temporal dimension as indicated in Figs. E-7 and E-8.

The utilization of the active matched filter hypothesized in Sec. E.3 permitted the physical separation of the coherent CW and mode-locked receiver. The "cost" of this design compromise is that the absolute phase reference between the two lasers is lost during the receiver processing. Even if care had been taken to insure the retention of the absolute phase information of the mode-locked and CW lasers during the receiver processing, it is most doubtful that the dispersions occurring in the propagation paths could have been compensated to a fraction of a radian (at the optical frequencies) as required by the system definition. Thus, the receiver detector bandwidths required for the optical detectors are only those required for the distortionless conversion of the received optical signal into the output electrical signal. This will be on the order of 100's of MHz to GHz for the mode-locked laser signal and a MHz or less for the CW receiver. In other words, the absolute phase coherence between the CW and the mode-locked laser signals is lost during the propagation to the target, and is not utilized in the signal processing of the receiver.

The effect on the system performance as increasing amounts of the CW carrier are introduced into the composite signal is most easily understood by referring to Fig. E-2. By controlling the ratio of the contributions of  $\chi_M$  and  $\chi_C$ , one controls the volume in the frequency and temporal flares of the composite function,  $\chi$ . Thus one has the capability of "fine tuning" the volume of the temporal and frequency flares in an attempt to generate a composite ambiguity function that has the desired properties. This process can only be performed to the extent allowed by the geometry of the individual ambiguity functions, however.

The implementation of a system with separate detectors for the CW and mode-locked lasers permits the definition of a system where the longitudinal Dopplers of the two lasers can be compensated separately (most likely, with frequency tracking servos operating on the local oscillators). This can be readily seen in Eq. E-7 by noting the wavelengths of the two

lasers ( $\lambda_C$  and  $\lambda_M$ ) are associated uniquely with the signal waveforms of the individual lasers, and that no cross product terms of the two carrier frequencies are obtained with the type of processing assumed in this report.

#### E.11 CONCLUSIONS

The utility of the bi-wavelength system is very dependent on the type of lasers that are used for the pulsed and CW sources. The parameters of center operational wavelength, the phase stability of the laser sources over the signal duration, the long term drifts of the center frequencies of the lasers over the propagation time delays, and the characteristics and rotation rates of the target are most important. If one is anticipating using the bi-wavelength technique to interrogate a slowly rotating target at long ranges by a system using a repetitively pulsed YAG laser and a CW  $\text{CO}_2$  laser system, the utility of the system is very limited. Introducing a commercial quality mode-locked YAG laser will not significantly increase the performance of the system due to the frequency instabilities of the presently available YAG lasers. Since these instabilities result from fundamental considerations such as mode jumping in the laser cavity active medium, significant theoretical and engineering effort would be required to develop YAG lasers that would meet the stability requirements of the bi-wavelength system. It is doubtful that post-detection picture processing will enhance the resultant image to a quality obtained by range-Doppler systems presently under development. Thus, the bi-wavelength technique using YAG and  $\text{CO}_2$  lasers is not competitive with other range-Doppler systems under development.

The analysis has indicated a number of alternate system definitions that may hold potential. It has been suggested that a mode-locked wave guide  $\text{CO}_2$  laser could be developed which has the frequency stability required for range-Doppler imaging. As demonstrated in the previous analysis, a system utilizing such a device can generate high resolution range-Doppler images of the interrogated targets without the requirement for an associated stable CW laser. The preceding analysis could be used as the basis for determining the stability requirements and system definition for a range-Doppler system operating at  $10.6 \mu\text{m}$ .

# METRIC SYSTEM

## BASE UNITS:

Quantity	Unit	SI Symbol	Formula
length	metre	m	...
mass	kilogram	kg	...
time	second	s	...
electric current	ampere	A	...
thermodynamic temperature	kelvin	K	...
amount of substance	mole	mol	...
luminous intensity	candela	cd	...

## SUPPLEMENTARY UNITS:

plane angle	radian	rad	...
solid angle	steradian	sr	...

## DERIVED UNITS:

Acceleration	metre per second squared	...	m/s
activity (of a radioactive source)	disintegration per second	...	(disintegration)/s
angular acceleration	radian per second squared	...	rad/s
angular velocity	radian per second	...	rad/s
area	square metre	...	m
density	kilogram per cubic metre	...	kg/m
electric capacitance	farad	F	A·s/V
electrical conductance	siemens	S	A/V
electric field strength	volt per metre	...	V/m
electric inductance	henry	H	V·s/A
electric potential difference	volt	V	W/A
electric resistance	ohm	...	V/A
electromotive force	volt	V	W/A
energy	joule	J	N·m
entropy	joule per kelvin	...	J/K
force	newton	N	kg·m/s
frequency	hertz	Hz	(cycle)/s
illuminance	lux	lx	lm/m
luminance	candela per square metre	...	cd/m
luminous flux	lumen	lm	cd·sr
magnetic field strength	ampere per metre	...	A/m
magnetic flux	weber	Wb	V·s
magnetic flux density	tesla	T	Wb/m
magnetomotive force	ampere	A	...
power	watt	W	J/s
pressure	pascal	Pa	N/m
quantity of electricity	coulomb	C	A·s
quantity of heat	joule	J	N·m
radiant intensity	watt per steradian	...	W/sr
specific heat	joule per kilogram-kelvin	...	J/kg·K
stress	pascal	Pa	N/m
thermal conductivity	watt per metre-kelvin	...	W/m·K
velocity	metre per second	...	m/s
viscosity, dynamic	pascal-second	...	Pa·s
viscosity, kinematic	square metre per second	...	m/s
voltage	volt	V	W/A
volume	cubic metre	...	m
wavenumber	reciprocal metre	...	(wave)/m
work	joule	J	N·m

## SI PREFIXES:

Multiplication Factors	Prefix	SI Symbol
1 000 000 000 000 = 10 <sup>12</sup>	tera	T
1 000 000 000 = 10 <sup>9</sup>	giga	G
1 000 000 = 10 <sup>6</sup>	mega	M
1 000 = 10 <sup>3</sup>	kilo	k
100 = 10 <sup>2</sup>	hecto*	h
10 = 10 <sup>1</sup>	deka*	da
0.1 = 10 <sup>-1</sup>	deci*	d
0.01 = 10 <sup>-2</sup>	centi*	c
0.001 = 10 <sup>-3</sup>	milli	m
0.000 001 = 10 <sup>-6</sup>	micro	μ
0.000 000 001 = 10 <sup>-9</sup>	nano	n
0.000 000 000 001 = 10 <sup>-12</sup>	pico	p
0.000 000 000 000 001 = 10 <sup>-15</sup>	femto	f
0.000 000 000 000 000 001 = 10 <sup>-18</sup>	atto	a

\* To be avoided where possible.

## **MISSION** **of** **Rome Air Development Center**

RADC plans and conducts research, exploratory and advanced development programs in command, control, and communications (C<sup>3</sup>) activities, and in the C<sup>3</sup> areas of information sciences and intelligence. The principal technical mission areas are communications, electromagnetic guidance and control, surveillance of ground and aerospace objects, intelligence data collection and handling, information system technology, ionospheric propagation, solid state sciences, microwave physics and electronic reliability, maintainability and compatibility.

